The Development of Intra-train Beam Stabilisation System Prototypes for a Future Linear Collider

Michael Davis
Balliol College, Oxford

Thesis submitted in fulfilment of the requirements for the degree of Doctor of Philosophy at the University of Oxford

Hilary Term, 2014

Abstract

Any future linear collider requires a beam stabilisation system at the interaction point to the to maintain luminosities. This thesis details the development of prototypes of three such systems based at the Accelerator Test Facility 2 (ATF2) at KEK, Japan.

The upstream feedback system utilises two stripline beam position monitors (BPMs) and two stripline kickers located in the ATF2 extraction line to stabilise the position and angle of the beam; the correction is then measured downstream at the ATF2 beam waist by a cavity BPM. The feedforward system uses the two upstream stripline BPMs to measure the position of the beam and calculate a correction signal which is then implemented locally by a stripline kicker located near the beam waist; the correction is then measured at the beam waist by a cavity BPM. The IP feedback system uses the position measured at the ATF2 beam waist by a cavity BPM and implements a correction based on this position using the local stripline kicker; the correction is then measured at the beam waist by a cavity BPM. Tests of the upstream feedback system have demonstrated stabilisation of the ATF2 beam waist at approximately the 300 nm level; tests of the feedforward and IP feedback systems have demonstrated stabilisation of the ATF2 beam waist at approximately the 100 nm level.

Additional work undertaken to improve the processing electronics of the stripline BPMs is detailed. The cavity BPMs and their electronics are characterised and offline analysis techniques to improve the BPM resolutions set out. Results demonstrating resolutions of approximately 350 nm for the stripline BPMs and 80 nm for the cavity BPMs are presented.

Acknowledgements

I am exceptionally grateful to the many people who helped contribute to this work. In particular I owe much to Prof. Phil Burrows who has pushed and guided me throughout my time at Oxford and who has been an excellent supervisor. My thanks goes out to the entire FONT group without whom this work would have been impossible and in particular Neven, Young-Im, Doug, Colin, Javier, Rob and Glenn. Likewise, the work of the FONT group would be impossible without the wider ATF collaboration, to all of whom I offer thanks.

I would like to thank my parents Gerry and Diana; girlfriend Tara; the boys from Vinnies and the Dome; and friends both in Oxford and out. Finally I would like to thank Andy for keeping me company during our regular coffee breaks.

Contents

List of Figures

List of Tables

Chapter 1

Introduction

Particle physics is the study of the fundamental properties of the universe. The field concerns research into the nature of energy and matter and the forces which govern their interactions. Research in the field aims to understand the basic laws of the universe in terms of a mathematical framework, referred to as the Standard Model. This theory postulates that the universe is made up of quarks, leptons, and force carrying particles - gauge bosons.

1.1 Particle Accelerators

Particle accelerators are the main tools used by particle physicists to probe the nature of the universe. First developed in the early 1930s modern particle accelerators are capable of accelerating particles to near the speed of light and considerable energies.

Over time particle physicists have craved accelerators with higher energies and luminosities. The desire for higher energies is driven by two factors: First the structures being probed are getting smaller; to observe such tiny structures the resolution of the probe must be below the size of the structure. The resolution of a probe is given by its wavelength λ. Visible light has a wavelength of order 10^{-7} m which is too large to observe even the atomic level (10^{-10} m). The wavelength of a particle probe (λ) is given by the De Broglie formula

$$\lambda = \frac{h}{p} \tag{1.1}$$

where h is the Planck constant and p is the particle's momentum and so as the momentum of a given particle increases its wavelength decreases. Secondly, over time the particles physicists are trying to study have increased in mass. To create such particles at rest requires energy E governed by

$$E = m_0 c^2 \tag{1.2}$$

where m_0 is the rest mass of the particle and c is the speed of light.

The current energy record for a particle accelerator is held by the Large Hadron Collider (LHC) at CERN. In 2012 the LHC successfully accelerated protons to an energy of 4 TeV [1].

Particle accelerators come in different forms. Currently there are two types of particle accelerators used in particle physics: 1) Linear accelerators or linacs for short which consist of a long straight line of accelerating cavities. Particles are injected into this line at one end and pass through it thereby gaining energy as they go. 2) Synchrotrons are circular accelerators which use bending magnets to steer a beam of particles around a closed loop. Once input the particles pass many times around the loop; fewer accelerating structures are needed in these accelerators as the energy of the particles can be increased minutely on every turn.

Both types of accelerator have advantages and disadvantages. Linacs are single pass machines and so there is only one chance to use the particles once they are accelerated. Although this is not the case for synchrotrons they have a different set of challenges: As a particle's energy increases so does its momentum and therefore the force required to bend it; the strength of the bending magnets in the accelerator must therefore scale with the beam energy. Additionally bending beams of high energy electrons causes the emission of radiation in a direction tangential to the beam's trajectory [2]. This energy - known as synchrotron radiation - must be replaced every turn. Machines which only accelerate the electron enough to replace these energy losses are known as storage rings.

1.2 Colliders

Particle physics normally involves colliding a beam of high energy particles into some form of target; the target can take the form of either a stationary object or another beam of high energy particles.

Colliding particles with a fixed target is considerably easier than colliding them with another incoming beam. This method also has the advantage that the centre of mass frame is moving with respect to the rest frame of the laboratory so a detector placed downstream of the interaction point (IP) is sufficient to detect any particles produced in the collision. This however leads to the main disadvantage of such a collider: as the particles produced have a large forward momentum less energy is available for the creation of new particles. As such this method is unsuitable for colliders at the energy frontier.

In high energy colliders two beams of equal energy are directed at one another and collided to form new particles. As the beams have opposing momenta the rest frame of the collision is stationary with respect to the laboratory. Here the energy available for the creation of

new particles is equal to the sum of the energies of the two beams. As the collisions happen in a centre of mass frame that is at rest with respect to the laboratory, particles produced have momentum which is directed outwards; a detector must therefore be constructed to surround the IP.

A linear collider is constructed by directing two linacs towards one another to form an IP. Circular colliders use two synchrotrons normally placed within the same tunnel which circulate beams in opposite directions; at one or more points around the rings the two beams cross to form an IP.

A second important quantity is the luminosity, L. The likelihood of a certain particle interaction X occurring is given by

$$P(X) = L\sigma(X) \tag{1.3}$$

where $\sigma(X)$ is the physics cross section for the interaction. L is given by [3]

$$L = H\frac{fN^2}{4\pi\sigma_x\sigma_y} \tag{1.4}$$

where f is the frequency at which the bunch pairs cross at the IP; N is the number of particles in each bunch; σ_x and σ_y are the horizontal and vertical beam sizes at the IP respectively and H is the enhancement factor which accounts for the electromagnetic forces present at the collision.

In a circular collider f is a function of the collider's frequency of revolution. Once the beams have been accelerated to their required energy they can be stored and used for collisions over many hours [4]. In a linear collider f is governed by the repetition rate of the linacs and so is lower. In addition any particles which do not collide are lost as the beam is dumped after the IP. To achieve a reasonable luminosity in a linear collider the other parameters in Equation 1.4 must be optimised. In particular smaller beam sizes are used at a linear collider; this shall be discussed later.

1.3 Recent Achievements in Particle Physics

The Standard Model is a theory that describes the universe in terms of elementary building blocks [5]. The theory postulates that the universe is made up of two types of particles: half integer spin fermions and whole integer spin bosons. In the Standard Model fermions are the basic building blocks of matter, bosons then act as the force carriers between the fermions. Table 1.1 lists the particles in the Standard Model.

Fermions themselves come in two groups: quarks and leptons. There are six types of quark (u, d, c, s, t, b) which exist only in bound states of two or more. The lepton family is further subdivided into three charged leptons (e, μ, τ) and their respective neutrinos (ν_e , ν_μ, ν_τ).

Fermions				Bosons
Quarks	u	c	t	$W^{\pm}/Z$
	d	s	b	γ
Leptons	e	μ	τ	g
	ν_e	ν_μ	ν_τ	H

Table 1.1: The fundamental particles of the Standard Model.

Each of these particles then has a corresponding antiparticle which has the same mass as its respective particle and opposite charge.

Of the bosons there is one or more type for each force. Gluons mediate the strong force; the W and Z bosons mediate the weak force and photons mediate the electromagnetic force.

A mechanism for the quantisation of the masses of the Standard Model particles ('the Brout–Englert–Higgs mechanism') was postulated by Peter Higgs and others [6] in 1964. The theory hypothesises that there exists a uniform field throughout space which particles interact with. The strength of a particle's coupling to this field is proportional to its mass. The physical manifestation of this Higgs field is a massive spinless boson: the 'Higgs boson' indicated by H in Table 1.1.

Experiments in particle physics have had notable success in validating the Standard Model. All the particles predicted by the Standard Model had been observed prior to 1995 with the exception of the top quark, tau neutrino and Higgs. Results from the Tevatron at the Fermi National Laboratory yielded the first experimental evidence of the top quark in 1995 [7] and the tau neutrino in 2001 [8]. The Higgs was observed in experiments at the LHC in 2012 [9], [10].

1.4 Next Generation Colliders

Protons are a bound state of three quarks held together by gluons. Equation 1.5 denotes the power emitted in the form of synchrotron radiation when a charged particle is accelerated

$$P \propto \frac{e^4}{m_0^2 r^2} \tag{1.5}$$

where e is the energy of the particle; m_0 is the rest mass of the particle and r is the radius of curvature of the bend the particle is passing through. The relatively high mass of the proton means that in proton beams the emission of synchrotron radiation is low and as such it is possible to accelerate a beam of protons to a very high energy. This energy, will however be shared between the constituent particles in a proton in an uneven manner. A collision between two protons at some centre of mass energy will therefore actually be a collision between these constituent particles at some lower unspecified centre of mass energy. This

Parameter	ILC	CLIC
Centre of Mass Energy (TeV)	0.5	3
Luminosity ($\times 10^{34}\text{cm}^{-2}\text{s}^{-1}$)	2	5.9
Repetition frequency (Hz)	5	50
Bunch population (electrons)	2×10^{10}	3.72×10^{9}
Bunches per train	2526	312
Bunch spacing (ns)	369	0.5
σ_x (nm)	640	45
σ_y (nm)	5.7	0.9

Table 1.2: Design parameters for ILC and CLIC.

introduces certain difficulties with a proton-proton collider: 1) Particles produced will have been created in a collision between two particles of unknown momenta, be they quark-quark, quark-gluon or gluon-gluon. 2) The energy of the colliding particles is unknown. 3) Reactions between the other particles in the proton can occur and will create large backgrounds. These difficulties conspire to make particle identification a formidable task in a proton-proton collider.

A lepton-lepton collider accelerates point-like particles for collisions typically producing particles by S-channel processes like the one shown in Figure 1.1 (a). In such a process the centre of mass energy is given by the sum of the energy of the two beams (ignoring beam-beam effects). This means both the constituent particles and the centre of mass energy in reactions are known making particles identification easier; in addition backgrounds are lower than at a proton collider [11]. Finally if the production of certain specific particles is desired the centre of mass energy can be set at a resonance for the production of this particle type, greatly increasing the likelihood such a particle will be produced [12].

Having established the case for a lepton-lepton collider the exact layout of such a machine should be carefully considered. Addressing firstly the type of lepton used for collisions the two massive leptons μ and τ have lifetimes that make them unsuitable for a collider as current technology is not advanced enough to accelerate them within this time [13]. Any lepton collider in the foreseeable future would therefore collide electrons and positrons.

The energy produced by synchrotron radiation by a particle of mass m_0 is proportional to $1/m_0^4$ [14]. As such an electron following the same trajectory as a proton and travelling with the same energy would radiate 1×10^{13} times the synchrotron radiation. Assuming it is prohibitively expensive to build a tunnel much larger than that of the LHC a second option is to construct a linear collider; in such a machine the beams of particles are not bent and so energy loss via synchrotron radiation is negligible.

Currently there are two main design proposals for such a collider: the International Linear Collider (ILC) and the Compact Linear Collider (CLIC). The two propsals are notably different in design and centre of mass energy and of the two the ILC is at a more advanced stage of development than CLIC. Some key parameters of both accelerators are given in Table 1.2.

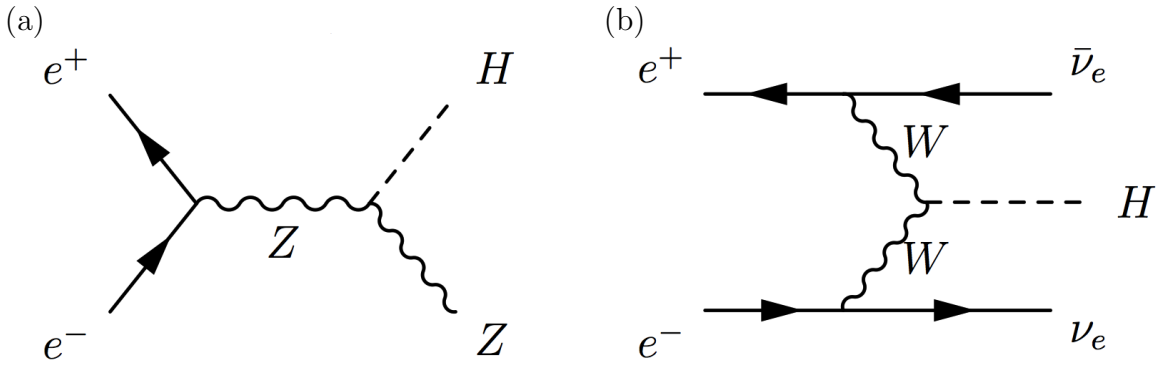

Figure 1.1: Feynman diagrams for Higgs production via (a) Higgs-strahlung and (b) W-W fusion.

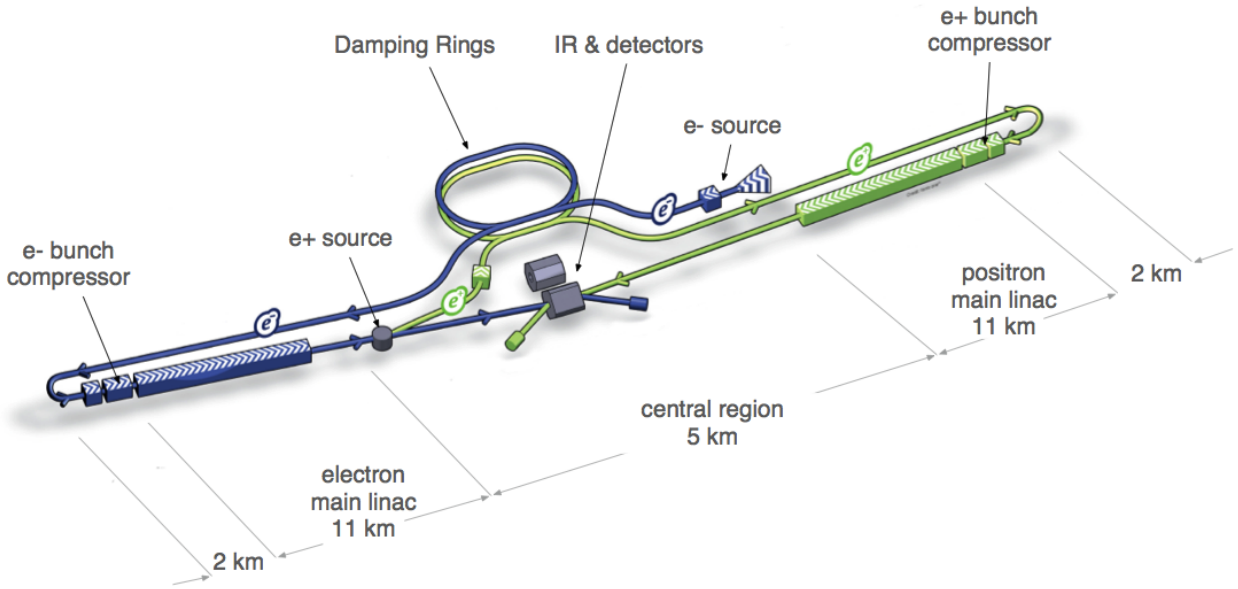

Figure 1.2: A schematic layout of the ILC, indicating all the major subsystems (not to scale).

1.4.1 The ILC

The ILC (Figure 1.2 [15]) consists of two superconducting linear accelerators orientated towards one another. One accelerator will accelerate electrons and the other positrons with an initial centre of mass energy of 500 GeV and the possibility of an upgrade to 1 TeV. Each accelerator shall be made up of about 16,000 niobium cavities providing an accelerating gradient of 31.5 MeV/m. The design parameters of the ILC are detailed in [16].

With an initial centre of mass energy of 500 GeV the ILC is designed primarily as a Higgs factory. Higgs bosons will be produced mainly via two mechanisms (Figure 1.1): (a) Higgs-strahlung ($ee \rightarrow ZH$) and (b) W-W fusion ($ee \rightarrow \nu_\mu\nu_\mu H$) [17]. At a collision energy of 250 GeV and assuming a Higgs production cross section of 200 fb a luminosity of 2×10^{34} $cm^{-2}s^{-1}$ would produced approximately 22,000 Higgs bosons per year.

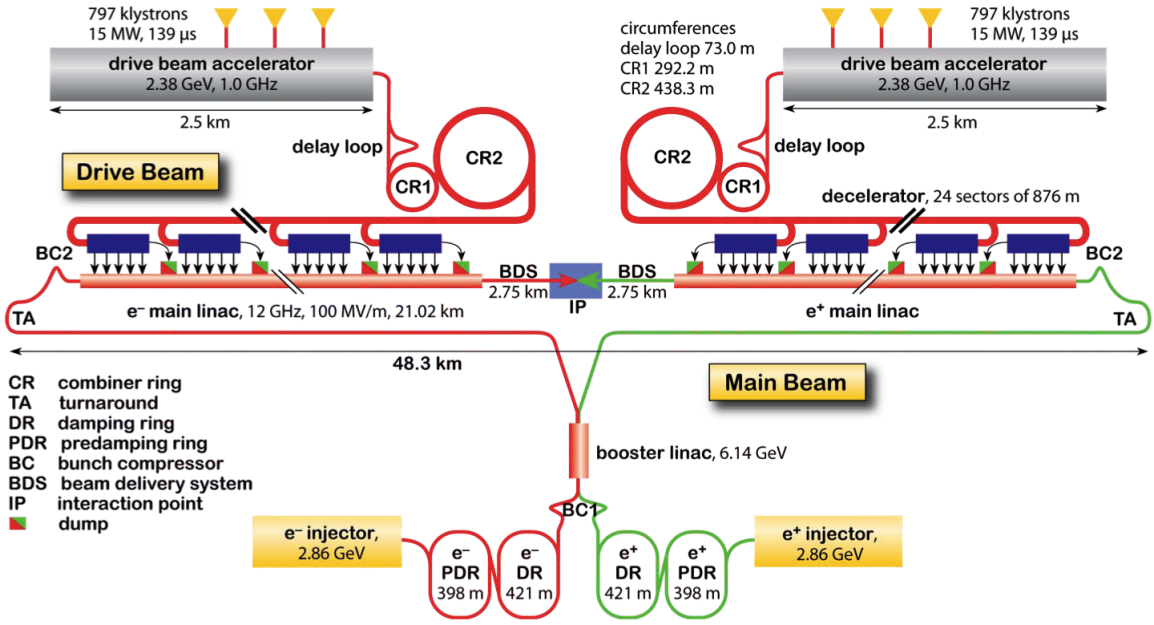

Figure 1.3: A schematic layout of CLIC, indicating all the major subsystems (not to scale).

1.4.2 CLIC

CLIC (Figure 1.3 [18]) is a design for a collider with a much greater centre of mass energy than the ILC. CLIC uses a novel two beam accelerating technique at room temperature. First a high current drive beam (100 A) is accelerated to an energy of 2.38 GeV; this is then decelerated and the energy used to drive a lower current probe beam to an energy of up to 1.5 TeV. The higher energy of the CLIC beam enables the study of more exotic particles than the Higgs.

The technical problems associated with such a design are complex and formidable. As such the CLIC design is currently less developed than that of the ILC. A proof of principle prototype to test the idea of two beam acceleration is located at the CLIC Test Facility (CTF) at CERN [19].

1.4.3 The Raimondi Seryi Final Focus Scheme

Returning to Equation 1.4 and recalling from Table 1.2 the repetition rate of a linear collider would only be of order $5 \leq f \leq 50$ Hz it becomes clear that to achieve a significant luminosity the other parameters in the equation must be optimised. Accelerating a very large number of particles in each bunch becomes impractical as inter-bunch effects result in beam growth and higher bunch charges lead to greater wakefield effects. Linear colliders are therefore designed to have final focus systems that produce a very small beamsize at the IP.

Such systems work by taking an almost parallel beam and using two or more final quadrupole magnets to focus the beam very strongly in both the horizontal and vertical planes. For a beam with an energy spread the chromaticity of these strong lenses will dilute the beam size;

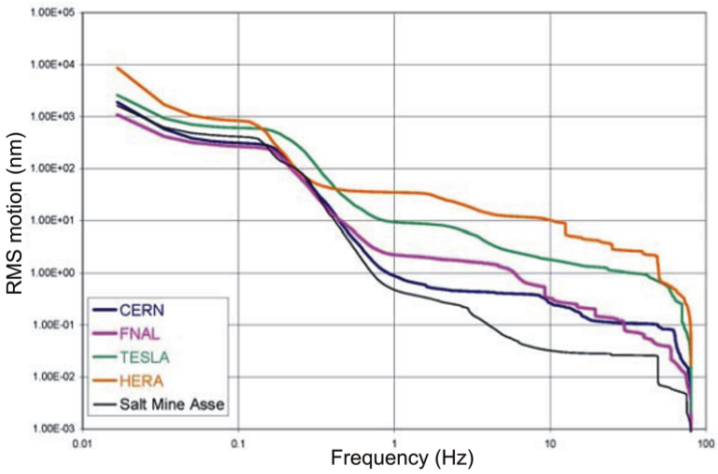

Figure 1.4: Ground-motion vs. frequency for a number of possible accelerator sites.

this problem only increases with energy.

Previous final focus systems - at the SLAC Linear Collider for example - have therefore comprised sections which correct the chromaticity in the horizontal and vertical planes and then sections which focus to a small beam size. Not only do such systems have a considerable length they also have a narrow bandwidth for incoming beam energy.

The Raimondi Seryi Final Focus design for the ILC is a novel final focus system whereby the chromaticity correction is interspersed with the beam size focusing. This not only reduces the length of the system but also improves the incoming beam energy bandwidth. Details of the scheme are given in [20].

1.5 Feedback on Nanosecond Time-scales

1.5.1 Beam Stabilisation at a Linear Collider

As discussed previously the luminosity of a linear collider is of considerable importance. To reach the target luminosity final focus systems that provide vertical beam sizes of order 5 nm or less at the IP are required. When such beam sizes are used the incoming beam-beam alignment is of paramount importance.

Figure 1.4 [21] shows ground-motion vs. frequency at a number of accelerator sites worldwide. Any ground motion which is slow compared to the train repetition rate of the machine (5 Hz) could be corrected by slow pulse-by-pulse feedback systems. Any ground motion above this frequency would have the effect of creating jitter on a pulse-by-pulse basis, this would have to be corrected by some kind of intra-train feedback system. Considering these results it is evident that ground motion of order tens of nanometres could be present at frequencies above 5 Hz. A future linear collider therefore requires an intra-train feedback system. A

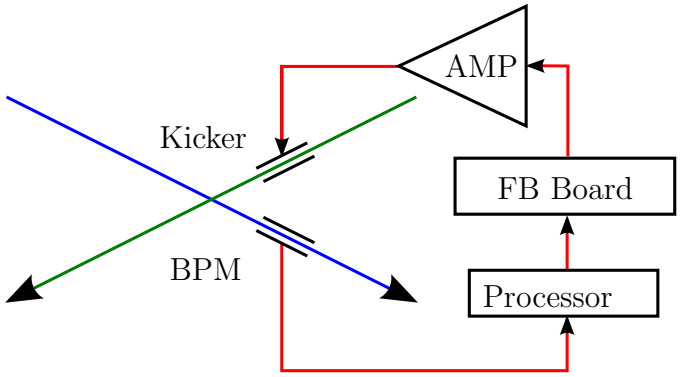

Figure 1.5: A schematic layout of an intra-train feedback system at a future linear collider.

study of how ground motion affects the luminosity at a linear collider is given in [22].

The Feedback on Nanosecond Time-scales (FONT) intra-train feedback system is designed to ensure high luminosity at a future linear collider. It is represented schematically in Figure 1.5 which shows the two incoming beams and the IP where the two beams cross. If two incoming bunches are transversely misaligned they will deflect one another; the deflection of one of the bunches can be measured at some point after the IP using a BPM. The raw signals from the BPM are processed and the misalignment of the two beams is calculated. From this a feedback correction signal is calculated and amplified and a kicker applies the correction to the next bunch of the other incoming beam.

Using such a system all bunches after the initial 'pilot' bunches can be corrected. A delay loop can be implemented on the feedback board ensuring that a deflection is applied to subsequent bunches; in the absence of such a loop the system would interpret the beam correction as evidence that no further kick was required after the initial correction to the first bunch. These concepts are explained further in [21]

The feedback correction can be implemented in either analogue or digital logic depending on the system requirements and bunch spacing. Tests of both types of system have been undertaken and are described below.

1.5.2 Previous Iterations of the FONT Project

Four previous iterations of the FONT project have been designed and tested at different accelerators worldwide. Initial experiments FONT1 and FONT2 were reported in [23] and [24] respectively. Both were based at the Next Linear Collider Test Accelerator (NLCTA) at SLAC in the US which provided a 170 ns bunch-train with a bunch spacing of 87 ps. The systems utilised button BPMs and analogue processing electronics to measure the average position of bunches in an incoming train and apply a correction to later bunches in the train based on this position. These early experiments demonstrated the feasibility of a feedback system operating within a bunch train and showed a 14:1 correction in the beam position with a system latency of 53 ns.

FONT3 was a further analogue system this time based at the Accelerator Test Facility (ATF) at KEK in Japan. The aims of FONT3 were to provide an ultra-low latency feedback system as proof of principle for a CLIC type collider. A 20-bunch train with a bunch spacing of 2.8 ns was used to test new feedback components including a low latency stripline BPM processor with a resolution similar to that required for the ILC and an adjustable gap kicker [25]. The results - reported in [26] and [27] - demonstrated beam stabilisation with a measured system latency of 23 ns.

FONT4 was a second experiment based at the ATF. Here a three-bunch train with bunch spacing of around 150 ns was used to mimic conditions at ILC. The larger bunch spacing relaxes the system latency requirements and enables the use of a digitally implemented feedback algorithm run on a Field Programmable Gate Array (FPGA). This system aimed to provide an independent position correction for the later two bunches in the train both zeroing the position and reducing the jitter on a train by train basis (1.5 Hz). Results from the experiment were presented in [28], [29], [30] and [31] and demonstrated beam stabilisation with a system latency of 140 ns.

1.5.3 FONT5

FONT5 is the current and fifth iteration of the FONT project and is based at the ATF. It is a digital feedback system designed to provide a coupled angle and position feedback correction in the vertical plane. It is based in the extraction line of the ATF but has recently been extended to include experiments in the final focus section of the ATF. Previous results from the upstream position and angle feedback system are presented in [32].

The system is designed around the FONT5 digital feedback board. In its current state it also utilises multiple stripline and cavity BPMs and kickers positioned throughout the ATF beamline, as well as analogue BPM processing electronics and analogue kicker amplifiers. The digital board is described below; the BPMs and kickers in the context of the ATF beamline are described in Section 1.6.3; a detailed discussion of the stripline and cavity BPMs and their processing electronics are given in Chapters 2 and 3 respectively.

1.5.4 The FONT5 Digital Board

The FONT5 board (shown in Figure 1.6) is the basis for the experiments described herein. Designed and built in Oxford it is based around a Xilinx Virtex-5 XC5VLX50T FPGA [33] which is a configurable logic device designed to run programmes written in a hardware description language (firmware). The firmware for the FONT5 board is either loaded from the Xilinx XCF32P [34] programmable read-only memory (PROM) chip located on the board or from the included joint test action group (JTAG) interface which allows direct communication with both the FPGA and PROM.

Each board has nine 14 bit Texas Instruments ADS5474 [35] analogue-to-digital converters

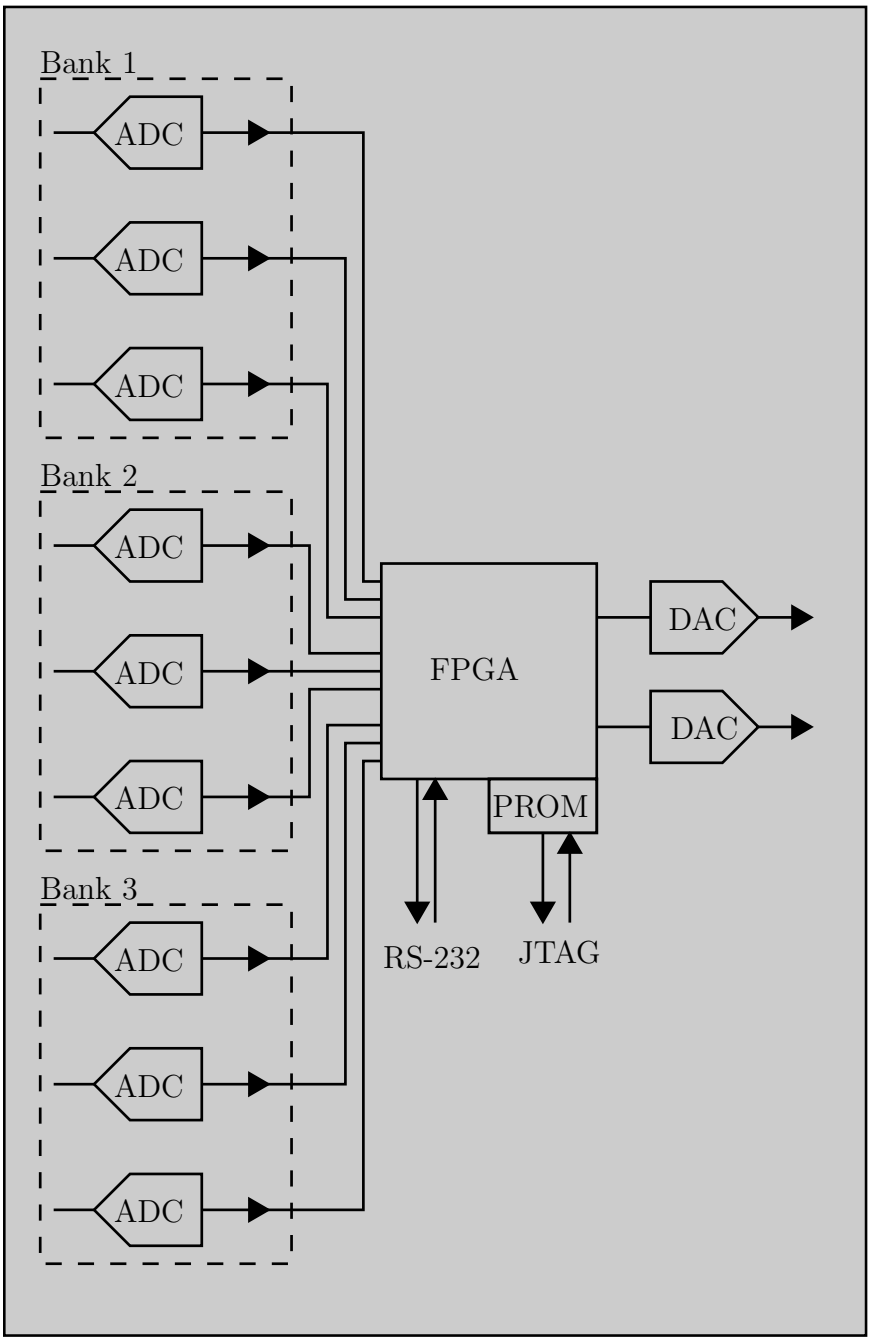

Figure 1.6: A block diagram of the FONT5 board showing the groups of ADCs, the FPGA, the DACs, the PROM, the JTAG and the RS-232 connection.

Parameter	Design Value
Energy	1.28 GeV
Intensity	1×10^{10} electrons/bunch
ϵ_x	1×10^{-9} m rad^{-1}
ϵ_y	1×10^{-11} m rad^{-1}
σ_x	6 μm
σ_y	37 nm

Table 1.3: Design parameters for the ATF.

(ADCs) which can be used to record signals in the range ±1.1 V. The ADCs are grouped in banks of three with each bank sharing a common clock. Signals in the range ±0.5 V can be output from the board using two 14 bit Analog Devices AD9744 [36] digital to anaologue converters (DACs). There are additional digital connections between the FPGA and the front panel of the FONT5 board; these are used for clock and trigger signals.

Finally the board has a RS-232 serial communication for communications with the board in real-time. The connection works in conjunction with a Universal Asynchronous Receiver/Transmitter (UART) which translates data between serial and parallel forms.

Custom designed firmware has been written to run on the FONT5 board. Full details of the firmware along with an in depth discussion of the FONT5 board itself are presented in [21].

1.6 The Accelerator Test Facility

1.6.1 The ATF

The ATF is a particle accelerator based at the High Energy Accelerator Research Organization (KEK) in Tsukuba, Japan [37]. The original goal of the project was to demonstrate a low emittance beam that met the injection requirements of a future linear collider; the project met the requirements in 2001 [38].

A schematic layout of the ATF is given in Figure 1.7 [39]. It consists of a laser driven photocathode RF source; a room temperature linac which accelerates electrons to 1.28 GeV; a 138.6 m circumference racecourse shaped damping ring which relies on radiation damping to reduce the beam's emittance; a fast kicker system to remove damped bunches from the ring and an extraction line for the measurement of the extracted bunches' emittance (ϵ).

The ATF is capable of producing one - two - or three - bunch trains with a bunch spacing between 140 ns and 300 ns. The repetition rate of the machine has recently been upgraded (2012) and is now 3 Hz. A list of some key design parameters of the ATF is given in Table 1.3.

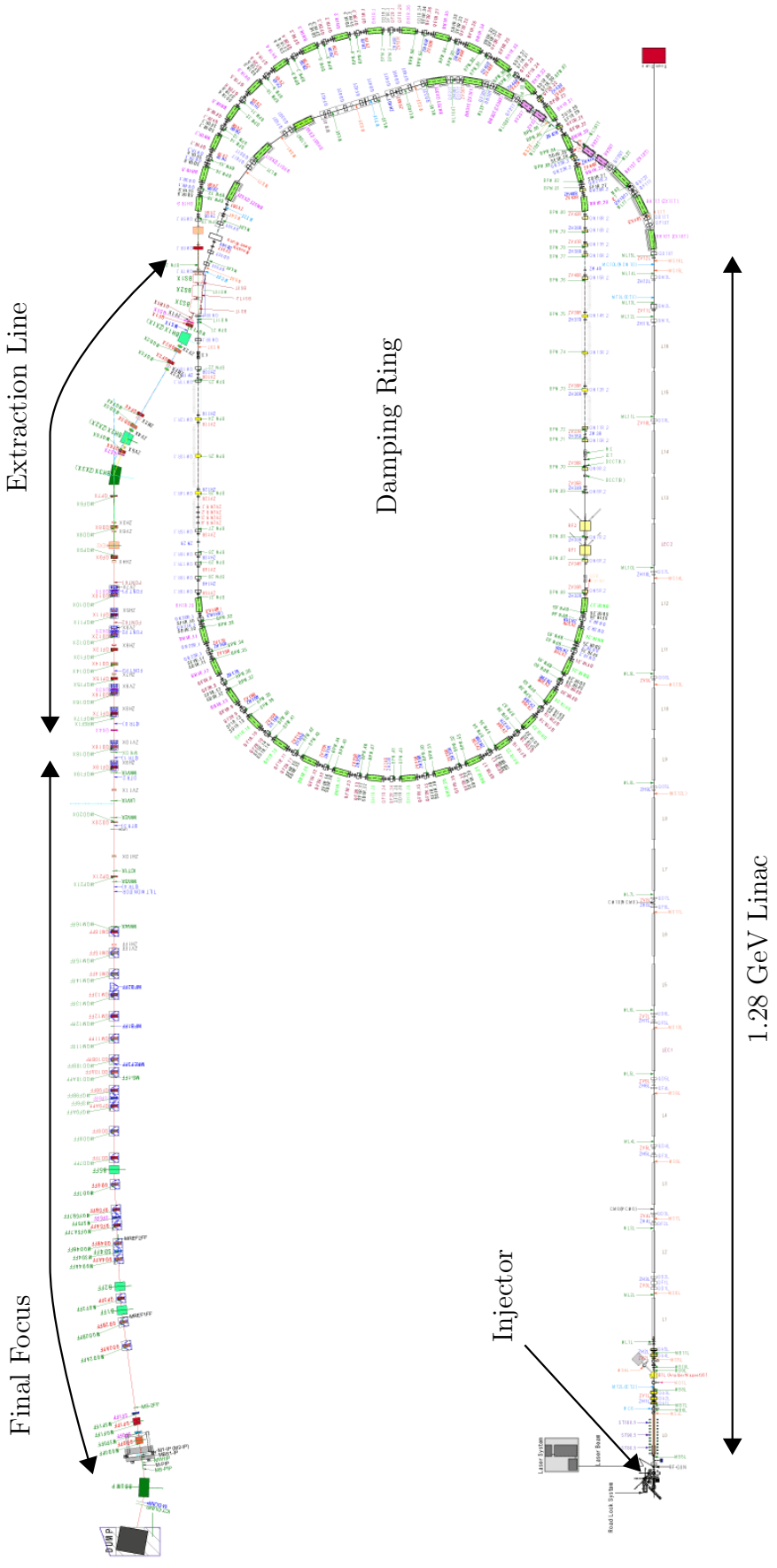

Figure 1.7: Schematic layout of the ATF, indicating all the major subsystems.

1.6.2 The ATF2

The low emittance extracted beams produced by the ATF damping ring provided the perfect opportunity to test another key component of the ILC design - the proposed Raimondi-Seryi final focus scheme. As such the existing extraction line of the ATF was decommissioned in 2007 and replaced with a new final focus test beam-line named the Accelerator Test Facility 2 (ATF2).

The new experiment consisted of an upgraded extraction line to transport the beam from the damping ring; a matching section to transform the extracted Twiss parameters from the damping ring to those required at the entrance to the final focus; sections to adjust for horizontal-vertical coupling and an energy scaled replica of the proposed final focus design for a linear collider.

The ATF2 project has two goals: 1) Demonstrate a compact final focus system capable of achieving and maintaining a beamsize of 37 nm (an energy scaled equivalent of the ILC design value) and 2) demonstrate precise control of this focused beam by stabilising it at the 2 nm nanometer level [40]. To date significant progress has been made in achieving the first of the ATF goals. Recent achievements have demonstrated measured beamsizes of 65 nm and are reported in [41].

The beam size produced by the ATF2 is too small to be measured with a wire scanner which has a resolution approximately that of its width [42]. Hence at the ATF2 IP a novel beam size monitor is installed: the Shintake Monitor is a non-invasive device based on a YAG laser. A detailed description of the physics of the Shintake Monitor is described in [43]; recent results from the Shintake monitor at the ATF2 are presented in [44].

The work described herein is the first attempt at progress towards the second ATF2 goal. The experiments presented demonstrate the validity of a number of possible methods for the stabilisation of the beam at the ATF2 final focus.

1.6.3 FONT5 at ATF2

The FONT5 experiment is based in the extraction and final focus lines of the ATF2. Figure 1.8 shows the components of the upstream system in the extraction line. There are three stripline BPMs each mounted on a two-axis mover system orientated perpendicular to the beam direction. In addition there are two stripline kickers orientated so as to deflect the beam in the vertical direction. These components are interleaved with quadrupoles which make up the ATF2 beamline. The BPMs and kickers are instrumented with a local FONT5 digital board and analogue processing and amplification electronics (not shown). All the components of these systems are discussed in full later.

Figure 1.9 shows the vertical (y) outputs of each BPM, these were connected to a FONT BPM processor which in turn was connected to a FONT5 digital board. The three outputs of each processor were connected to one of the three banks of ADC outputs on the FONT5 board. The FONT5 board was then connected to a serial server inside the tunnel which was in

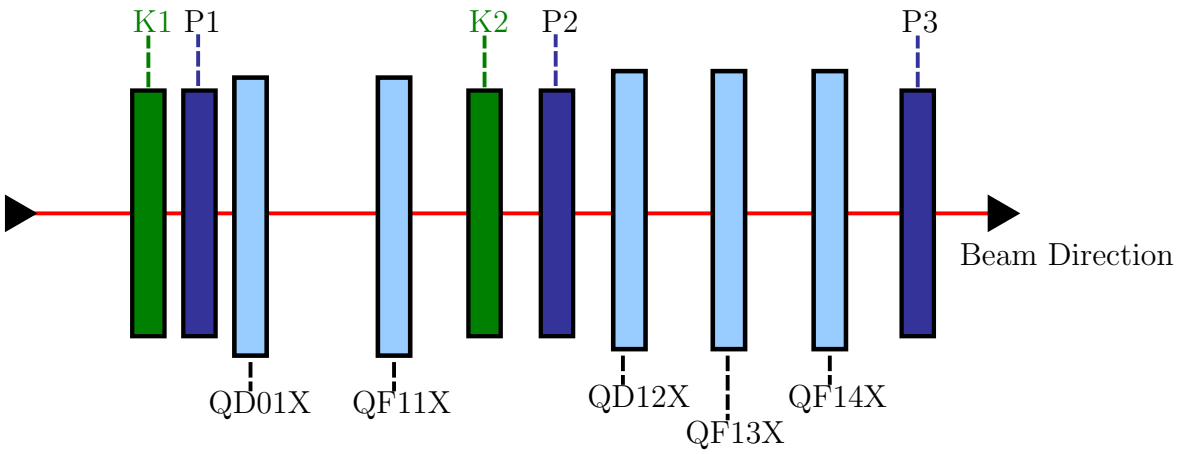

Figure 1.8: A schematic of the upstream system showing the three stripline BPMs P1, P2 and P3; the two stripline kickers K1 and K2; and the ATF quadrupole magnets (light blue).

turn connected to a Microsoft Windows computer via the ATF local Ethernet network. The Labview DAQ was run on the computer and used to send commands to the FONT5 board; LO phase controller box and mover system and record data from the FONT5 board.

Figure 1.10 shows the components of the FONT IP system. A vertically orientated stripline kicker and two cavity BPMs are positioned between the ATF2 final doublet magnets and the nominal IP. A second FONT5 board is located at the IP along with further analogue components (not shown); the setup of the FONT5 board and the other components is discussed in Chapter 6.

Figure 1.11 shows the FONT system in context of the whole ATF2 beamline. The two systems are joined by a long cable - the feedforward cable - which runs parallel to the beamline.

The operation of the upstream stripline BPMs are discussed in Chapter 2 and the cavity BPM system is discussed in Chapter 3. Operation of the upstream feedback system; the feedforward system; and the IP feedback system is discussed in Chapters 4, 5 and 6 respectively.

1.7 Beam Dynamics at a Particle Accelerator

This section will outline some basic concepts in accelerator physics and define certain key parameters. These concepts are used throughout this work and describe the dynamics of a beam of particles in an accelerator.

Beams travelling through an accelerator do not just travel in a continuous stream: the beam is clustered into bunches which can then be easily accelerated; the bunches are made up of individual particles each with its own trajectory. As the bunches pass through the accelerator the trajectory of the particles that make up that beam will vary. The different magnetic elements which make up the accelerator lattice will effect the trajectory of each particle in

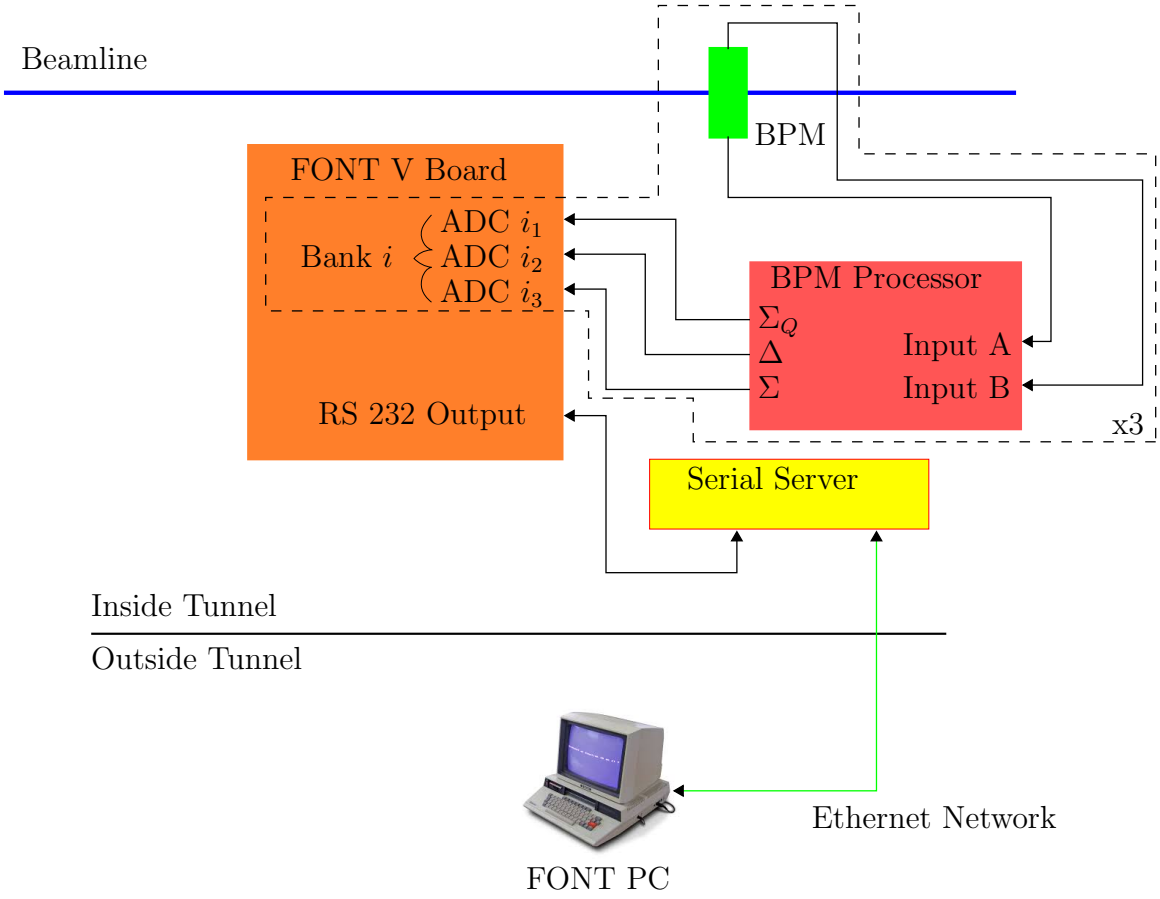

Figure 1.9: A block diagram of the components of the upstream system. i ($1 \leq i \leq 3$) represents the three ADC banks on the FONT5 board.

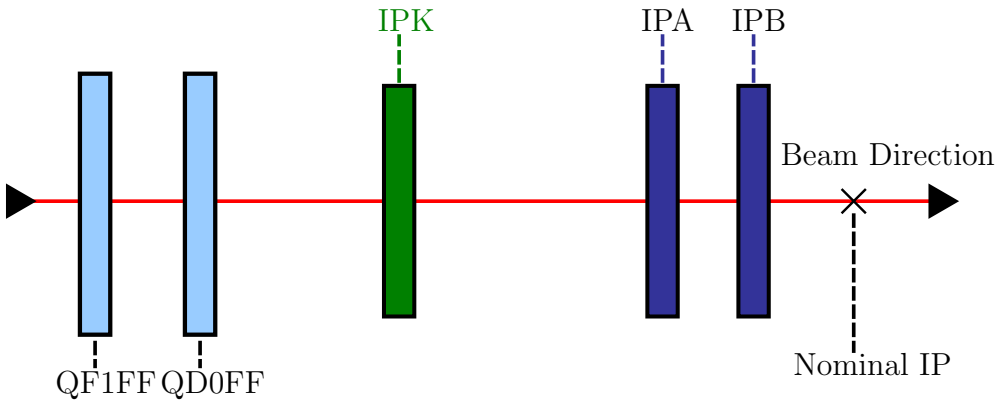

Figure 1.10: A schematic of the IP system showing the two final doublet quadrupoles QD0FF and QD1FF; the local IP stripline kicker (IPK); and the two IP cavity BPMs IPA and IPB.

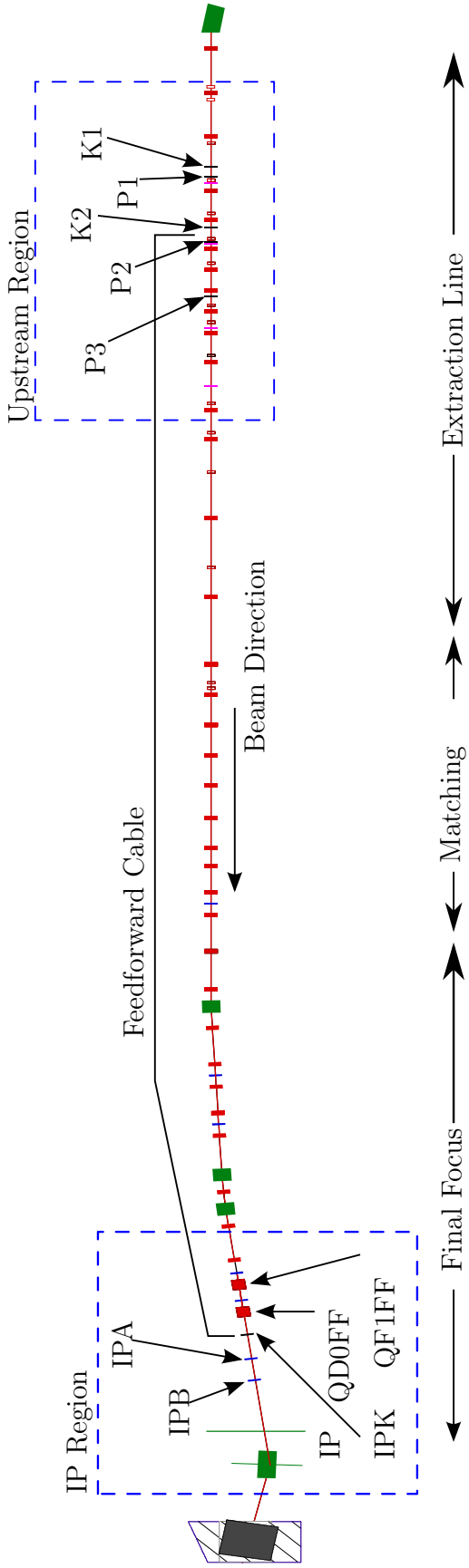

Figure 1.11: A schematic of the feedforward system in the context of the ATF2 beamline showing the upstream region with associated components; the IP region with associated components; and the feedforward cable which joins the two regions.

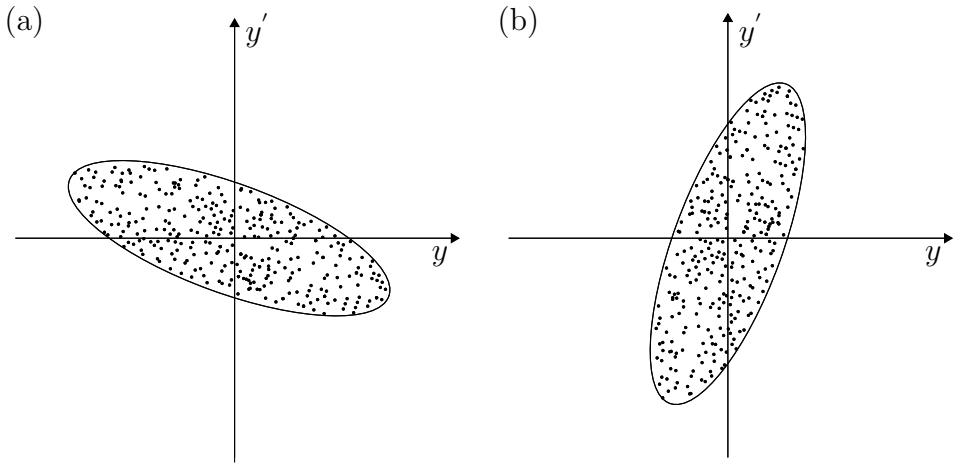

Figure 1.12: $y^{'}$ vs. y for a bunch of particles (a) before and (b) after a quadrupole magnet.

a different way.

If the particles were to travel through the accelerator unconstrained each bunch would disperse outwards over time. Quadrupoles act as focusing elements in the lattice, they alter the trajectory of the particles, compressing them in one plane whilst decompressing them in the other. Alternate focusing and de-focusing quadrupoles placed one after the other form a FODO cell and many cells along a line can transport a beam over long distances without it dispersing.

Considering only one plane in general a magnetic element will affect a bunch's initial angle and position ($y^{(0)}$ and $y^{(0)^{'}}$) resulting in an outgoing angle and position ($y^{(1)}$ and $y^{(1)^{'}}$) and can be described by the transfer matrix $\underline{\underline{M}}$ via

$$\begin{pmatrix} y^{(1)} \\ y^{(1)^{'}} \end{pmatrix} = \begin{pmatrix} m_{00} & m_{01} \\ m_{10} & m_{11} \end{pmatrix} \begin{pmatrix} y^{(0)} \\ y^{(0)^{'}} \end{pmatrix} \tag{1.6}$$

Each element can therefore have an effect on a particle's position or angle or both.

The angle and position of all the particles in a bunch can be shown on a plot of $y^{'}$ vs. y. Figure 1.12 is an example of this with (a) showing an initial distribution of incoming particles. A quadrupole has the effect of converting angular components of the distribution to position and positional components to angle, this will effectively rotate the distribution as shown in (b).

The area of the ellipse governs the beamsize and is defined in terms of the emittance as $\pi\epsilon$. The emittance is a conserved quantity under Liouville's Theorm [45]. It can be reduced using radiative damping in a storage ring.

It is then convenient to denote another parameter β defined as

$$\beta = \frac{\sigma^2}{\epsilon} \tag{1.7}$$

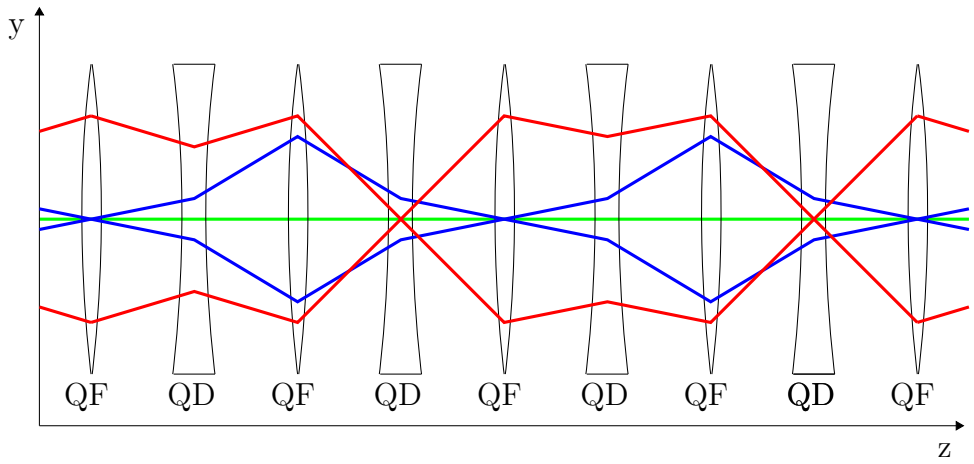

Figure 1.13: Particle trajectory through a FODO lattice for an ideal particle (green) and two non ideal particles (red and blue).

Where σ is the Gaussian width of the beam. The 'beta function' can be used to characterise particle motion through a lattice and for a stable lattice must be non-divergent.

The final key concept mentioned throughout this work is the phase advance, this governs the motion of a particle in the emittance ellipse. Consider the lattice shown in Figure 1.13 made up of FODO cells. An ideal particle will pass through this lattice with a flat trajectory. Non-ideal particles will travel through the machine with trajectories which oscillate around the ideal trajectory. For the lattice shown it takes four FODO cells for one complete oscillation; the phase advance for this lattice cell is therefore 90°. The phase advance of a lattice can be varied by varying the strength of the elements that make up the lattice.

Chapter 2

Improvements to the FONT BPM Processors

The performance of a position feedback system has several hard limits, one of which is the resolution of its BPMs. Work has been undertaken to improve the resolution of the stripline BPMs used in the FONT upstream feedback system.

2.1 Stripline BPMs

Figure 2.1 shows a stripline BPM which consists of two metal strips insulated from the rest of the beam-pipe. This figure also defines the coordinate system used throughout this thesis. The strips are laid along the beam-pipe's cylindrical length (the z-direction) and conform to the beam-pipe's circular cross section. The two strips are placed on opposite sides of the beam-pipe and so together form a symmetric system. Each strip is insulated from the remainder of the beam-pipe and so the end of each strip creates a break in the beam-pipe's electrical continuity. Pickoffs are attached to each stripline from which a signal can be read out.

Figure 2.2 shows the electric field of (a) a stationary electron; (b) a relativistic electron and (c) an ultra-relativistic electron in the rest frame of the laboratory. As the energy of the electron increases the shape of its electric field is Lorentz contracted to an increasingly thin disk, perpendicular to its direction of travel. At the ATF where the electrons have an energy of 1.28 GeV their electric field can be treated as a thin disk.

The flat nature of the resultant field means that the image current induced on the beam-pipe will have a similar time-varying profile to the beam current. The image current integrated azimuthally over the circumference of the beam-pipe will have an equal magnitude and

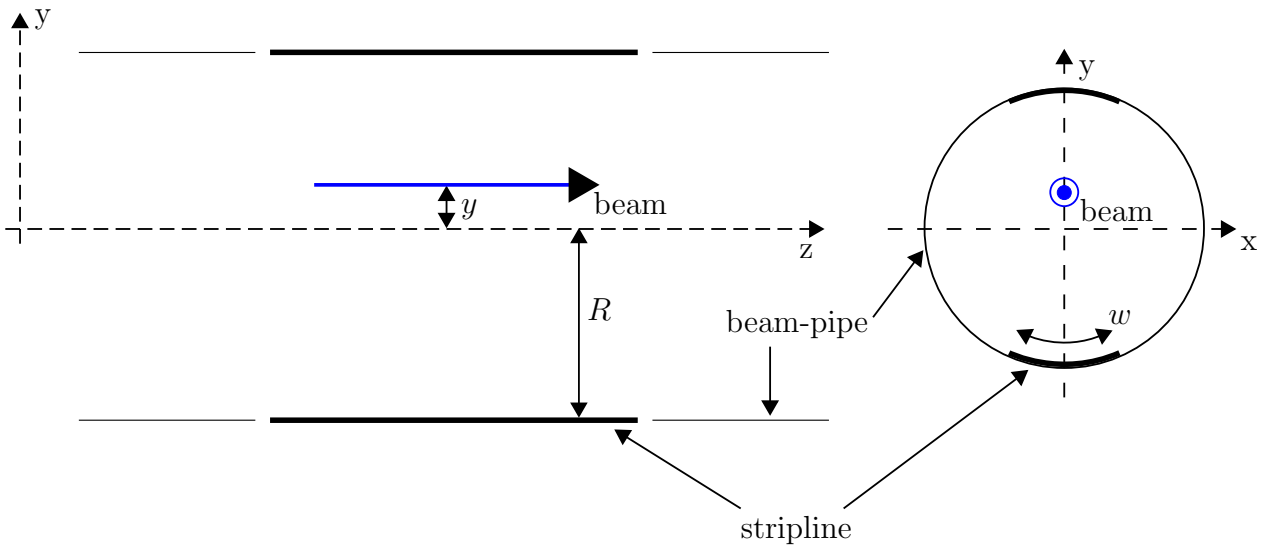

Figure 2.1: A diagram of a beam passing through a stripline BPM. The coordinate system used in this thesis is also shown.

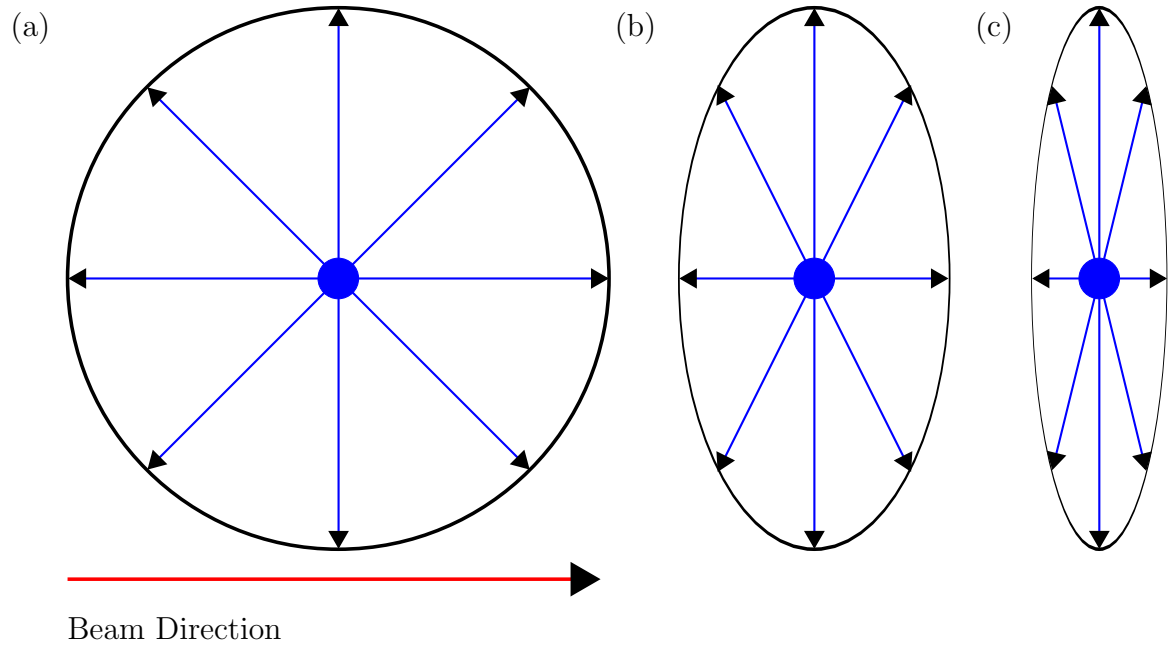

Figure 2.2: The electric field of (a) a stationary electron; (b) a relativistic electron and (c) an ultra-relativistic electron in the rest frame of the laboratory.

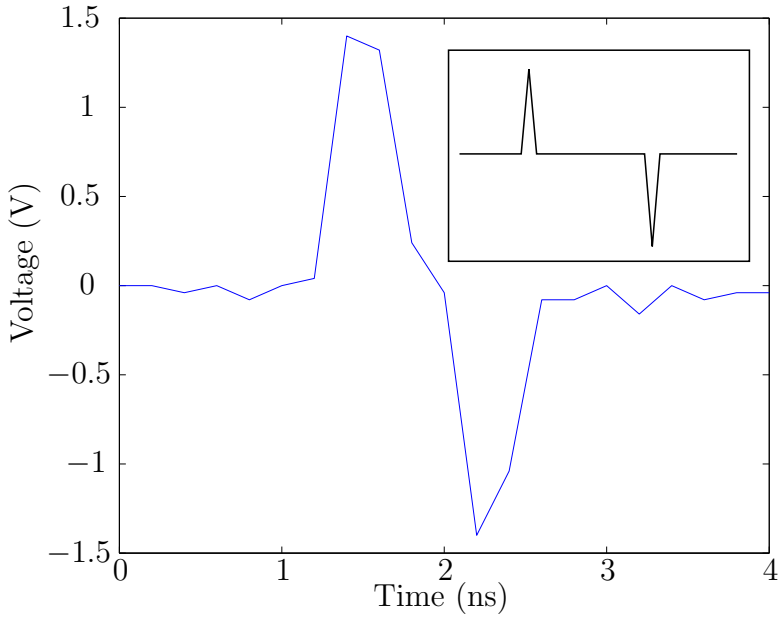

Figure 2.3: The output voltage pulse of a bunch passing through a stripline vs. time, recorded using an oscilloscope. An example of an ideal stripline pulse is given in the box in the top right corner.

opposite sign to the beam charge [46].

Figure 2.3 shows an example of the output voltage pulse of a stripline as a bunch passes through. At the start of the pulse there is a positive voltage spike as the electric field passes across the electrical discontinuity at the beginning of the stripline. There is then a period with no voltage signal as the bunch travels down the length of the stripline. Finally, there is a second voltage spike, of equal magnitude but opposite polarity to the first as the electrical field of the bunch passes over the electrical discontinuity at the end of the stripline. The spikes are of opposite polarity as one corresponds the bunch's electric field passing onto the stripline, and the other corresponds to the bunch's electric field passing off it.

Each stripline BPM at the ATF has two pairs of strips orientated in the horizontal and vertical planes. As discussed in Chapter 1 there are three stripline BPMs dedicated to the FONT project located in the ATF extraction line. A photograph of one of the FONT BPMs is shown in Figure 2.4.

2.2 Stripline Signal Processing

The magnitude of the voltage pulse excited in a single stripline by a beam travelling a distance y from, and coaxially along, its axis is given by [47]

$$V_{peak} \propto \tan^{-1} \frac{w}{2(R-y)} \tag{2.1}$$

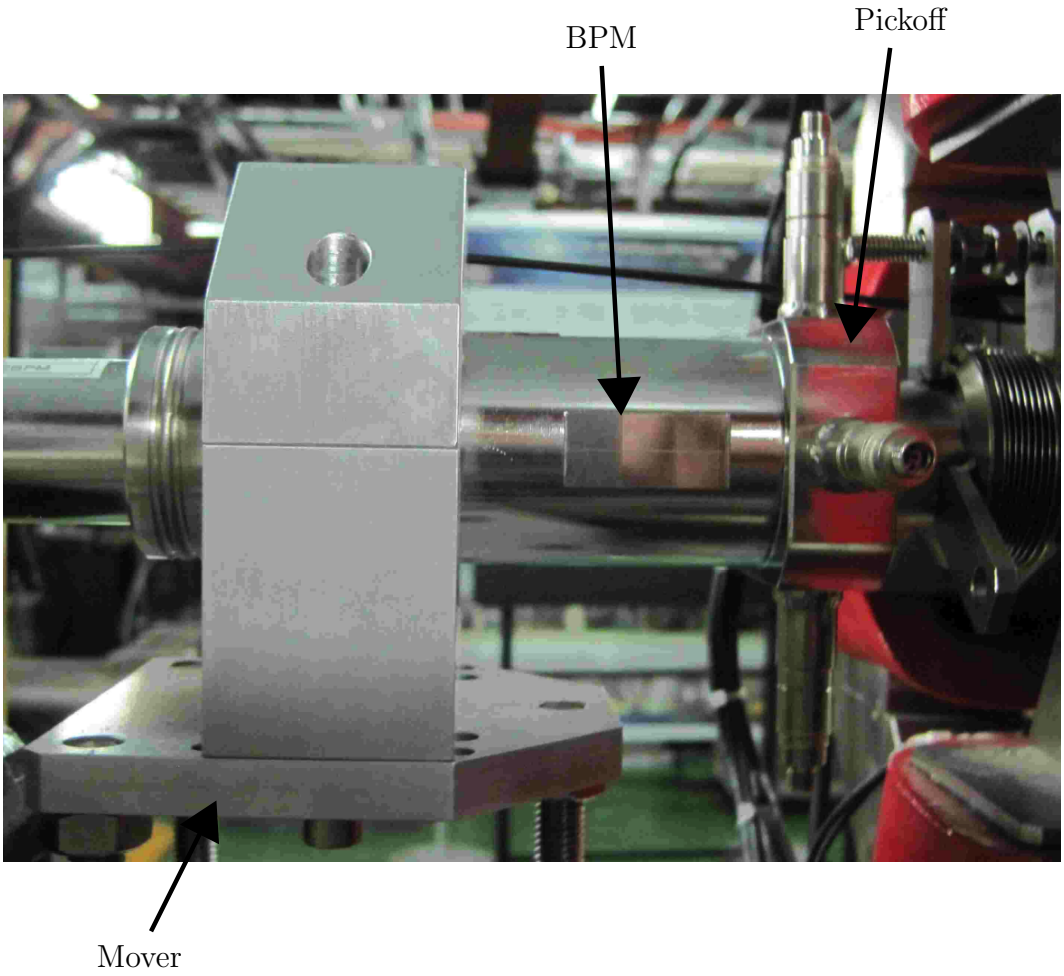

Figure 2.4: A photograph of one of the FONT BPMs in the ATF beamline.

where V_{peak} is the peak amplitude of the output pulse; w is the azimuthal width of the stripline and R is the radius of the beampipe (as defined in Figure 2.1).

Assuming $\frac{\omega}{2(R-y)} << 1$ a Taylor expansion of Equation 2.1 gives

$$V_{peak} \propto \frac{w}{2(R-y)} - \frac{w^3}{24(R-y)^3} + \frac{w^5}{160(R-y)^5} + ... \tag{2.2}$$

The dimensions of the ATF BPMs are given in Figure 2.5 [48]; the radius of the BPM is marginally greater than the width of the striplines; additionally efforts are made to centre the beam in the BPM i.e. $y \approx 0$. Equation 2.2 therefore approximates to

$$V_{peak} \propto \frac{w}{2(R-y)} \tag{2.3}$$

If two striplines are then located on opposite sides of a beampipe, the signals can be written as

$$V_{top} = f(t)q\rho\frac{w}{2(R+y)} \tag{2.4}$$

$$V_{bot} = f(t)q\rho\frac{w}{2(R-y)} \tag{2.5}$$

where V_{top} and V_{bot} are the signals from the top and bottom striplines respectively; $f(t)$ is the function that defines the shape of the output pulse; q is the bunch charge and ρ is the impedance of the measurement electronics.

Subtracting Equation 2.5 from Equation 2.4 gives

$$V_{bot} - V_{top} = f(t)qwy\rho\frac{1}{(R^2-y^2)} \tag{2.6}$$

which approximates to

$$V_{bot} - V_{top} = f(t)qwy\rho\frac{1}{R^2} \tag{2.7}$$

when $y << R$. Summing Equations 2.4 and 2.5 gives

$$V_{top} + V_{bot} = f(t)qwR\rho\frac{1}{(R^2-y^2)} \tag{2.8}$$

which approximates to

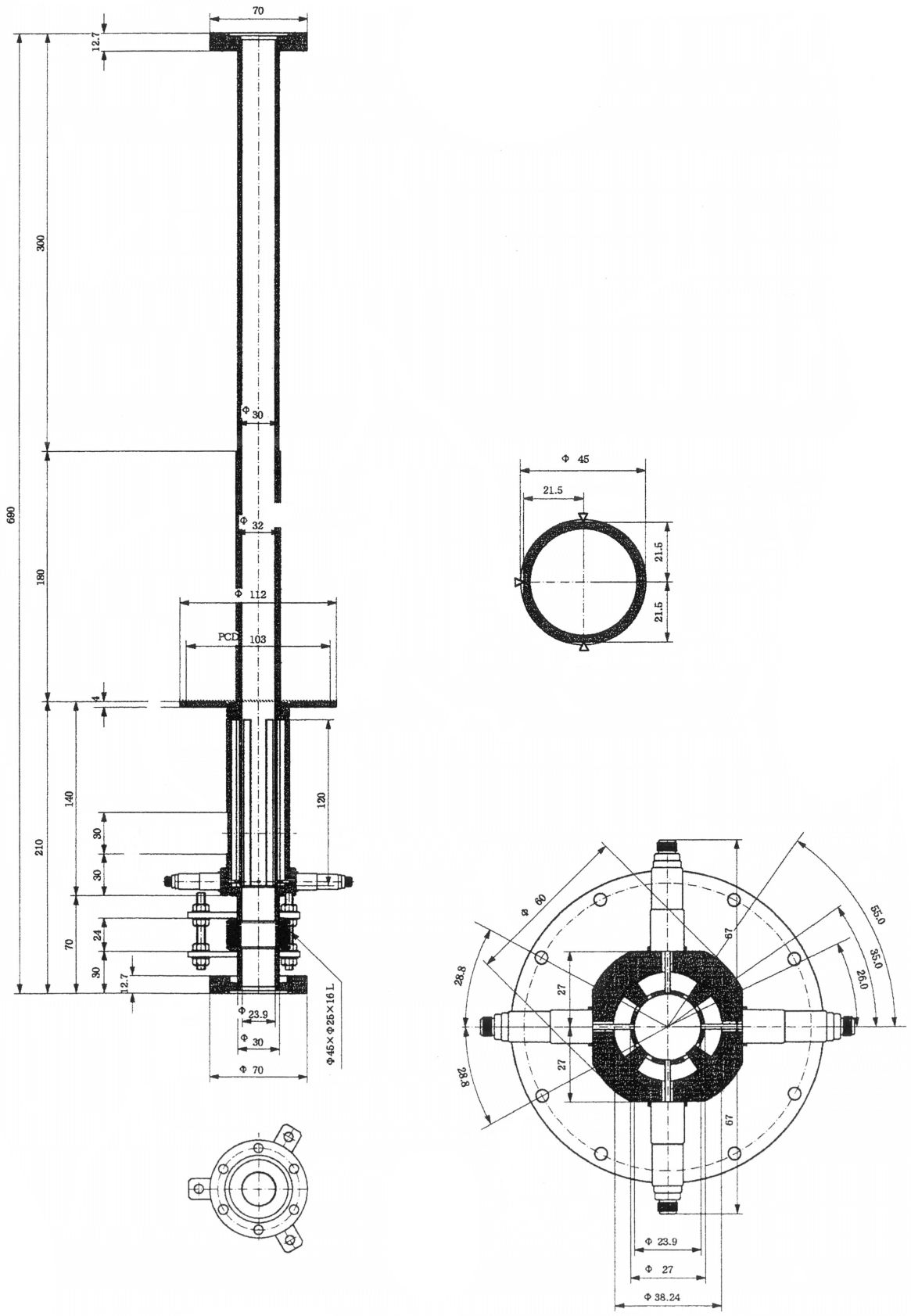

Figure 2.5: A technical drawing of the ATF stripline BPMs.

$$V_{top} + V_{bot} = f(t)qwR\rho\frac{1}{R^2} \tag{2.9}$$

when $y << R$. Dividing Equation 2.7 by Equation 2.9 gives

$$\frac{V_{top} - V_{bot}}{V_{top} + V_{bot}} = \frac{y}{R} \tag{2.10}$$

This is the so called difference over sum method for calculating the beam position from a stripline BPM. The position can then be calculated from

$$y = \kappa\frac{\Delta}{\Sigma} \tag{2.11}$$

where $\Delta \equiv V_{top} - V_{bot}$; $\Sigma \equiv V_{top} + V_{bot}$ and κ is a calibration constant calculated by either moving the position of the BPM a known amount using the FONT mover system [49] or by measuring the change in position when the beam is deflected by a known amount. Δ and Σ are calculated in an analogue BPM signal processor.

Due to the approximations made this method of calculating the position will only work when the beam has a small offset from the centre of the BPM. During the experiments throughout the beam was centred to better than 100 μm, tests detailed in [50] have demonstrated that the BPMs still perform well within this range.

2.3 The FONT BPM Processors

The FONT experimental setup utilises analogue signal processors which take two raw signals from the top and bottom outputs of a stripline BPM and produce Σ and Δ signals at baseband. These analogue BPM processors are constructed from off the shelf components fitted together on an in-house designed PCB. A photograph of one of the FONT BPM processors is shown in Figure 2.6. The processing scheme is split into several separate stages, each described below. A block diagram of the complete scheme is shown in Figure 2.7.

2.3.1 The Components of the FONT BPM Processing Scheme

The first stage of the processing scheme comprises low pass filters [51](LPF) with a cut-off frequency of 1 GHz. These filters - applied to both input channels - cut out high frequency noise whilst leaving the raw stripline signals unaffected.

A resistive coupler network - shown in Figure 2.8 - is then used to produce the Σ signal. The network sums all frequencies identically. The Δ signal is calculated using a 180° hybrid [52] to shift the phase of one of the channels by 180° before summing it with the other channel.

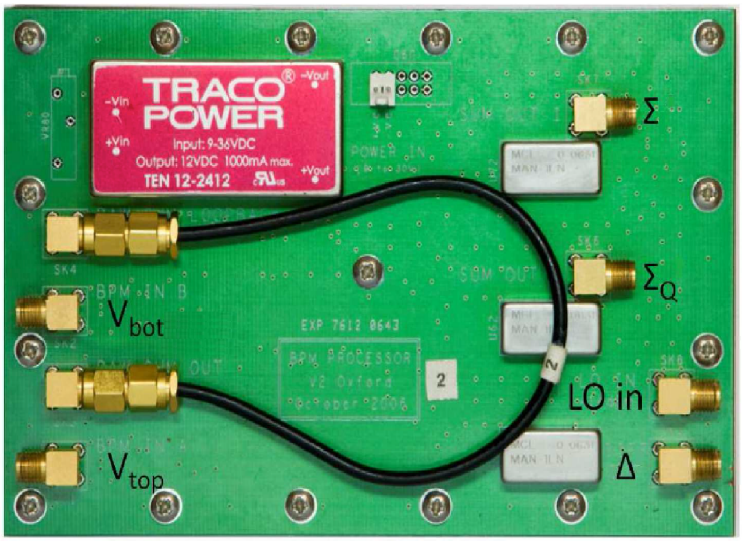

Figure 2.6: A photograph of a FONT BPM processor.

By design the power output of the stripline in the frequency domain peaks around 625 MHz. The Nyquist limit of the ADCs on the FONT5 board is approximately 180 MHz and therefore, to avoid aliasing, the bandwidth of the hybrid output should be shifted below this. A low pass filter would do this satisfactorily, however it would block out most of the power, thereby decreasing the signal to noise ratio and hence the resolution. Instead the Σ, Σ_Q (discussed later) and Δ channels are each passed through a 200 MHz bandpass filter centred at 714 MHz, further reducing extraneous noise [53], and then a mixer [54].

Each mixer outputs the product of the BPM signal and a reference, or local oscillator (LO), signal:

$$V_{out} = A_I A_{LO} \cdot \sin(\omega_I t) \cdot \sin(\omega_{LO} t) \tag{2.12}$$

where ω_I and ω_{LO} and A_I and A_{LO} are the angular frequencies and amplitudes of the input and LO signals respectively. When the frequency of the LO signal is selected to be similar to that of the input $\omega_I \approx \omega_{LO} \approx \omega$ so Equation 2.12 approximates to

$$V_{out} = \frac{A_I A_{LO}}{2}[\cos(\phi) - \cos(2\omega + \phi)] \tag{2.13}$$

where ϕ is the phase difference between the input and LO signals. This produces an output signal with a down-mixed DC component proportional to $\cos\phi$ and an up-mixed AC component with a frequency double that of ω.

The final stage of the processing scheme is a low-pass filter designed to remove the up-mixed high frequency component leaving only the down-mixed DC signal. A Chebyshev filter was selected for the processing scheme as it has a strong suppression of frequencies outside its passband [49].

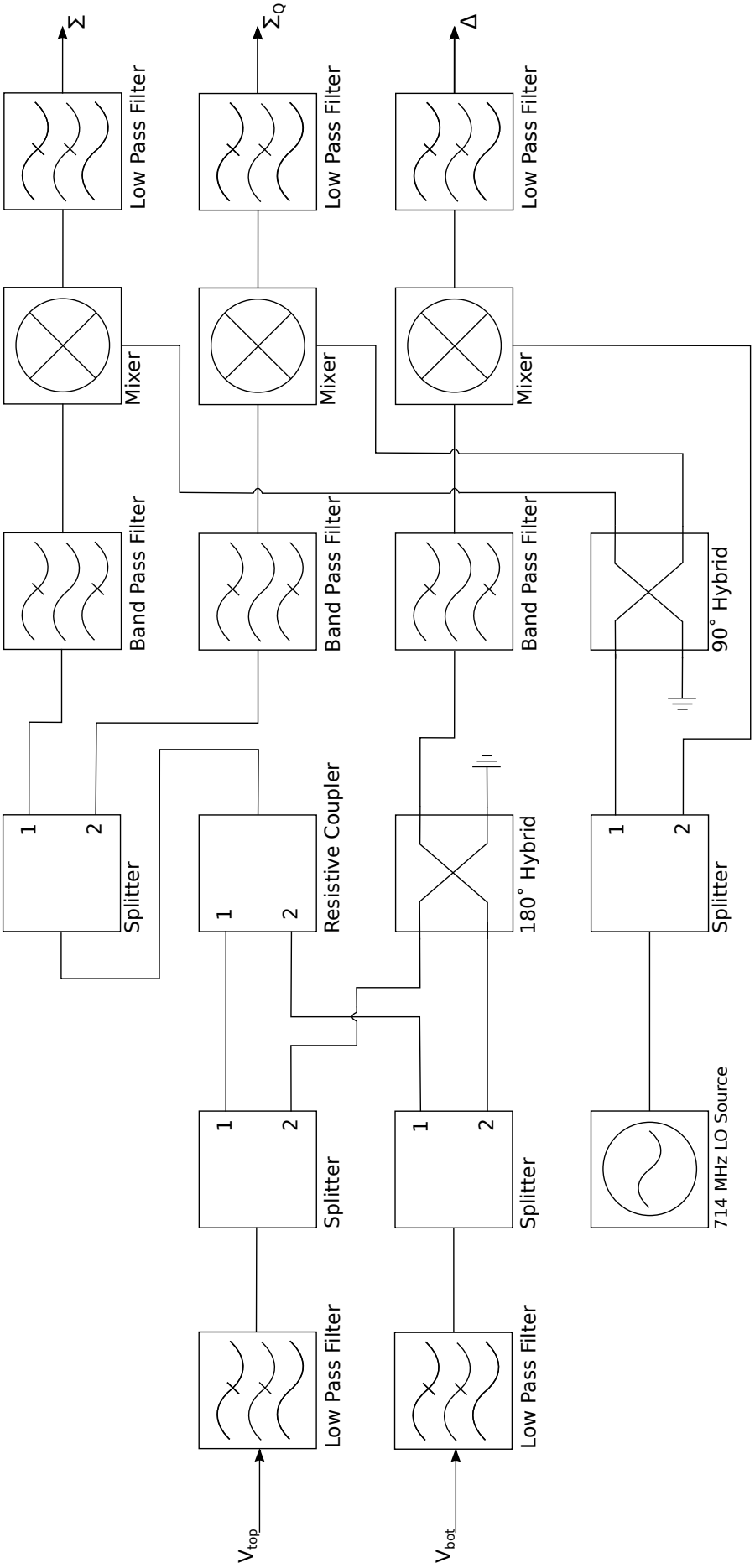

Figure 2.7: A block diagram of a FONT BPM processor.

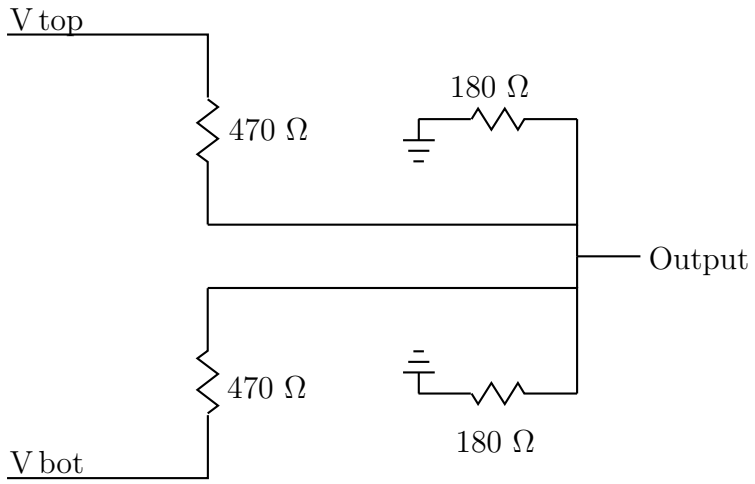

Figure 2.8: Circuit diagram of the resistive couple network used in the Σ channel of the FONT BPM processors.

As V_{out} also has a dependence on the phase ϕ it is important to synchronise the LO signal with the arrival of each bunch so that ϕ remains constant. The LO signal frequency was therefore chosen to be 714 MHz as this is the R.F. of the ATF damping ring [55] and thus sets the ATF bunch timing. Additionally there is a convenient distribution of 714 MHz signals locked to the damping ring R.F. distributed around the ATF. Hence 714 MHz was chosen as the centre of the band-pass filter to get the highest possible signal power output from the processor.

2.3.2 The Σ_Q Output

In addition to the Σ output each processor also provides a Σ_Q output used as a measure of the phase difference (ϕ) (see Section 2.7.1). This signal is formed by splitting the Σ signal before it is down-mixed. One signal is then down-mixed to form the Σ output; the other is down-mixed using a LO signal that has been phase shifted using a 90° hybrid, this forms the Σ_Q output.

2.3.3 Setup of the FONT BPM Processors

Examining Equation 2.13 and ignoring the high frequency components the output of the processor is

$$V_{out} = \frac{A_I A_{LO}}{2}[\cos(\phi)] \tag{2.14}$$

This equation can be thought of as containing two parts: A_I which contains the information from the BPM signal and $A_{LO}[\cos(\phi)]$ which contains information from the LO signal.

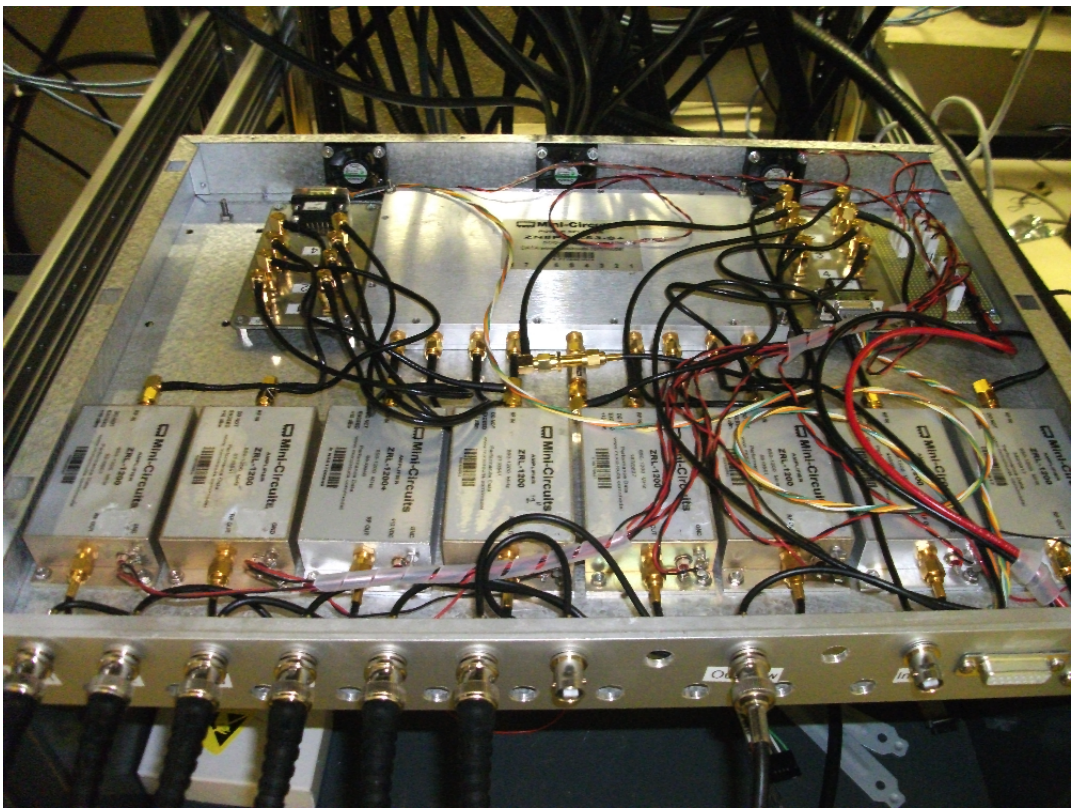

Figure 2.9: A photograph of the LO signal distribution box.

Ideally the output of the processor should depend only on A_I. It is important therefore to have an LO signal which is stable in both amplitude and phase. Additionally to produce the maximum voltage output the LO signal should be of enough power to drive the mixer properly (14 ± 1 dBm [53]) and be correctly phased with the bunch arrival ($\phi = 0 + n\pi$).

A distribution box was built to provide LO signals for up to 6 processors; each output signal was designed to have the correct power level and an independently adjustable phase. The LO signal distribution box is shown in Figure 2.9. The ability to provide a global phase shift to all channels, referred to as the master LO phase, was also provided.

At the start of each shift the phase of the LO signal for each BPM processor was adjusted or 'phased' to maximise the Σ signal. This was initially done by eye but was later automated in the FONT DAQ system described in [50].

2.4 Features of the BPM Processing Scheme

As discussed in Section 2.3.3 the magnitude of the processor output is dependent on both the amplitude and phase of the LO signal. Problems arise in the FONT processing scheme if the phase is not perfectly stable with respect to the bunch arrival. Synchrotron oscillations in the ATF damping ring cause small changes in the arrival time of the bunch with respect to the 714 MHz signal used as the LO; this manifests itself as a small variation in the relative

LO phase ϕ.

2.4.1 Position Sensitivity to LO Phase Jitter

The position is calculated by dividing Δ by Σ (Equation 2.11). If the signals from both striplines arrived at the mixer simultaneously a jitter in the LO phase with respect to the beam would not cause an apparent position difference: both the sum and difference signals would be affected identically and their ratio would remain unchanged.

In the processors however, due to inherent differences in their construction and the cables that connect them to the striplines, there is likely to be some path length difference between the two input channels. This results in each channel having a slightly different phase with respect to the LO signal. If the LO phase jitters this will manifest itself in an apparent jitter in beam position.

The change in output of the sum and difference channels due to LO phase jitter is given by [49]

$$\Sigma = \frac{\sqrt{V_{top}^2 + V_{bot}^2 + 2V_{top}V_{bot}\cos(2\theta)}}{2} cos\left[\delta\phi - \tan^{-1}\left(\frac{V_{top} - V_{bot}}{V_{top} + V_{bot}}\tan(\theta)\right)\right] \tag{2.15}$$

and

$$\Delta = \frac{\sqrt{V_{top}^2 + V_{bot}^2 - 2V_{top}V_{bot}\cos(2\theta)}}{2} \cos\left[\delta\phi - \tan^{-1}\left(\frac{V_{top} + V_{bot}}{V_{top} - V_{bot}}\tan(\theta)\right)\right] \tag{2.16}$$

where $\delta\phi$ is the LO phase jitter and θ is the path difference between the two stripline channels in units of LO phase. If the beam is roughly centred $V_{top} \approx V_{bot}$. Combining Equations 2.15 and 2.16 gives an apparent change in position δy of

$$\delta y = \kappa \tan(\theta)\tan(\delta\phi) \tag{2.17}$$

when k is the calibration constant from Equation 2.11.

2.4.2 LO Phase Jitter at ATF

At ATF synchrotron oscillations in the damping ring cause jitter in the bunch arrival time with respect to the 714 MHz clock that is used as the LO signal; additionally cooling water cycles cause a gradual sinusoidal drift. The LO phase difference vs. time during a typical 1000 trigger data run has been calculated using the Σ_Q channel and Equation 2.24 and is

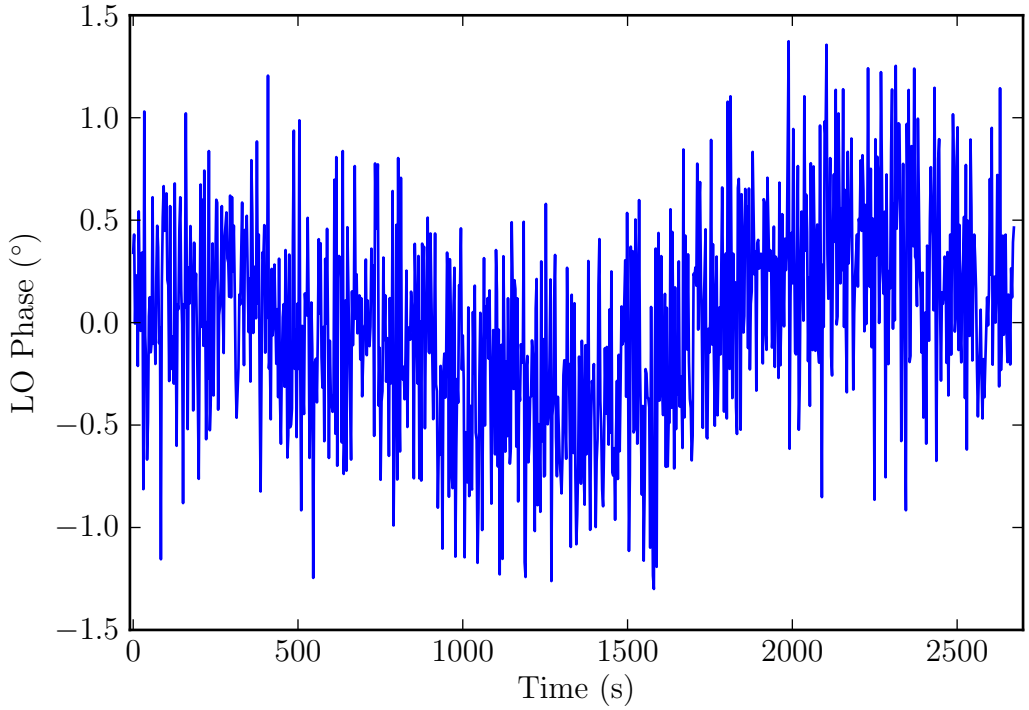

Figure 2.10: LO phase drift vs. time during a 1000 trigger data run.

shown in Figure 2.10. It shows that the bunch remains stable in average phase, but jitters around the mean phase by 0.49°.

2.4.3 Effects of a 0.5° LO Phase Jitter on Resolution

If $\theta \neq 0$ then a LO jitter would manifest itself as an apparent beam jitter; this would be indistinguishable from real beam jitter and hence would have a degrading effect on the BPM's resolution. For example if $\theta = 4.3°$ (a 5 mm path length difference) a LO phase jitter of 0.5° would result in an apparent beam jitter of approximately 0.8 μm. If θ were reduced to 0.43° mm (a 0.5 mm path length difference) the apparent position jitter would become approximately 0.08 μm. The theoretical resolution limit of the BPMs due to electrical noise (discussed later) is approximately 0.25 μm, reducing the apparent position jitter to 0.08 μm would therefore effectively negate its contribution to eh BPM resolution.

These results were cross checked with simulations run using the program SPICE [56]. A basic model of the BPM processor created by C. Perry was modified to calculate the effect of an LO phase jitter of 0.5°. The simulations yield position jitters of 0.9 μm and 0.09 μm with cable path length differences of 4.3° and 0.43° respectively.

BPM	Phase Sensitivity (μm / °)	Contribution to σ (μm)
P1	-7.41 ± 0.06	2.99 ± 0.02
P2	-2.66 ± 0.04	1.11 ± 0.02
P3	-0.94 ± 0.02	0.35 ± 0.01

Table 2.1: The position sensitivity to LO phase jitter and the contribution of this jitter to the BPM resolution (σ) for the upstream FONT BPMs. The errors represent the statistical uncertainty on the results.

2.4.4 Measuring the Sensitivity to LO Phase Jitter

Due to its potential importance as a degrading effect on the position resolution a standard test was devised to measure a BPM processor's sensitivity to LO phase jitter. First the beam was centred in the FONT BPMs and the LO signal was phased via the method described in Section 2.3.3. A 50 trigger data run was taken, the master LO phase was shifted by 10° and another 50 trigger data run was taken. The phase was then shifted back to nominal and another data run taken before the phase was shifted in the other direction by 10° and a final data run taken. This process was repeated and the average apparent position for each data run calculated. The results from such a test are shown in Figure 2.11.

The position shifts between the maximum and minimum settings. A linear fit can be applied to the data for each BPM and used to measure the BPM's position sensitivity to LO phase jitter. Table 2.1 gives the apparent change in position for a one degree change in LO phase; the phase jitter over the run was also measured and the contribution to the resolution by the phase sensitivity calculated, also shown in Table 2.1. Finally examination of the data points with the master LO phase set to zero suggests a small sinusoidal oscillation; this is an artefact of the slow drift in the LO signal over time due to the cooling water.

2.5 Reducing the Sensitivity of the Processors to LO Phase Jitter

For a given BPM the position dependence on LO phase jitter can be corrected by minimising the path length difference between the two stripline channels. The external cables that connect the processor to the striplines were used to provide a correction. For each processor properly matched pairs of cables were fabricated that were of appropriate length to cancel any internal path length difference in the processor between the two stripline channels.

To make measurements of the internal path length difference of each BPM processor an experimental setup was created in the lab that was designed to mimic conditions at ATF. Apparatus to generate a simulated stripline signal along with a synchronised LO signal with phase adjustment was constructed. The experimental setup is shown in Figure 2.12.

A signal generator provided a stable 714 MHz LO source. The output was split using a

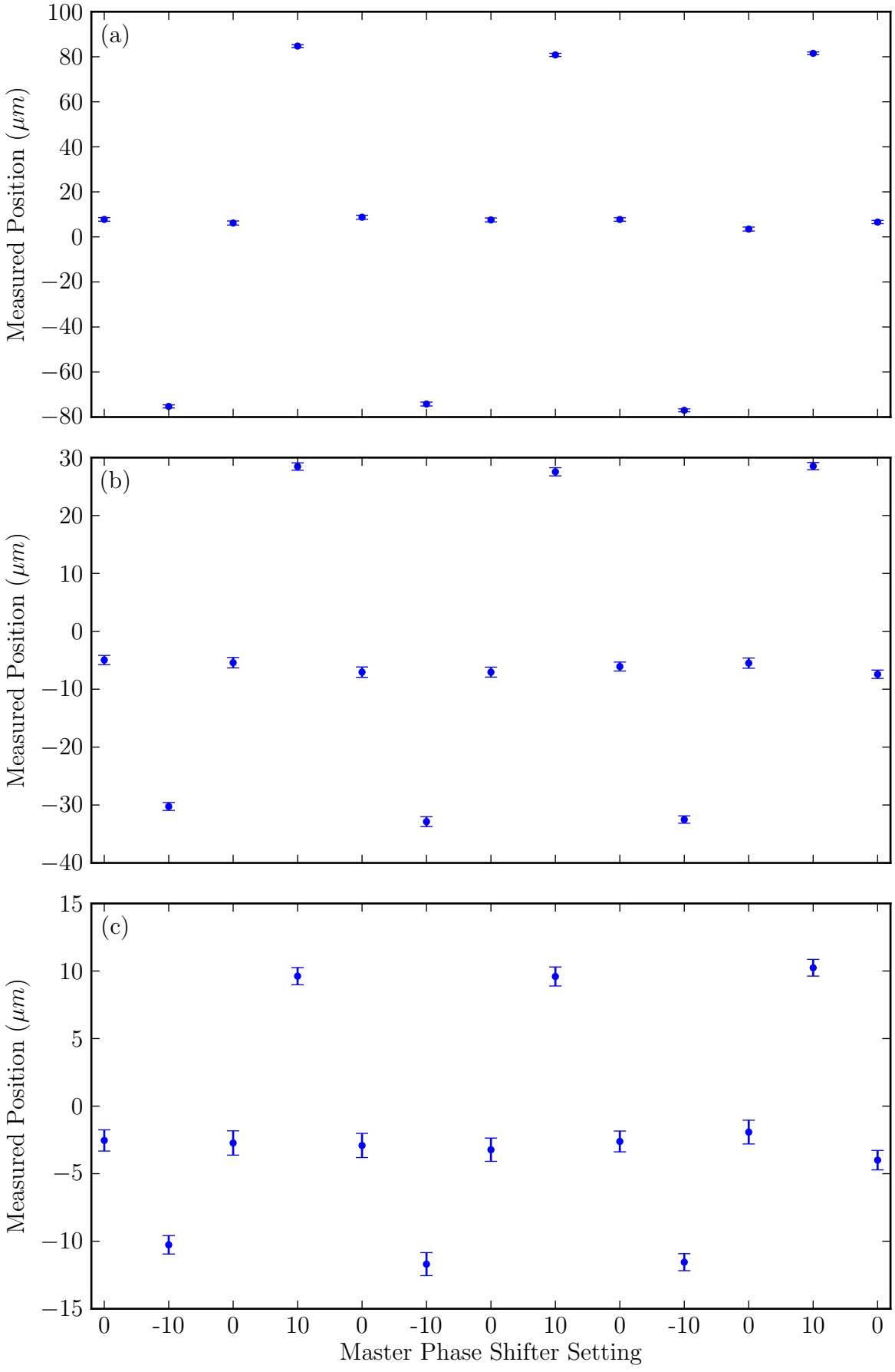

Figure 2.11: Apparent position at (a) P1, (b) P2 and (c) P3 vs. master LO phase setting during a LO phase scan. The error bars represent the statistical uncertainty on each point.

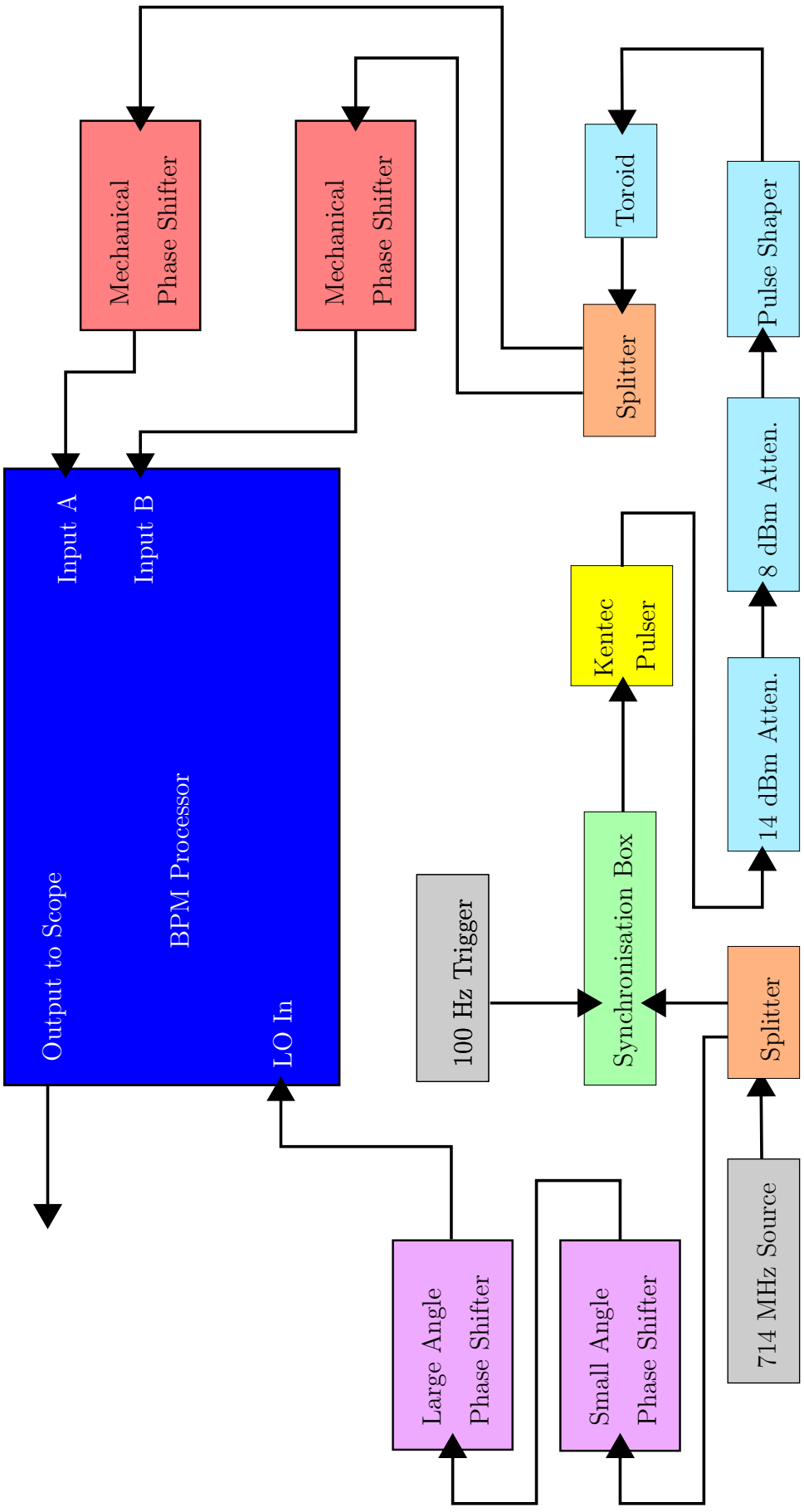

Figure 2.12: A block diagram of the experimental setup used to generate an imitation stripline pulse.

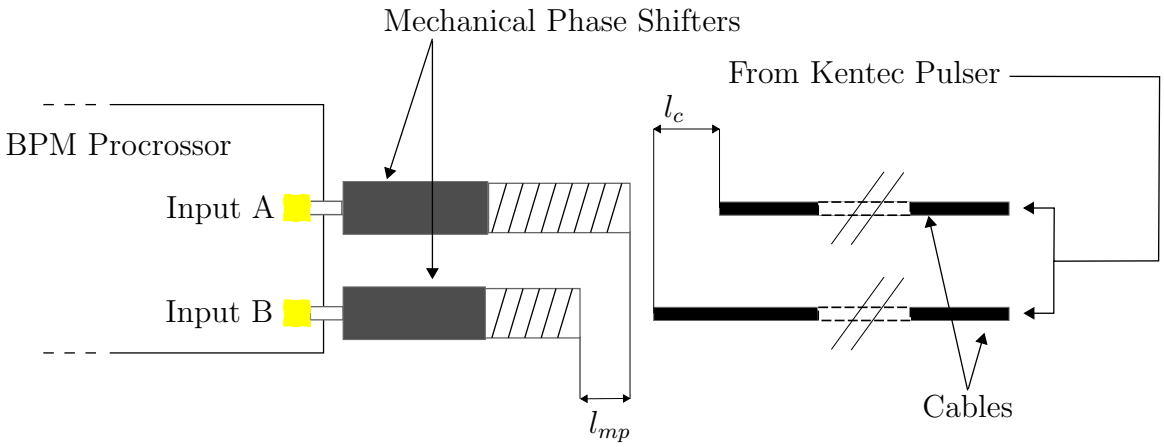

Figure 2.13: The experimental setup connecting each BPM processor to the Kentec pulse generator.

resistive splitter; one half was relayed through large and small angle phase shifters before being input as the LO signal to the processor; the other half was used as the input to a setup for generating an imitation stripline pulse.

The latter consisted of an in-house built synchronisation unit which took as inputs the LO signal (prior to being phase shifted) and a 100 Hz trigger. The output of the box was a LO-synchronised 100 Hz trigger pulse input to a Kentec PBG1 high voltage pulse generator. The high voltage pulse was attenuated via 14 dBm and 8 dBm attenuators before being sent through a copper foil shielded pulse shaping network and ferrite toroid to reduce high frequency interference. This pulse was split and input into the two stripline channels via mechanical phase shifters, one on each channel, as shown in Figure 2.13. The difference in path length introduced by the mechanical phase shifters was defined as l_{mp}.

The dielectric path lengths of 40 specially purchased nominally 1 m cables were measured using a network analyser. The connections between the splitter and mechanical phase shifters were made using two of these cables; the difference between the lengths of two cables was referred to as l_c. Initially l_c was set to zero by selecting two cables of the same length and l_{mp} was set to zero by adjusting the mechanical phase shifters. The LO signal was then adjusted using the large angle phase shifter so that the Σ_Q output of the processor was at a minimum, and therefore the Σ and Δ signals were at their maxima. One of the two stripline channels on the BPM processor was then disconnected and terminated and the time at which the Δ signal peaked, t_p, was measured with an oscilloscope.

This channel was reconnected, the LO phase was shifted in turn by $+9°$ and $-9°$ using the small angle phase shifter and a measurement of the difference signal was taken at both phases yielding D_1 and D_2. The difference residual D_r was calculated via

$$D_r = D_1 - D_2 \tag{2.18}$$

and the value of D_r at t_p was noted.

l_{mp} was then varied with a range of $\pm$ 4 mm around 0 by changing the length of the mechanical

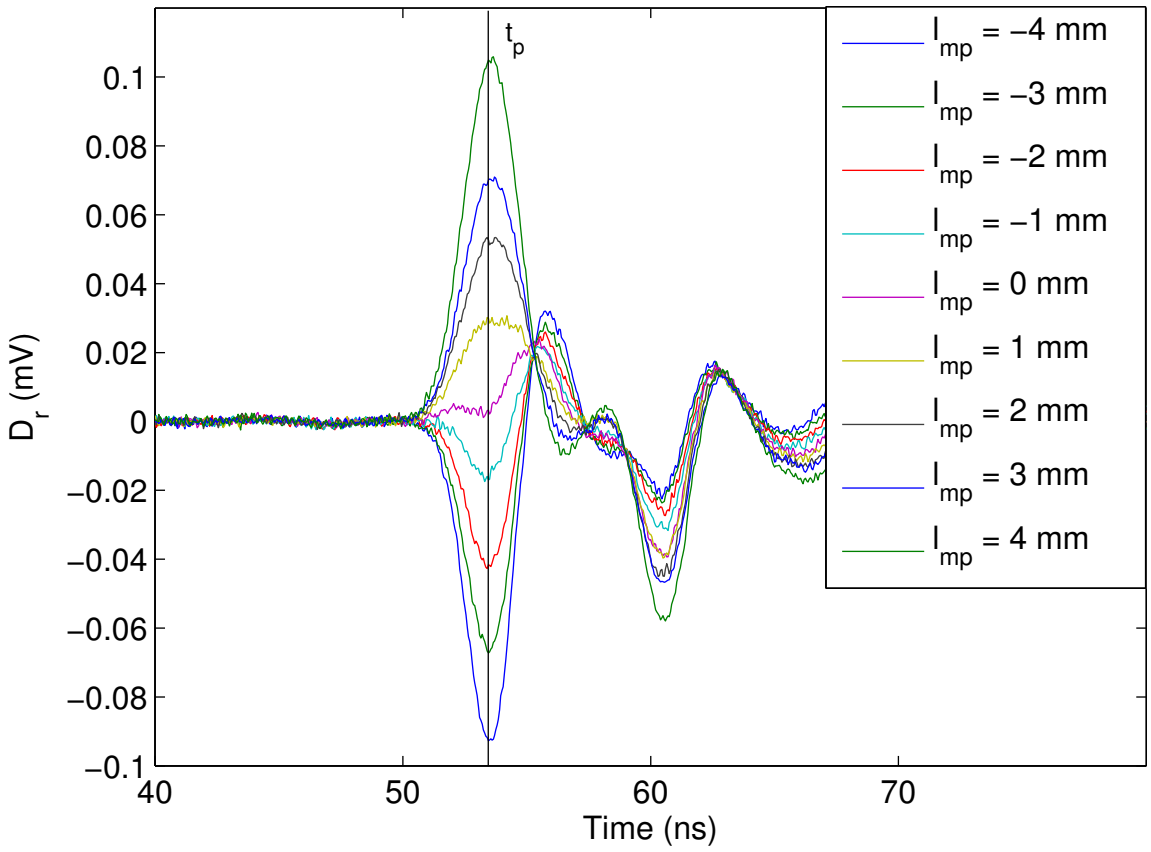

Figure 2.14: Difference residual vs. time for a range of l_{mp} between +4 and −4 mm.

phase shifters. At each step the LO was rephased using the large angle phase shifter so that the Σ_Q was zero and the measurement process was repeated (without the initial step to find t_p). This gave a set of difference residuals; an example is shown in Figure 2.14.

The difference residual at t_p vs. l_{mp} is shown in Figure 2.15; the variation is linear. If l_c was exactly the opposite of the internal path length difference in the processor the value of the D_r at $l_{mp} = 0$ would be zero. If, as is shown in Figure 2.15, this was not the case l_c was altered. For each processor a pair of cables was chosen to minimise D_r at $l_{mp} = 0$. For each pair of cables that were selected the final path difference is shown in Table 2.2.

2.6 Problems with Reducing the Path Difference

Correcting for imperfections inside the processor using external cables assumes these cables have a fixed length. This is not the case as the cables used are flexible. Bending them affects the dielectric path length by altering both the real length and putting the internal dielectric under pressure and changing its refractive index.

Each cable's dielectric path length was measured in November 2010 and again in March 2011.

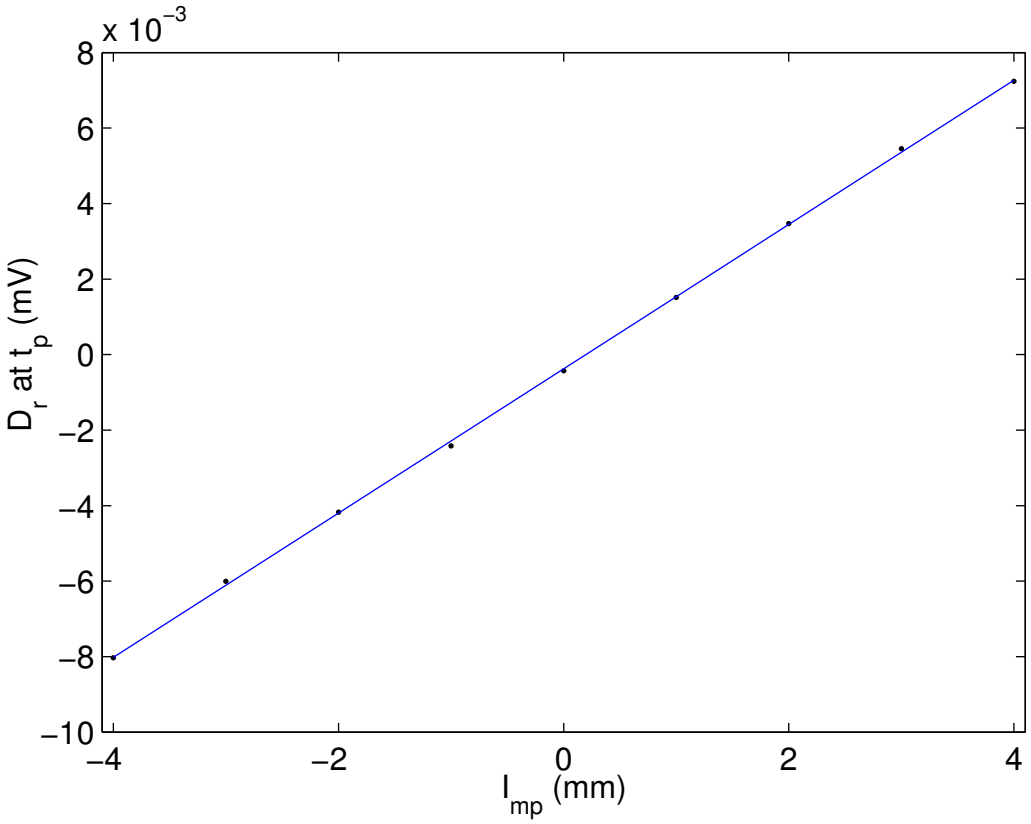

Figure 2.15: Difference residual at t_p vs. l_{mp}.

Processor	Path Difference (mm)
1	-0.14
2	-0.18
3	0.38
4	0.016
5	0.10
7	0.24
8	-0.23
10	-0.34

Table 2.2: Final path differences for the FONT BPM Processors.

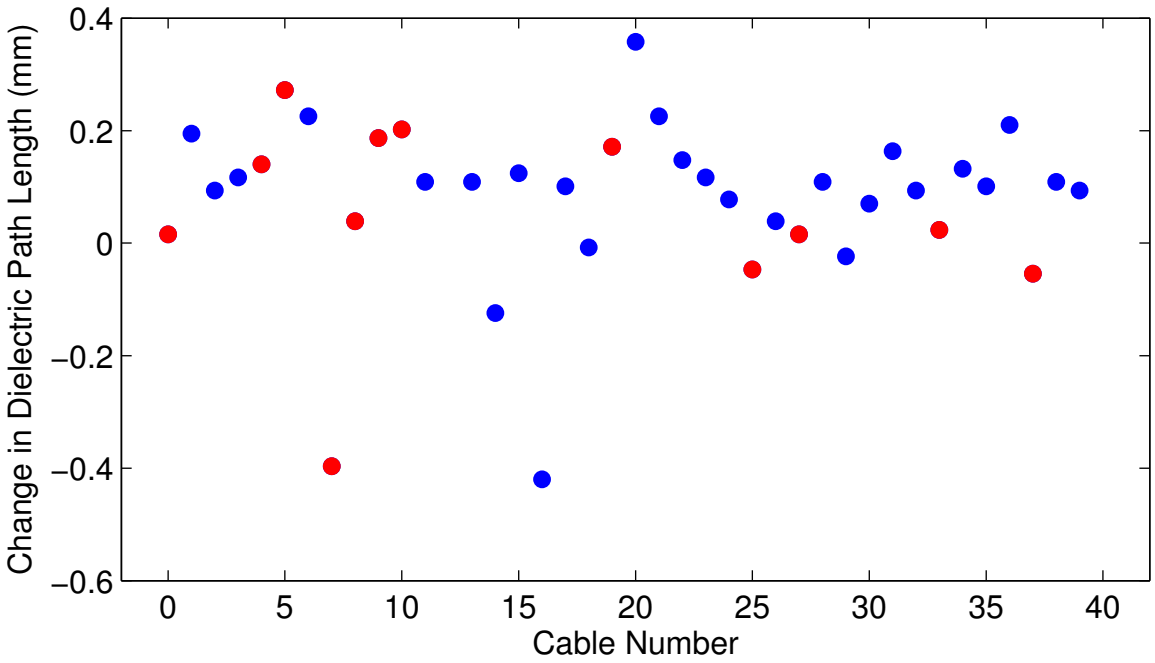

Figure 2.16: The change in dielectric path length of the external cables between two measurements made approximately four months apart vs. cable number for the cables that have not (blue) and have (red) been used in experiments at the ATF.

The difference between the two measurements is shown in Figure 2.16. The cables have been arbitrarily numbered from 0 to 39. As the FONT group took a trip to Japan in December 2010 some of the cables were used in the beamline at ATF. These were handled more frequently and roughly than most other cables in the set and are shown in red. The length difference for these cables does not appear to vary more than for the unused cables in the set.

The standard deviation is 0.15 mm; some cables differ from the mean by as much as 0.6 mm. Further tests showed that flexing the cables by hand could change their dielectric length by as much as 0.4 mm and that after flexing the cables would not always return to their nominal length.

In addition to such changes in the cable dielectric lengths, attenuators are regularly used at ATF and although notionally matched in length can also introduce path length differences. Differences in SMA connector tightness and inbuilt irregularities in the BPMs themselves further worsen the effects. The meant that the path length difference between the two BPM processor channels was much greater than the target 0.5 mm and hence it was concluded that although using cables to correct for the effect of the phase sensitivity in the lab worked well it was not optimal for use at the ATF. Despite this the matched cables were still used at the ATF.

2.7 Further Reductions of the Phase Sensitivity

Two further approaches were tried to reduce the sensitivity to LO phase: an offline analysis using the Σ_Q signal and an online method using remote control phase shifters (RCPS).

2.7.1 Offline Analysis

Σ_Q can be used to distinguish true position jitter from LO phase jitter. Equation 2.17 gives the affect of a LO phase jitter on the measured position; for small angles this effect will be approximately linear. Assume the measured position y_m is a combination of the actual position y_a and LO phase ϕ and write

$$y_m = y_a + b\phi \tag{2.19}$$

where b is a constant determining the amount of LO phase pollution in the measured position. A measure of ϕ can be gained using the Σ and Σ_Q signals: Consider first the output of the Σ channel after the down-mix

$$\Sigma = A_\Sigma A_{LO} sin(\omega_\Sigma t) \cdot sin(\omega_{LO} t) \tag{2.20}$$

where ω_I and ω_{LO} and A_I and A_{LO} are the angular frequencies and amplitudes of the Σ and LO signals respectively. Ignoring up-mixed components and setting $\omega_{LO} = \omega_\Sigma$ Equation 2.20 approximates to

$$\Sigma = \frac{A_\Sigma A_{LO}}{2} \cos(\phi) \tag{2.21}$$

The output of the Σ_Q channel after the down-mix will be

$$\Sigma_Q = A_\Sigma A_{LO} sin(\omega_\Sigma t) \cdot cos(\omega_{LO} t) \tag{2.22}$$

or

$$\Sigma_Q = \frac{A_\Sigma A_{LO}}{2} \sin(\phi) \tag{2.23}$$

therefore

$$\phi = \tan^{-1} \frac{\Sigma_Q}{\Sigma} \tag{2.24}$$

BPM	Without Offline Correction (μm/$^\circ$)	With Offline Correction (μm/$^\circ$)
P1	-7.63 $\pm$ 0.02	1.04 $\pm$ 0.02
P2	-2.78 $\pm$ 0.03	-0.40 $\pm$ 0.01
P3	-0.97 $\pm$ 0.02	-0.14 $\pm$ 0.01

Table 2.3: BPM phase sensitivity without and with offline LO phase correction. The errors represent the statistical uncertainty on the results.

The phase of the processor is purposely set so to minimise Σ_Q and maximise Σ and so for $\Sigma_Q/\Sigma << 1$:

$$\phi \approx \frac{\Sigma_Q}{\Sigma} \tag{2.25}$$

Rewriting Equation 2.19 in these terms and using

$$y_m = \frac{\Delta}{\Sigma} \tag{2.26}$$

gives an equation for the true position

$$y_a = \frac{\Delta - b\Sigma_Q}{\Sigma} \tag{2.27}$$

where b can be obtained via a fit of

$$y_m = \frac{b\Sigma_Q}{\Sigma} + \eta \tag{2.28}$$

to measured data where η is some arbitrary global LO phase which can be ignored. This method was employed offline to correct for LO phase jitter.

Figure 2.17 shows measured beam position vs. master LO phase setting during an LO phase scan without and with the offline correction. The position sensitivity to a variation in the LO phase is given in Table 2.3. The scan shows a reduction in the phase sensitivity when the offline correction is applied. There is still an offset from zero after the LO phase removal (especially visible in (b)), this is a result of a slight mis-phasing of the LO signal.

2.7.2 Use of Remote Control Phase Shifters (RCPS)

For real-time beam stabilisation, such methodology needs to be applied to the measurement of the position used in the feedback loop (Section 4.1.3). Work was begun in 2011 to implement LO phase compensation in firmware via the method described in Section 2.7.1. Such work [50] is ongoing.

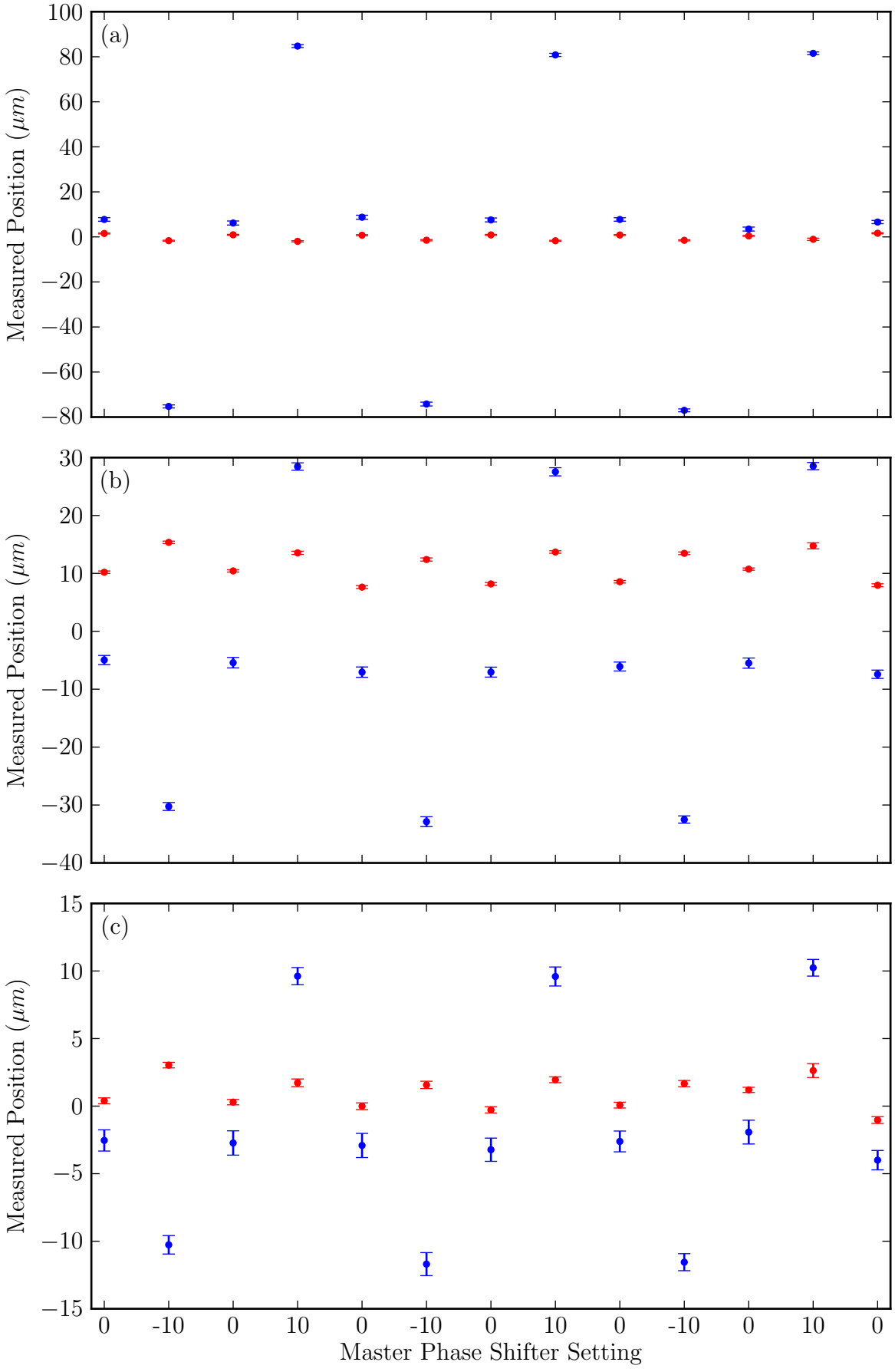

Figure 2.17: Measured position at (a) P1, (b) P2 and (c) P3 vs. master LO phase setting over a LO scan without (blue) and with (red) offline LO phase correction applied. The error bars represent the statistical uncertainty on each point.

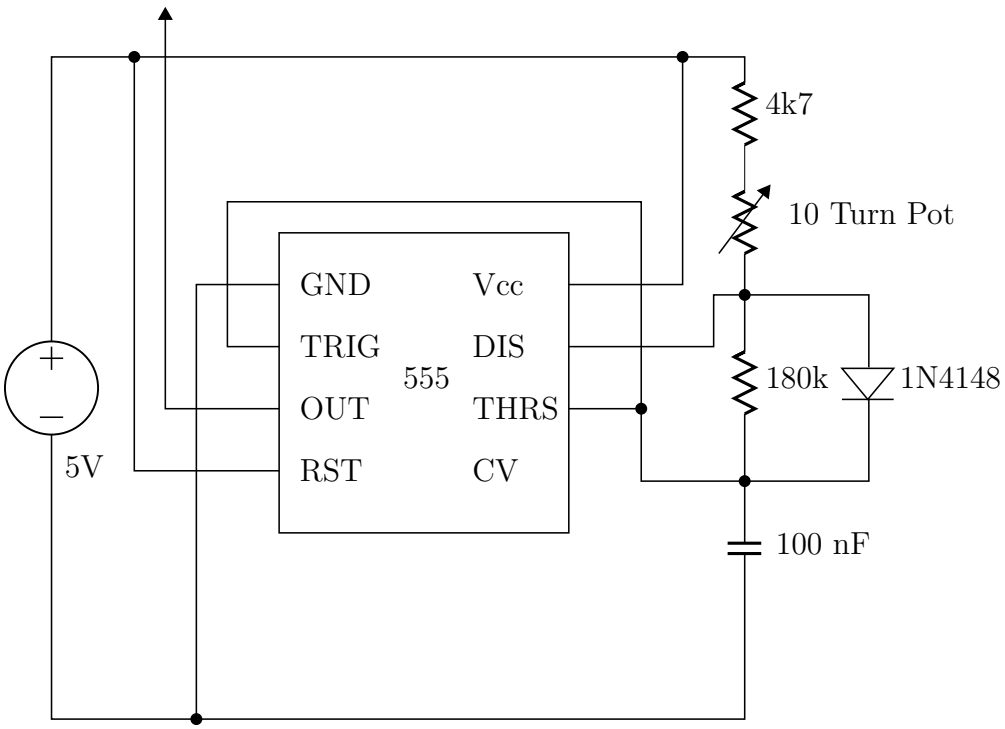

Figure 2.18: A circuit digram of the 555 circuit used to control the RCPS. The connection pins of the 555 chip are defined in Table 2.4.

Label	Pin
GND	Ground
TRIG	Trigger
OUT	Output
RST	Reset
Vcc	Positive supply voltage
DIS	Open collector output
THRS	Output ends when the voltage at THRS > CV
CV	Provides access to the internal voltage divider

Table 2.4: The output pins on the 555 chip.

A different online approach was devised using RCPS. The RCPS were built in Oxford by pairing mechanical phase shifters with electrical servos. One of these remote control phase shifters is shown in Figure 2.19. A control board (Figure 2.19) was built using the 555 timer circuit shown in Figure 2.18. The phase shifters were connected to this board via RG58 cables and set using a 10 turn pot which had settings between 0 and 1000. The system was calibrated so pot settings of 0 and 350 corresponded to the mechanical limit of the RCPS. Figure 2.21 shows the response of the RCPS over a range of pot settings.

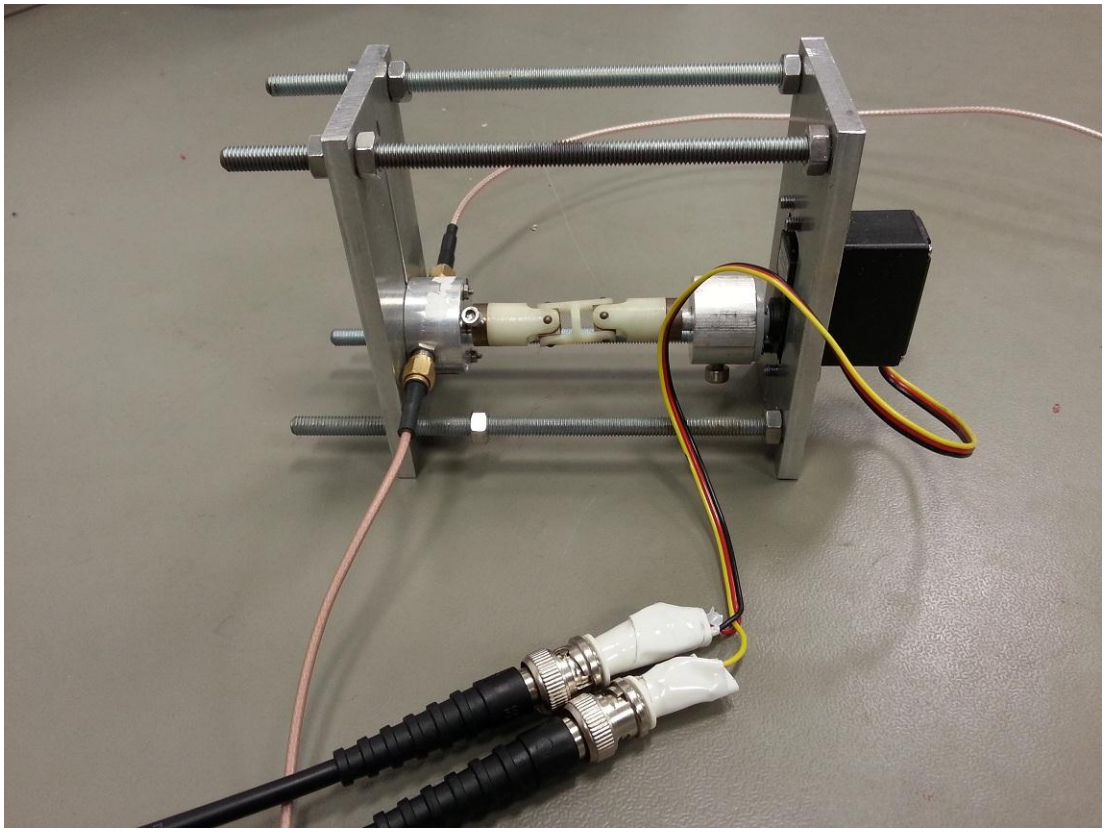

Figure 2.19: Photograph of a RCPS unit.

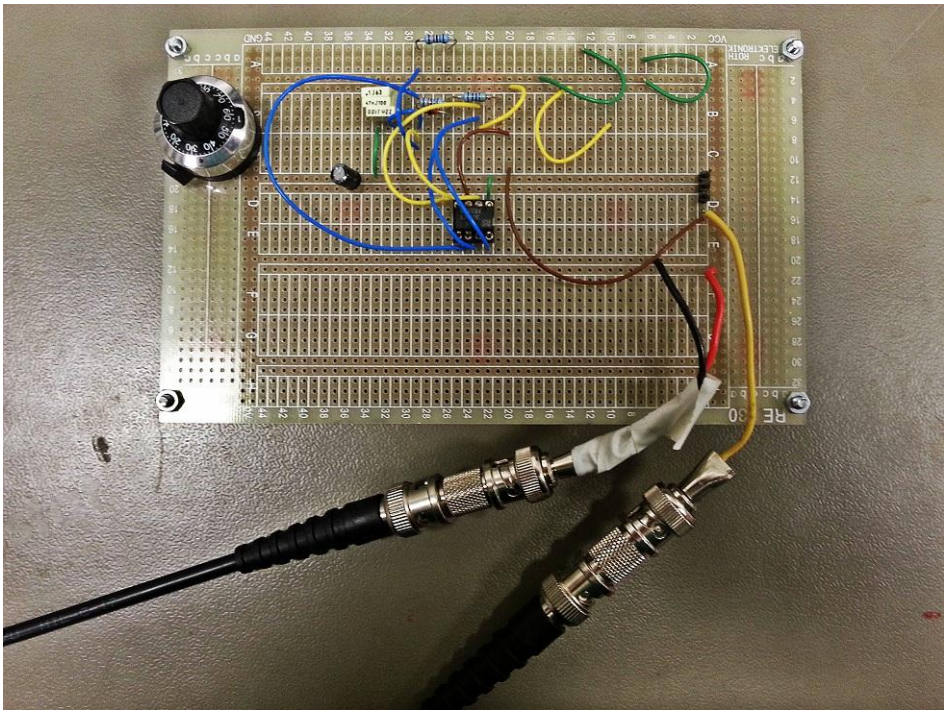

Figure 2.20: Photograph of the RCPS controller unit.

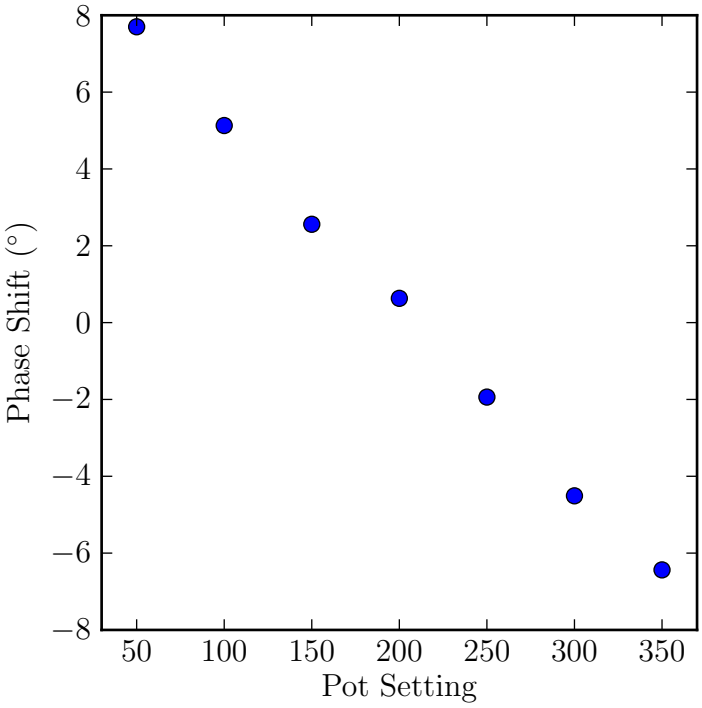

Figure 2.21: Phase shift vs. pot setting for a remote control phase shifter.

2.7.3 Setup of the RCPS

Three RCPS were constructed and built in Oxford before being transported to Japan. They were installed on the stripline BPMs P1, P2 and P3.

To set up the RCPS a test was devised based on the LO phase scan. The RCPS were set in a number of steps across their range and at each step a LO phase scan was undertaken (Figure 2.22). At each RCPS setting the phase sensitivity of the BPM processor was calculated from a fit of the measured position to LO phase angle which was calculated using Σ_Q/Σ. The phase sensitivity vs. RCPS setting was calculated (Table 2.5); this was plotted (Figure 2.23); a fit was used to find the RCPS setting which minimised the LO phase sensitivity and the RCPS shifter was set to this value to minimise the LO phase sensitivity. The phase sensitivity for an input cable length mismatch corresponding to 1° is given in Table 2.6.

2.8 BPM Resolution Measurements

2.8.1 BPM Setup

The BPMs were connected to the FONT5 board in the manner described in Section 1.6.3. At the start off each shift the processors were phased using the method described in Sec-

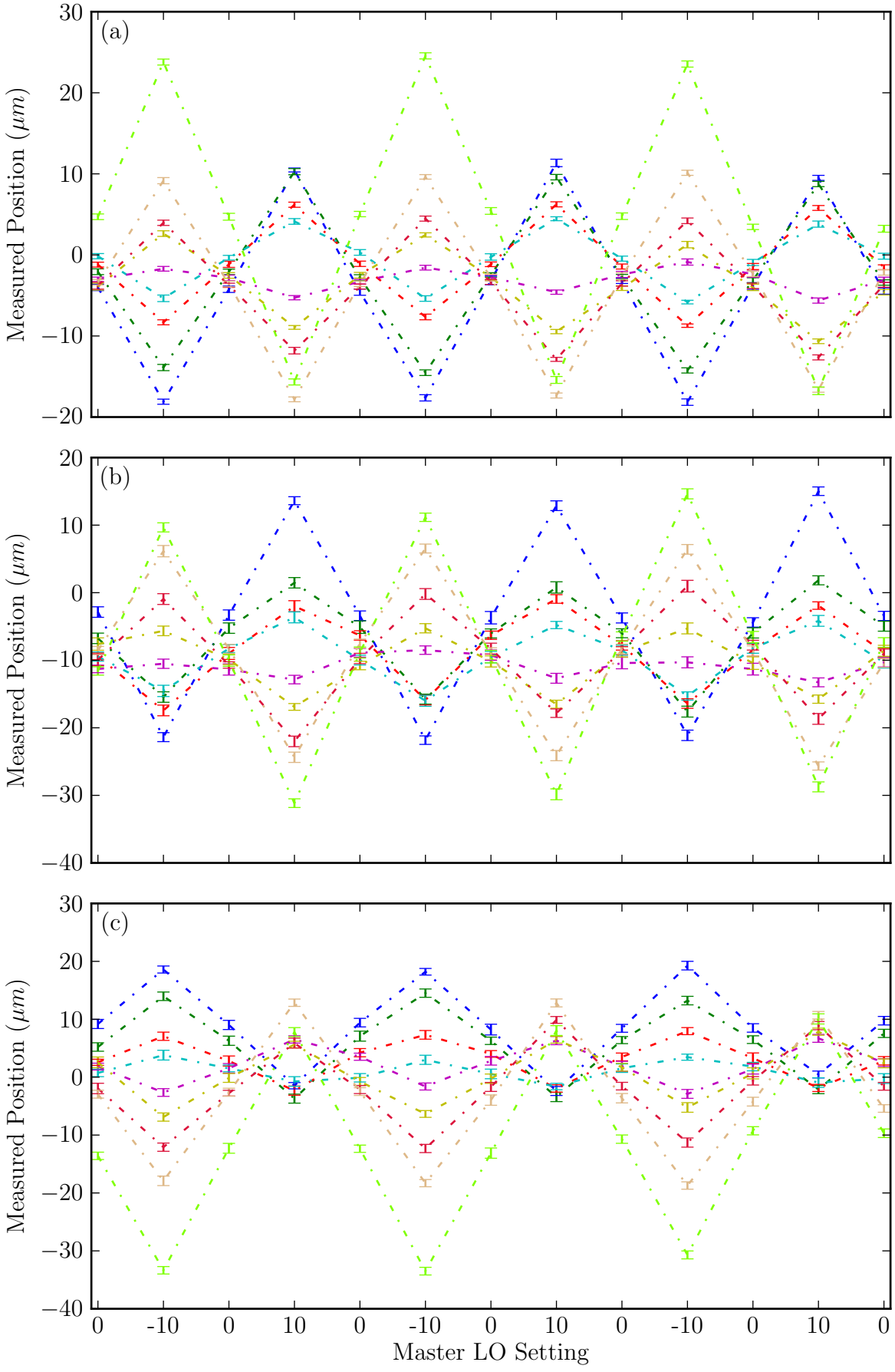

Figure 2.22: The apparent position vs. master LO phase setting for (a) P1, (b) P2 and (c) P3 at a number of RCPS settings either side of optimum ranging from a pot setting of -40 (green) to 40 (blue) in steps of 10 for a RCPS scan. The dotted lines are included to guide the eye. The error bars represent the statistical uncertainty on each point.

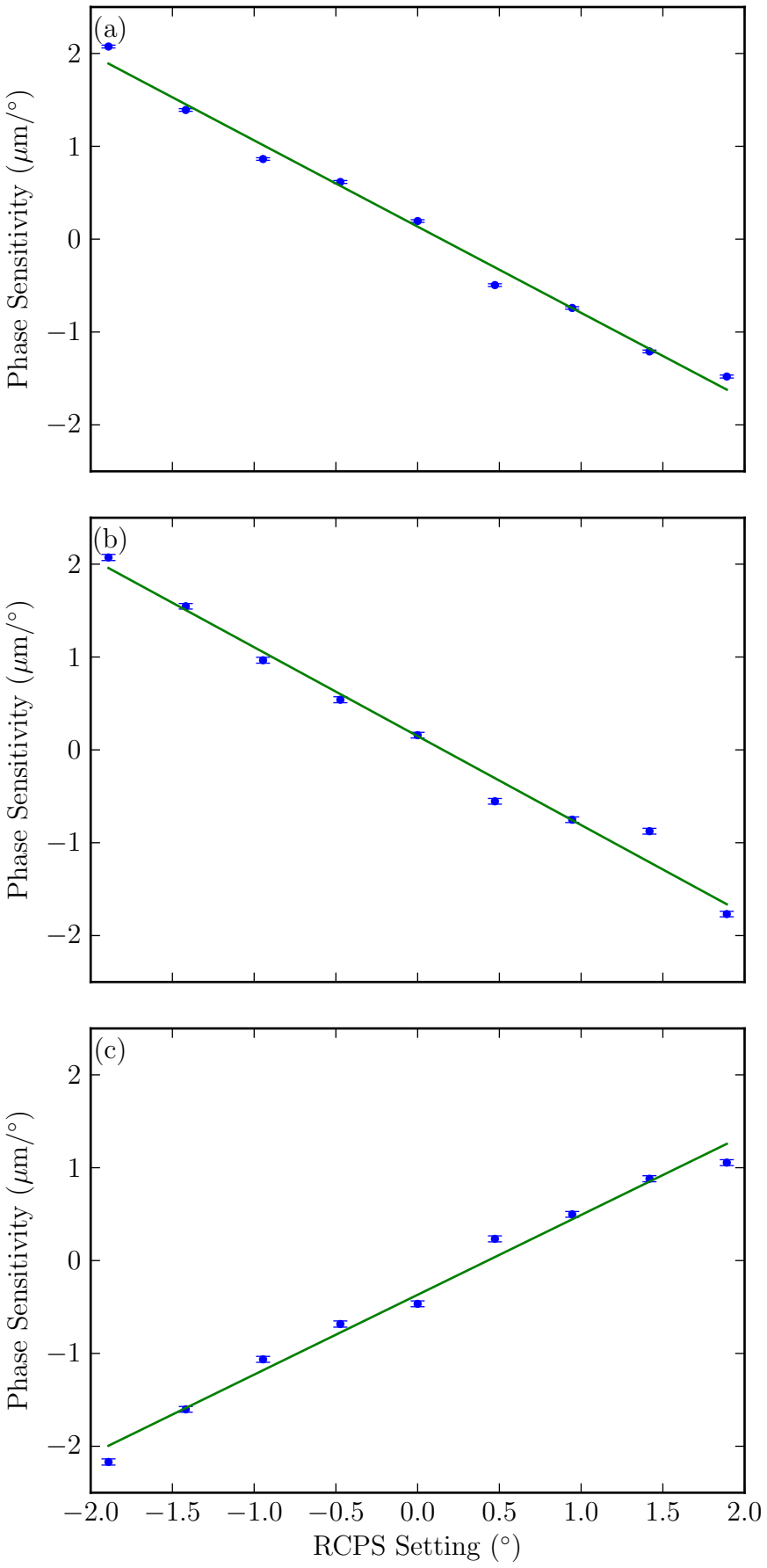

Figure 2.23: The LO Phase sensitivity (blue) vs. RCPS setting of (a) P1, (b) P2 and (c) P3 for a RCPS scan. The green lines represent linear fits applied to the data. The error bars represent the statistical uncertainty on each point.

RCPS Setting (°)	P1 Sens. (μm/°)	P2 Sens. (μm/°)	P3 Sens. (μm/°)
-1.9	2.05 ± 0.02	2.05 ± 0.04	-2.15 ± 0.03
-1.4	1.38 ± 0.02	1.53 ± 0.03	-1.58 ± 0.03
-0.9	0.85 ± 0.02	0.98 ± 0.03	-1.03 ± 0.03
-0.5	0.45 ± 0.02	0.52 ± 0.03	-0.69 ± 0.03
0.0	0.20 ± 0.01	0.14 ± 0.03	-0.48 ± 0.03
0.5	-0.50 ± 0.02	-0.54 ± 0.03	0.25 ± 0.04
0.9	-0.74 ± 0.01	-0.74 ± 0.03	0.50 ± 0.03
1.4	-1.19 ± 0.02	-0.87 ± 0.03	0.87 ± 0.03
1.9	-1.47 ± 0.02	-1.76 ± 0.03	1.04 ± 0.04

Table 2.5: Phase sensitivity vs. RCPS setting (°). The errors represent the statistical uncertainty from each fit.

BPM	Phase Sensitivity (μm/°)
P1	-0.92 ± 0.04
P2	-0.95 ± 0.06
P3	0.85 ± 0.05

Table 2.6: Phase sensitivity introduced by one degree of mismatch between the two input channels of each BPM. The errors represent the statistical uncertainty on the results.

tion 2.3.3. When installed the RCPS were set up and adjusted to minimise the BPMs LO phase sensitivity; the BPMs were then calibrated by moving them a known amount using the FONT movers and recording a data run at each (Figure 2.24). From the fit applied to the data κ from Equation 2.11 can then be calculated (Table 2.7). Further details of the setup procedure are given in [50].

2.8.2 Methods of Calculating the BPM Resolution

There are several methods for calculating the BPM resolution. If it is assumed that all BPMs have the same resolution then a minimum of three BPMs are required to form a set of simultaneous position measurements from which the average resolution of the BPMs can be calculated. For linear optics the position of the beam in any of the BPMs can be predicted by some linear combination of the position of the beam at the other two BPMs.

Writing then

$$T_1 y_{P1} + T_2 y_{P2} + T_3 y_{P3} = 0 \tag{2.29}$$

BPM	κ (μm/(Δ/Σ))
P1	389 ± 3
P2	421 ± 4
P3	393 ± 3

Table 2.7: κ for each BPM. The errors represents the statistical uncertainty on the results.

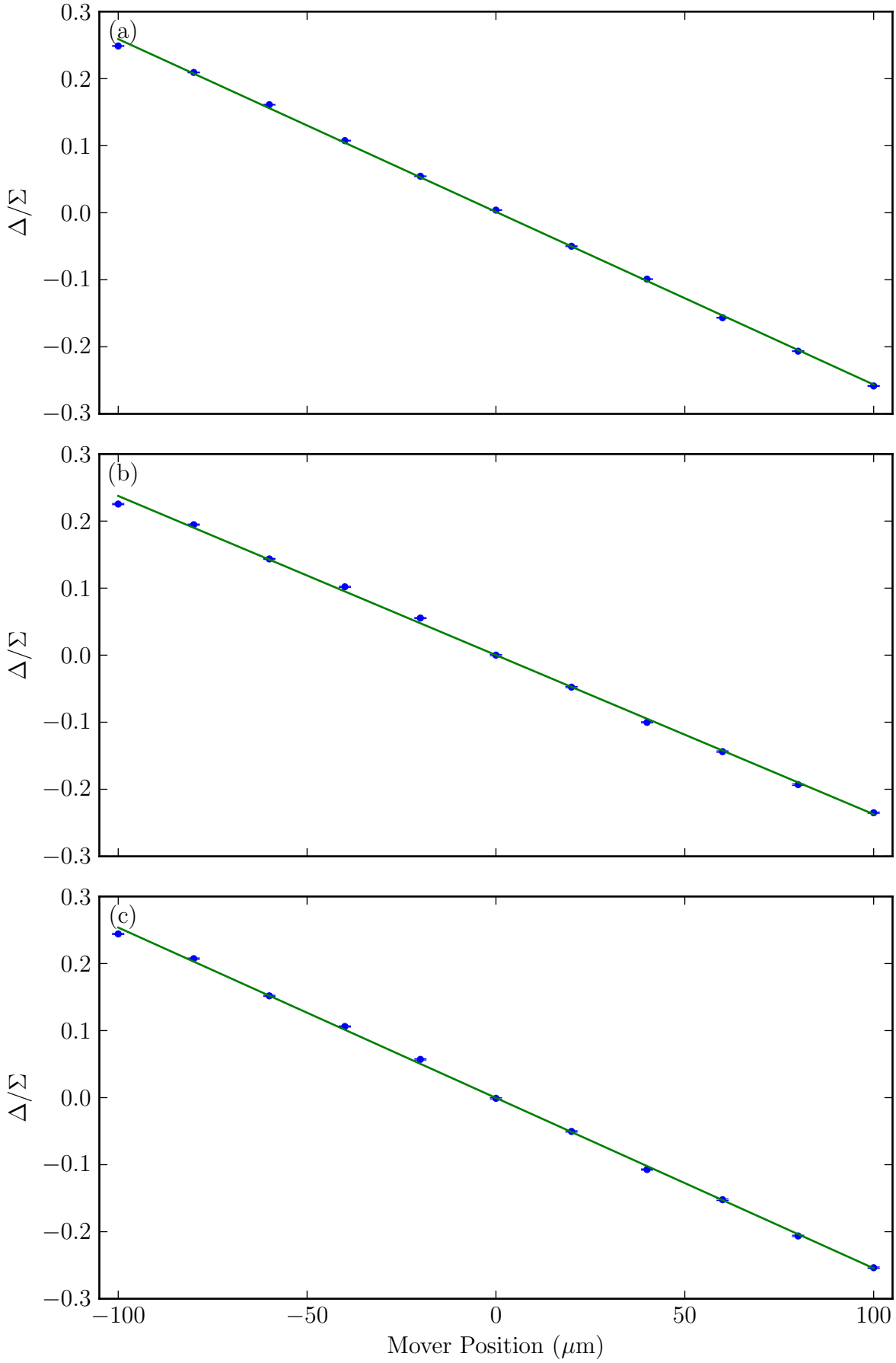

Figure 2.24: Raw position (blue) vs. BPM mover position for (a) P1, (b) P2 and (c) P3 for a BPM calibration. The green lines represent linear fits applied to the data. The error bars represent the statistical uncertainty on each point.

Where y_i (i = P1, P2, P3) is the vertical beam position at BPM i and T_i is a constant determined either directly from the linear transfer matrices or from fitting; this will be discussed later.

The measured position y^m is a convolution of the true position y and noise described by a random variable n_i normally distributed with a standard deviation equal to that of the i^{th} BPM's resolution σ_i

$$y^m = y + n_i \tag{2.30}$$

For BPM i the difference between the measured position and the position predicted by the other two BPMs δ_i is given by

$$\begin{aligned} \delta_i &= y_i^m - \tfrac{T_j y_j^m + T_k y_k^m}{T_i} \\ &= \left(y_i - \tfrac{T_j y_j + T_k y_k}{T_i}\right) + \left(n_i + \tfrac{T_j n_j + T_k n_k}{T_i}\right) \end{aligned} \tag{2.31}$$

From Equation 2.29 the first term is zero. Considering the variance of the system and re-writing Equation 2.31 in terms of the resolution of BPM i, σ_i, gives

$$\mathrm{Var}\left(\delta_i\right) = \sigma_i^2 + \frac{T_j \sigma_j^2 + T_k \sigma_k^2}{T_i} \tag{2.32}$$

Equation 2.32 and its cyclic permutations become

$$\sum_{a=i,j,k} \frac{T_a}{T_i} \cdot \sigma_a^2 = \mathrm{Var}\left(\delta_i\right) \tag{2.33}$$

With three independent resolutions and a rank 2 matrix no unique solution to Equation 2.33 exists. However assuming the resolution of all three BPMs is the same a unique solution can be obtained and an estimate of this resolution calculated. This is given by

$$\sigma_i = \sqrt{\frac{\mathrm{Var}\left(\delta_i\right)}{1 + \frac{T_j}{T_i} + \frac{T_k}{T_i}}} \tag{2.34}$$

where the three cyclic permutations each give an estimate of the average resolution.

There are two methods for obtaining the constants $T_{i,j,k}$: 1) Geometric calculation using the lattice model. The constants $T_{i,j,k}$ can be calculated directly from the linear transfer matrices between the BPMs P1, P2 and P3. These transfer matrices can be obtained using one of several ATF lattice models. Here the 'Flight Simulator' has been used [57]. 2) Fitting to the data. Considering a long data run of many independent triggers a least squared fit of

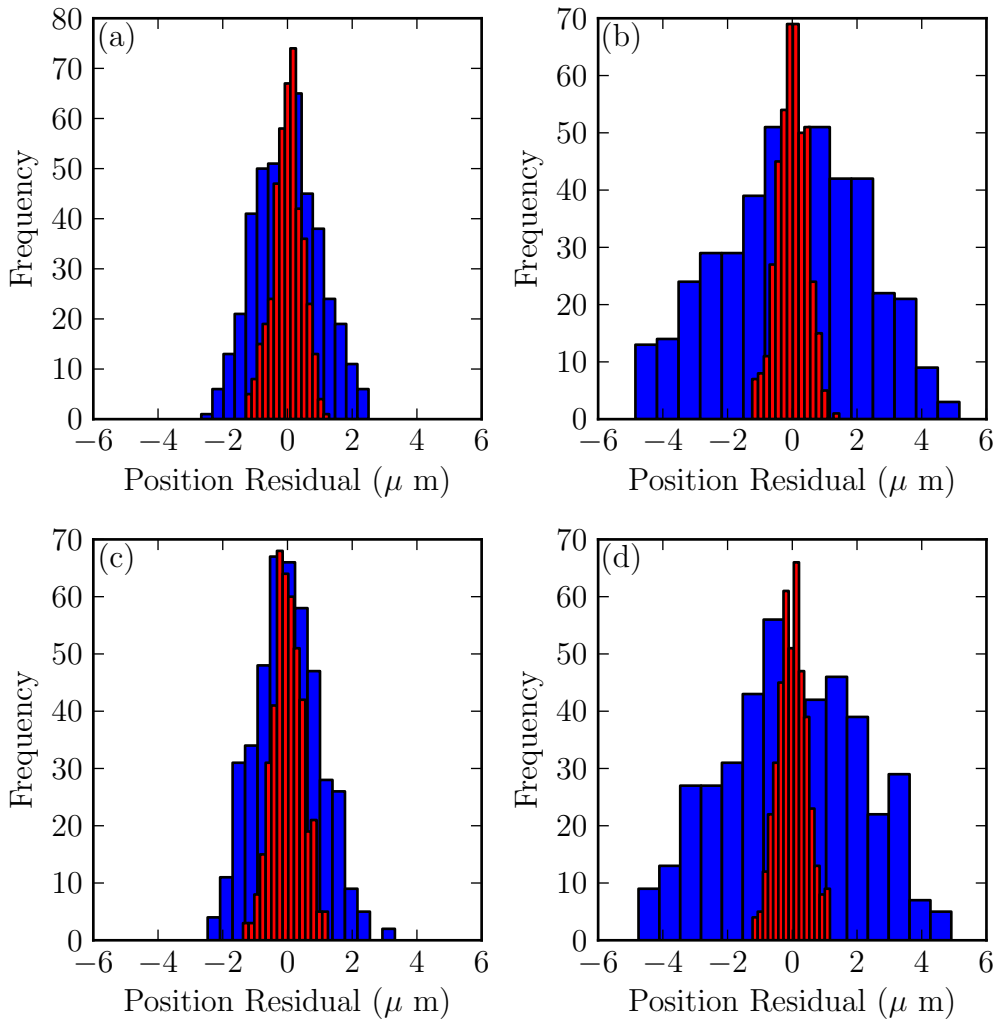

Figure 2.25: The difference between the predicted and measured positions for the first bunch (a) fitted method and (b) geometric method; second bunch (c) fitted method and (d) geometric method without (blue) and with (red) offline phase correction.

Equation 2.29 can be applied to the data to yield $T_{i,j,k}$. Results will be presented for both methods.

2.8.3 Results

Figure 2.25 shows the distributions of the difference between the predicted and measured positions; from the RMS width of these distributions the resolution can be calculated. Two sets of distributions are presented, one using the geometric relation constants and one using the fitted relation constants. In each case the results are shown both without and with offline LO phase correction. For these tests the ATF was run in two bunch mode; results are presented for bunches one and two.

The results demonstrate a reduction in the RMS width of the distribution when offline LO

	Bunch 1 σ_y (μm)	Bunch 2 σ_y (μm)
Fitted Without Correction	1.00 ± 0.04	1.00 ± 0.01
Fitted With Correction	0.33 ± 0.01	0.33 ± 0.01
Geometric Without Correction	2.28 ± 0.08	2.20 ± 0.08
Geometric With Correction	0.34 ± 0.01	0.33 ± 0.01

Table 2.8: BPM resolution without and with offline phase correction. The errors represent the statistical uncertainty.

	Bunch 1 σ_y (μm)	Bunch 2 σ_y (μm)
Fitted Without Correction	1.00 ± 0.04	1.00 ± 0.01
Fitted With RCPS	0.33 ± 0.01	0.35 ± 0.01
Geometric Without Correction	2.28 ± 0.08	2.20 ± 0.08
Geometric With RCPS	0.42 ± 0.01	0.40 ± 0.01

Table 2.9: BPM resolution without and with RCPS. The errors represent the statistical uncertainty.

phase correction is applied. Both sets of results give estimates of the average BPM resolution from the standard distributions of the residuals. The resolutions of the BPMs without and with offline LO phase correction are shown in Table 2.8. They demonstrate an improvement in the resolution when offline phase correction is applied. The two methods of calculating the resolution show good agreement after the correction is applied.

The best resolution of a BPM can be calculated using the ADC noise for a given run [49]. In this case the theoretical resolution was 0.25 μm; 0.33 μm is close to this limit and represents a notable achievement for the resolution of stripline BPMs.

Results are also shown to illustrate the effectiveness of RCPS. Long data sets have been taken using the upstream BPMs without and with RCPS. The RMS distributions of the difference between the predicted and measured positions are shown in Figure 2.26. Table 2.9 gives the BPM resolutions calculated from these distributions.

The results show a clear improvement in the resolution when the RCPS are used with the geometric method giving a slightly poorer resolution than the fitted method. Comparing these results with those presented offline corrections the fitted method agrees within the error of the results.

The effect of the phase correction was further studied by setting the RCPSs to a range of values either side of their optima and recording a resolution run at each (Figure 2.27); the resolution at each setting is given in Table 2.10. The results show the behaviour expected with a degradation of resolution as the RCPS are increasingly mis-set. The geometric method suffers a greater degradation of resolution then the fitted method, this is because the calibration constant changes slightly as the RCPS is mis-set. This is accounted for in the fitted method as the calibration constant is inherently included in the fit but not in the geometric method where it is not. The minimum resolution in this scan is greater than that presented in previous results, this is because the bunch charge was lower when this data was taken.

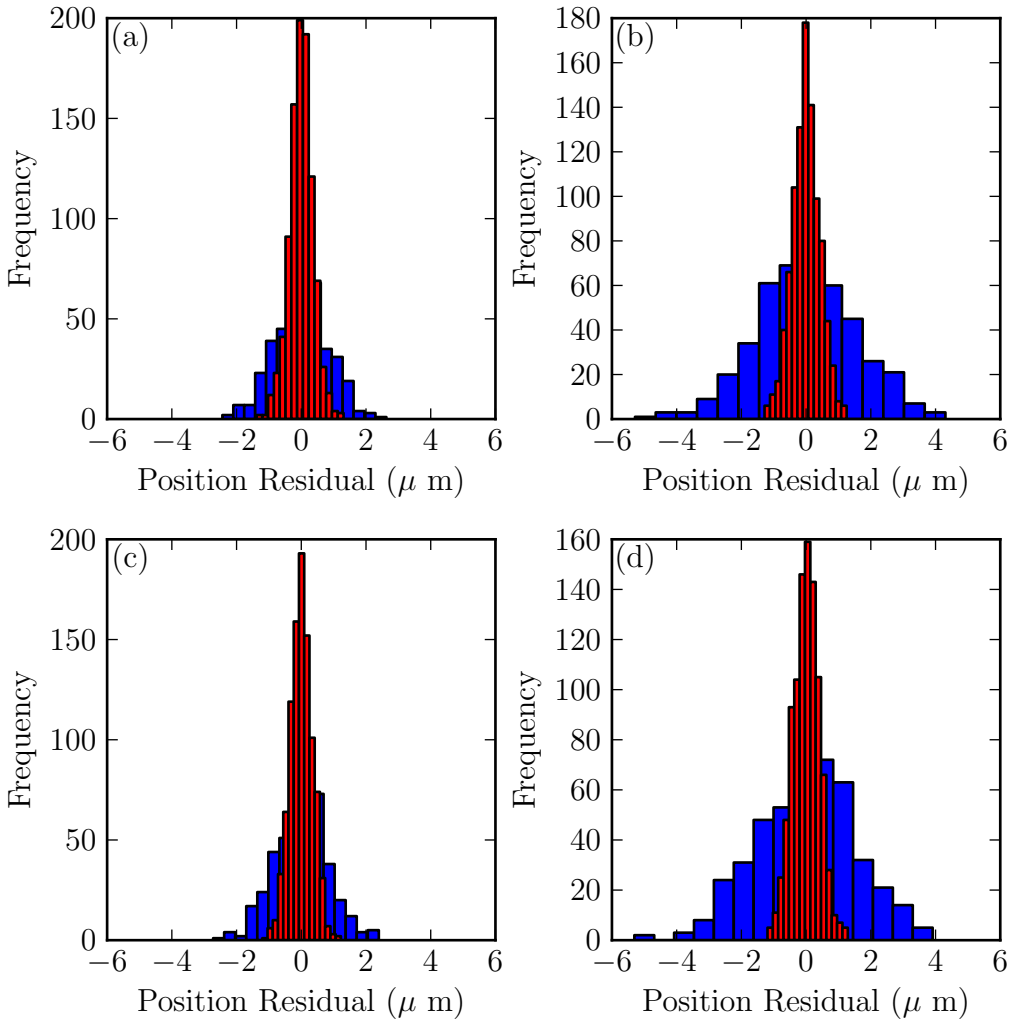

Figure 2.26: The difference between the predicted and measured positions for the first bunch (a) fitted method and (b) geometric method; second bunch (c) fitted method and (d) geometric method without (blue) and with (red) RCPS.

RCPS Setting (°)	Geo. σ_y (μm)	Fitted σ_y (μm)
-6.6	1.77 ± 0.08	0.55 ± 0.03
-3.3	0.87 ± 0.04	0.48 ± 0.02
0	0.48 ± 0.02	0.47 ± 0.02
3.3	0.92 ± 0.04	0.51 ± 0.02
6.6	1.37 ± 0.06	0.69 ± 0.03

Table 2.10: First bunch resolution vs. RCPS setting calculated using the geometric and fitted method. The errors represent the statistical uncertainty.

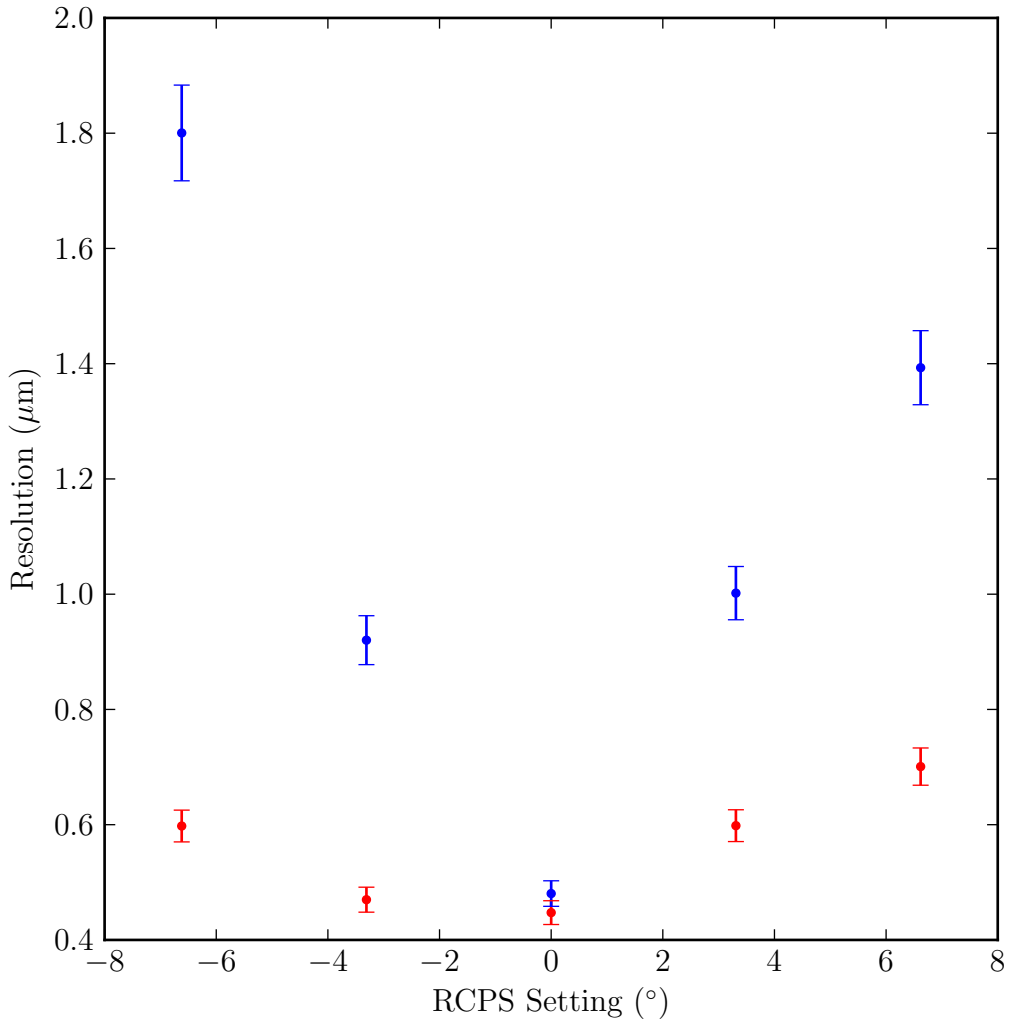

Figure 2.27: BPM resolution vs. RCPS setting calculated using the geometric (blue) and fitted (red) method. The error bars represent the statistical uncertainty on each point.

2.9 Summary

Experiments done at the ATF and in the lab yielded strong suggestions that the dominating factor in the position resolution was a sensitivity to LO phase jitter. Three methods of reducing the BPM processor sensitivity to LO phase jitter were tested. The first method attempted to use external cables to correct internal imperfections in the BPM processor that make it sensitive to LO phase jitter; the second method used an offline analysis technique to remove the component of LO phase jitter from the measured position; and the final method used remote control phase shifters to correct internal imperfections in the BPM processor.

Measurements taken with both offline LO phase correction and using RCPS demonstrated position resolutions of approximately 0.35 μm. The resolution limit predicted by the ADC noise level was 0.25 μm. The resolution requirement of the BPMs for the ILC feedback system is approximately 1 mum.

Chapter 3

The ATF IP Cavity BPMs

3.1 Cavity BPMs

Figure 3.1 shows a cavity BPM, a hollow metallic resonator installed in a beam-line. A bunch travelling through the cavity excites electrical oscillations, from these oscillations a measurement of the beam position can be gained. This chapter explains the basic theory of cavity BPMs and how they can be used to measure the beam position. The cavity BPMs and signal processing electronics at the ATF are described along with the setup and calibration procedures. Finally, the resolution of the BPMs is discussed and various techniques used to improve the resolution are presented.

3.1.1 The Theory of Cavity BPMs

A cavity BPM acts as a resonator in the beam-line. When a relativistic bunch travels through the cavity it will excite electromagnetic oscillations, these are characterised by the eigenmodes of the electromagnetic fields within the cavity. Two types of field patterns are possible in the cavity, transverse magnetic (TM) and transverse electric (TE). These eigenmodes are functions of the geometry of the cavity and as such the cavity can be designed to give it specific characteristics for use as a BPM.

The TM and TE eigenmodes of a cavity can be represented in terms of a coordinate system (x, y, z). The electromagnetic fields are given in [58] and for the TM modes are represented in terms of integers (m, n, l) which specify the modes numbers in the (x, y, z) directions. In beam position monitoring three modes are used: the TM_{010} (first monopole mode) in a circular monopole cavity and the TM_{210} and TM_{120} (first dipole modes) in a rectangular cavity.

Each of these modes is characterised by an angular frequency ω and a decay time τ. Sig-

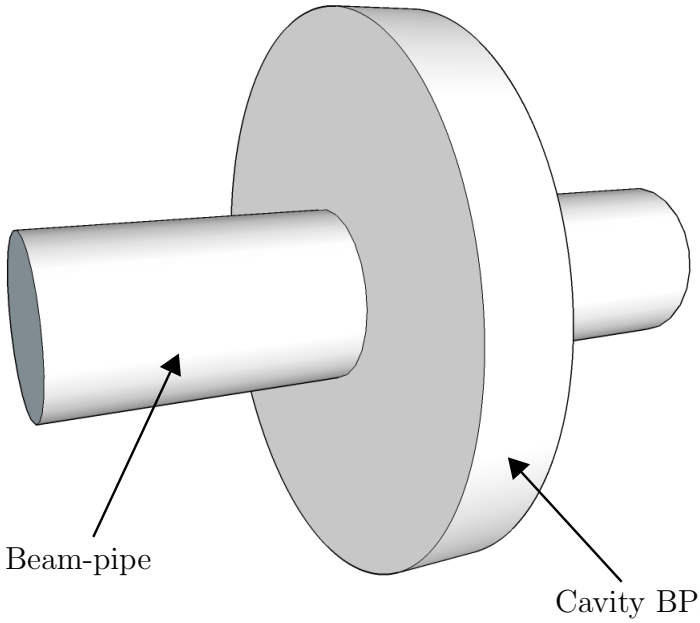

Figure 3.1: A diagram of a cavity BPM installed in a beamline.

nals excited in the cavity will oscillate at the angular frequency and decrease in amplitude exponentially, characterised by the decay time.

3.1.1.1 The First Monopole Mode

The first monopole or TM_{010} mode is normally used as the accelerating mode in an RF cavity. A diagram of the TM_{010} mode in a cavity is shown in Figure 3.2. When a beam passes through a cavity the beam charge couples linearly to the TM_{010} mode with no coupling to the beam position. As such the TM_{010} mode can be used to construct a reference cavity whose output is dependent only on beam charge.

3.1.1.2 The Dipole Mode

In a rectangular dipole cavity the first dipole modes (TM_{210} and TM_{120}), shown in Figure 3.3, are used to measure beam position in the x and y axis respectively. The oscillation of these modes is directly proportional to the beam offset from the cavity's electrical centre: a beam passing through with no displacement will not excite an oscillation and the oscillations will grow with the beam's displacement. This can be used to construct a cavity whose response to beam offset is linear, which can be used measure beam position.

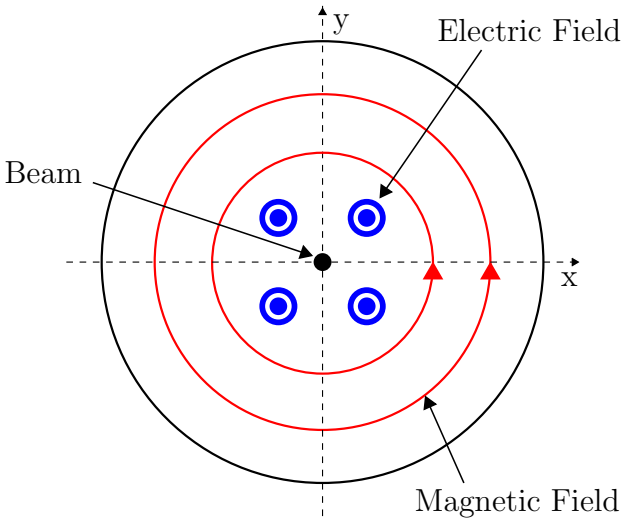

Figure 3.2: The first monopole mode of a cavity BPM.

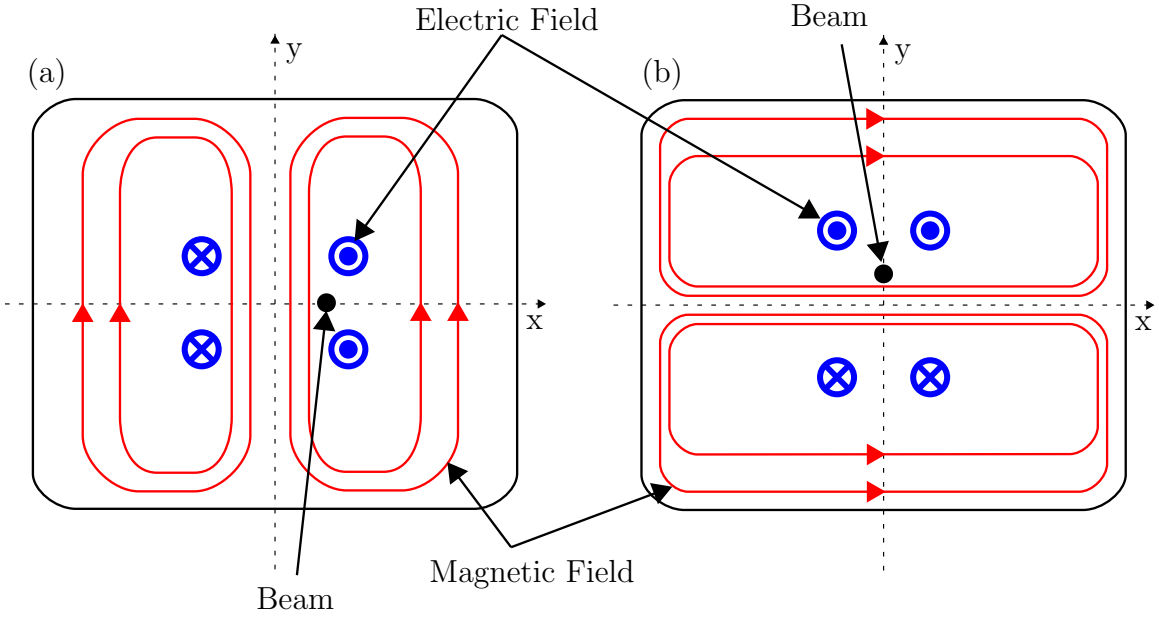

Figure 3.3: The (a) TM_{210} and (b) TM_{120} modes of a rectangular dipole cavity.

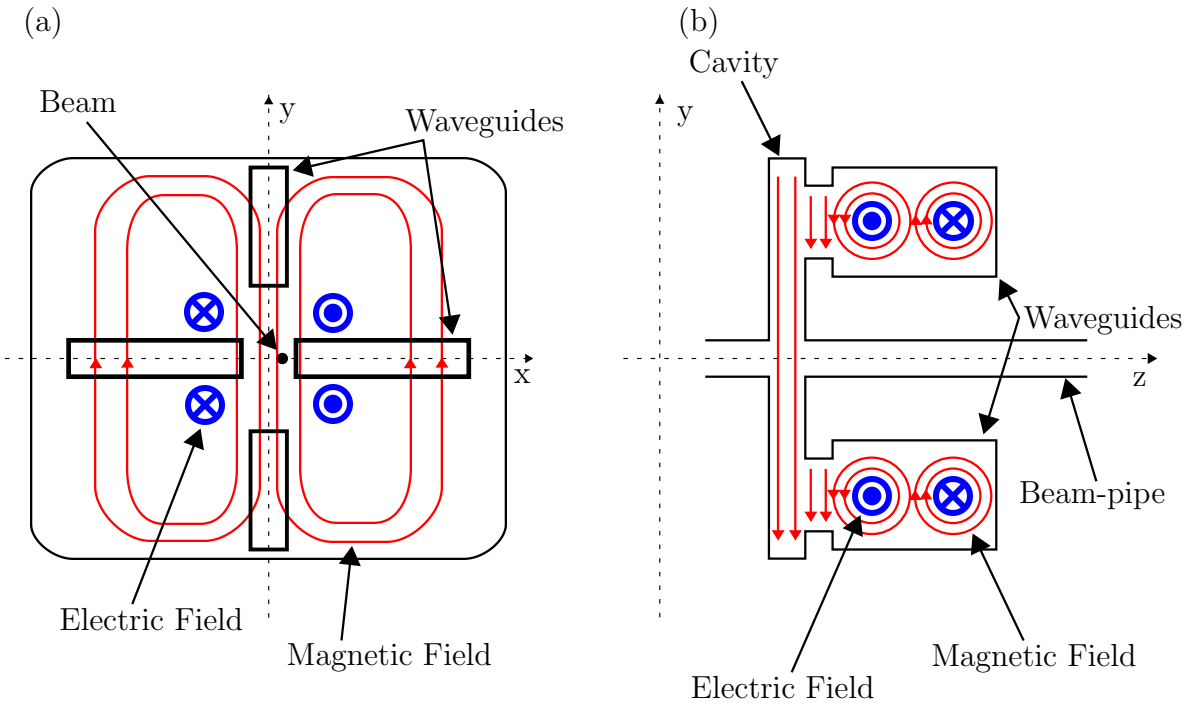

Figure 3.4: A rectangular cavity BPM with the TM_{210} mode excited shown (a) face-on and (b) side-on; the waveguides used to couple out the cavity signals are also shown.

3.1.1.3 Cavity Signal Extraction

To measure the beam position the signals from the cavity BPM must be read out and recorded. It is important that only the mode of interest is read out, be that the monopole mode for a reference cavity or the dipole mode for a position cavity. In a dipole cavity the main monopole mode will typically be strongly present as well as other higher order modes and these should be suppressed. Poor suppression of the unwanted modes can cause position offsets and non linearities affecting the position resolution of the BPM.

For dipole cavities waveguides are used to extract the position signal, and their designs can be constrained to suppress unwanted frequencies whilst strongly coupling to the desired signals. The waveguide is designed such that its cut-off frequency is just below the dipole mode of the cavity; the lower frequency main monopole mode will therefore be strongly suppressed.

To be coupled out the magnetic field of the signal must be directed along the length of the waveguide. Four waveguides on each cavity are used to deconvolve the horizontal and vertical position signals, two in each axis. Figure 3.4 shows the dipole mode excited when a bunch passes through a cavity off centre in the x axis. The magnetic field is directed radially along the waveguide orientated along the y axis and so will be coupled out. Along the x axis the magnetic field passes circumferentially across the slot and so will be suppressed.

The coupled out magnetic field excites an electric field in the waveguide. Coaxial antennas attached to the waveguides read out this electric field. They are positioned at anti-nodes of the field such that the opposite waveguides in each axis are π out of phase with one another. The signals from each pair of waveguides are then combined using a 180° hybrid. This acts

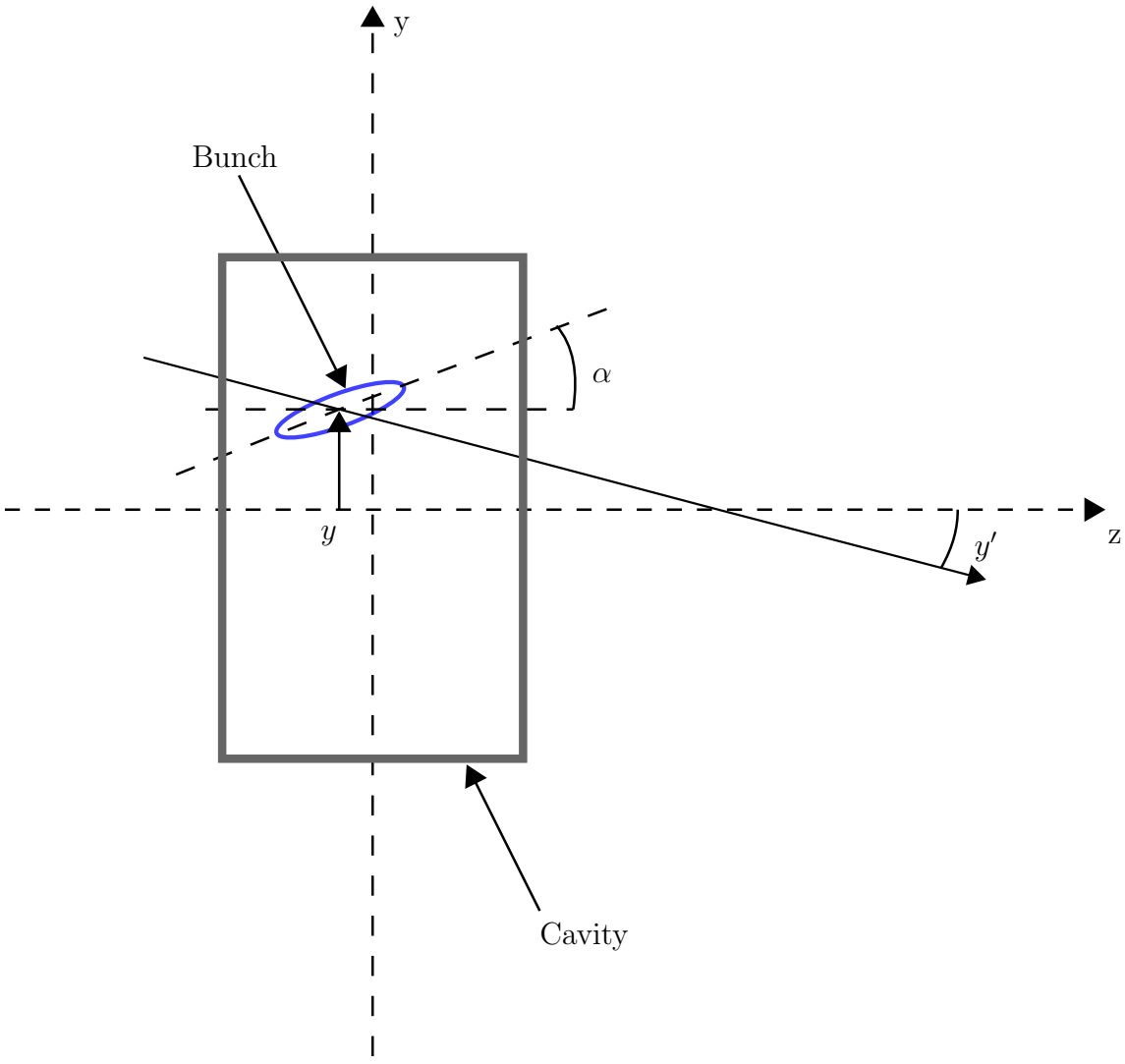

Figure 3.5: A bunch with a vertical displacement y; travelling at a bunch angle y' and with a bunch tilt α passing through a rectangular dipole cavity.

to further suppress the main monopole mode.

3.1.2 Output Signal from a Cavity

Figure 3.5 shows a bunch of charge q; with a vertical displacement y; travelling at an angle y' and with a bunch tilt α with respect to horizontal passing through a dipole cavity of angular frequency ω_d and decay time τ. The output signals from a cavity pickoff in such a scenario are given by [59]

$$V_y(y, q, t) \propto yqe^{-t/2\tau} \sin(\omega_d t) \tag{3.1}$$

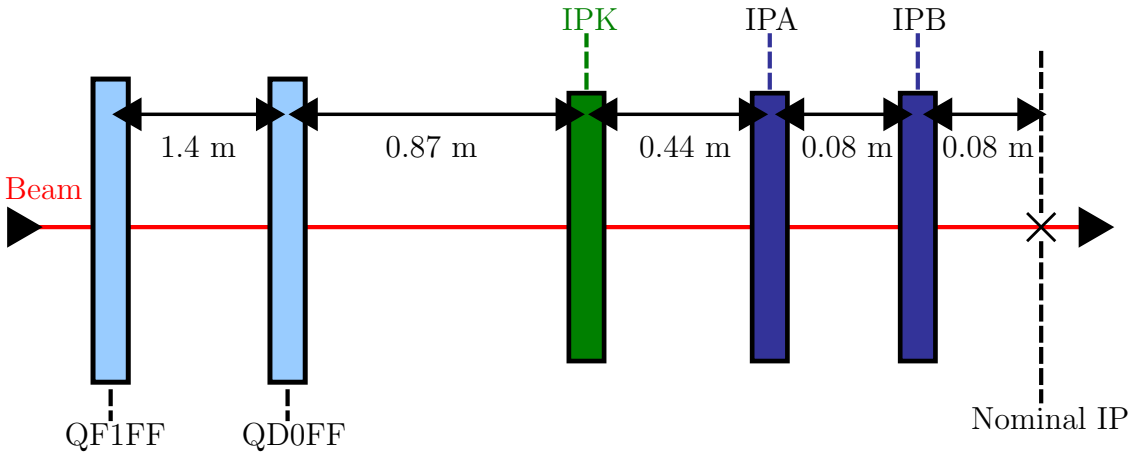

Figure 3.6: A schematic of the IP region showing the two final focus magnets QF1FF and QD0FF; the IPK and the two IP BPMs IPA and IPB.

$$V_{y'}(y', q, t) \propto -y' q e^{-t/2\tau} \cos(\omega_d t) \tag{3.2}$$

$$V_{\alpha}(\alpha, q, t) \propto \alpha q e^{-t/2\tau} \cos(\omega_d t) \tag{3.3}$$

in the limit α, $y' << 1$. The total output signal of the cavity (V_d) is given by

$$V_d(y, y', \alpha, q, t) \propto V_y(y, q, t) + V_{y'}(y', q, t) + V_{\alpha}(\alpha, q, t) \tag{3.4}$$

The cavity output takes the form of an exponentially damped sine-wave. The position signal is 90° out of phase with the tilt and angle signals; this can be used to deconvolve the position from the other signals; a full derivation of the method used to calculate the position is presented later.

The output of a monopole cavity of angular frequency ω_r is independent of position, angle and tilt and is given by

$$V_m(q, t) \propto q e^{-t/2\tau} \sin(\omega_r t) \tag{3.5}$$

3.1.3 The ATF IP Cavity BPMs

3.1.3.1 Dipole Cavities

The ATF IP area had two C-band cavity BPMs installed. They are positioned between the last final focus magnet QD0FF and the nominal beam waist. A diagram of the IP region geometry including the IP kicker (IPK) is shown in Figure 3.6.

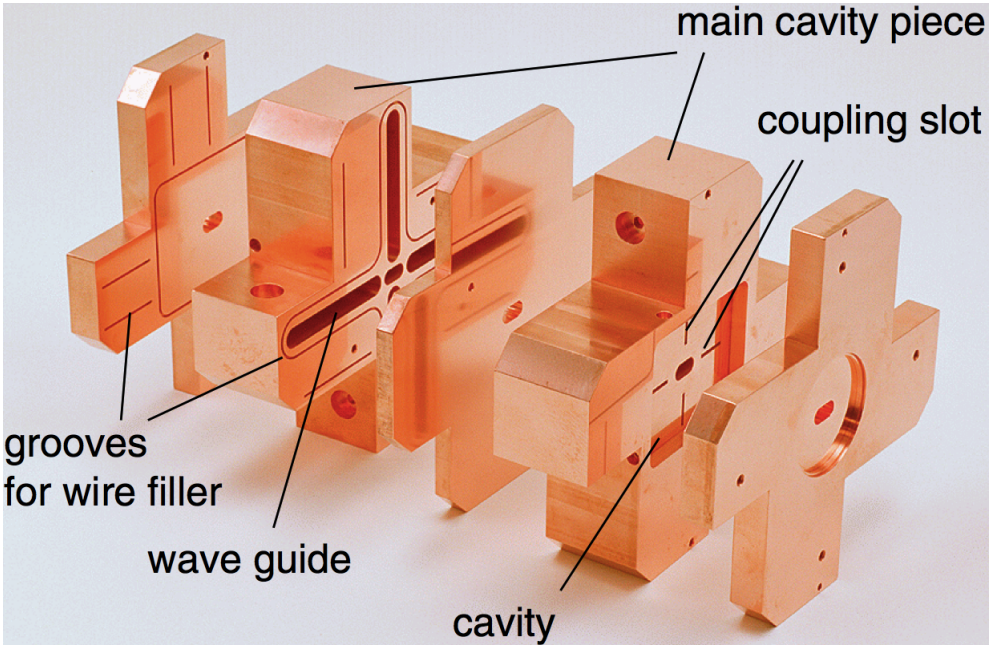

Figure 3.7: A photograph of the ATF IP cavity BPMs. Both BPMs are contained in the same block.

Parameter	Horizontal Mode	Vertical Mode
f_0 (GHz)	5.7086	6.4336
β	1.4	2.0
Q_L	2070	1207
Q_0	5337	5015
Q_{ext}	3382	1590
(R/Q) @ 1mm offset	0.549	1.598
τ (ns)	58	30
Sensitivity (mV/mm/nC)	0.952	2.061

Table 3.1: A table of simulated key parameters of the ATF IP BPMs.

Figure 3.7 [60] shows a photograph of the ATF IP cavity BPMs. The cavities were constructed from 5 pieces of copper brazed together to form a single rectangular block. This design helped isolate the horizontal and vertical dipole modes and aimed to achieve a strong dependence on position. The two dipole modes of the cavity have frequencies of 6.426 GHz in the vertical axis and 5.712 GHz in the horizontal. The isolation between the two frequencies was found to be of order 80 dB [58]. In the IP region the angular jitter of the beam is large. To reduce the cavity's dependence on the incoming beam angle the cavity was designed with a short longitudinal length of 6mm.

Key parameters include: the resonant frequencies of the dipole modes f_0; the coupling strength β; the loaded, internal and external quality factors Q_L, Q_0 and Q_{ext}; the shunt impedance (R/Q); the decay time τ and position sensitivity for the cavity were simulated [60]; they are given in Table 3.1.

3.1.3.2 Monopole Cavities

Several monopole cavities are installed along the ATF extraction line which operative using the TM_{010} mode. These cavities are used both to measure the bunch charge and as sources for LO signals for down-mixing (see Section 3.2.3.4). The frequency of the reference cavity used for the beam tests was designed to be identical to the dipole y cavity.

3.2 The ATF Cavity Signal Processing

The signals from the ATF IP BPMs are split immediately after the cavity pickoff using a 6 dB resistive splitter. The outputs of the splitter are connected to two independent signal processing schemes.

3.2.1 Heterodyne System

One of the IP BPM outputs is connected to the heterodyne processing system. It consists of a two stage down-mixing scheme: the frequency is shifted from C-band to 25 MHz using an analogue mixer and then digitised; a digital down conversion algorithm (DDC) then shifts the frequency to baseband and the position is calculated. Full details of the heterodyne scheme are given in [61].

3.2.2 Homodyne System

The Homodyne processing scheme is an alternate processing scheme is also installed at the IP. This scheme takes as input the raw C-band signals from the BPMs and down-mixes them to baseband using analogue electronics. It outputs two signals, I and Q which in combination are proportional to position, and amplifies them so they can be digitised. The experiments described herein used the homodyne electronics to measure the position as they have a considerably lower latency then the heterodyne DDC system.

The scheme works in two stages, the first down-mixes from C-band (6.4 GHz) to 714 MHz and the second to baseband. Using a two stage down-mixing process reduces the requirements on the filters used in the design and brings the filter characteristics to within the range of items readily available for purchase [62].

Returning to Equation 3.4; combining the angle and tilt terms into ϵ and adding two constants of proportionality s_p and s_a gives

$$V_d = e^{-t/2\tau} q[s_p y \sin(\omega_d t) + s_a \epsilon \cos(\omega_d t)] \tag{3.6}$$

Mixing this signal with a LO signal of frequency ω_{LO} 714 MHz lower than ω_d and renaming it I results in

$$I = e^{-t/2\tau} q[s_p y \sin(\omega_d t) A \sin(\omega_{LO}) + s_a \epsilon \cos(\omega_d t) A \sin(\omega_{LO})] \tag{3.7}$$

Expanding; including the phase difference between the dipole cavity signal and the LO signal ϕ_d; absorbing the LO amplitude term in the constants and ignoring the up-mixed terms which will be filtered by the electronics gives

$$I = e^{-t/2\tau} q[s_p y \cos((\omega_d - \omega_{LO})t + \phi_d) - s_a \epsilon \sin((\omega_d - \omega_{LO})t + \phi_d)] \tag{3.8}$$

The signal from the monopole cavity with frequency ω_r is also down-mixed using the same LO signal. The output of this down-mixer (r_I) is passed through a limiter to give a signal with a constant amplitude A represented by

$$r_I = A \cos((\omega_r - \omega_{LO})t + \phi_r) \tag{3.9}$$

where ϕ_r is the phase difference between the monopole cavity signal and the LO signal. Using r_I as an LO to down-mix the signal given by Equation 3.8 yields

$$\begin{aligned} I = \; & e^{-t/2\tau} q \\ & [s_p y \cos((\omega_d - \omega_{LO})t + \phi_d) A \cos((\omega_r - \omega_{LO})t + \phi_r) - \\ & s_a \epsilon \sin((\omega_d - \omega_{LO})t + \phi_d) A \cos((\omega_r - \omega_{LO})t + \phi_r)] \end{aligned} \tag{3.10}$$

Expanding this; ignoring the up-mixed components which are filtered by the electronics and absorbing the amplitudes in the constants gives

$$\begin{aligned} I = \; & e^{-t/2\tau} q \\ & [s_p y \cos((\omega_d - \omega_{LO} - \omega_r + \omega_{LO})t + \phi_d - \phi_r) - \\ & s_a \epsilon \sin((\omega_d - \omega_{LO} - \omega_r + \omega_{LO})t + \phi_d - \phi_r)] \end{aligned} \tag{3.11}$$

Since $\omega_d = \omega_r$ and the LO terms cancel the result in an exponentially damped DC signal dependent on two phase terms. These terms represent the phase difference between the reference and dipole signals and their respective LOs ($\phi = \phi_d - \phi_r$).

Since digital sampling will always take place at a fixed point with respect to bunch arrival the exponential term is fixed and is absorbed by s_p and s_a. This leaves

$$I = q[s_p y \cos(\phi) - s_a \epsilon \sin(\phi)] \tag{3.12}$$

If ϕ can be set to zero then rearranging

$$y = \frac{I}{s_p q} \tag{3.13}$$

gives a measurement of the position based on I, s_p and q. The q dependence was removed using two different measures of the beam charge and the scale factor s_p can be found from a calibration. Both of these are discussed later.

In practice setting ϕ to zero is difficult and can be time consuming. Instead the LO signal derived from the reference cavity is split and one half phase shifted by $\pi/2$ to yield

$$r_Q = A\sin((\omega_r - \omega_{LO}) + \phi_r) \tag{3.14}$$

Using this as an LO signal to down-mix the signal represented by Equation 3.8 and following the steps set out for I yields

$$Q = q[s_p y \sin\theta + s_a \epsilon \cos\theta] \tag{3.15}$$

Equations 3.12 and 3.15 provide a pair of simultaneous equations for y and ϵ in terms of I, Q, s_p, s_a and θ. Solving for x and ϵ gives

$$y = \frac{I'}{s_p q} \tag{3.16}$$

where I' is defined

$$I' = I\cos\theta + Q\sin\theta \tag{3.17}$$

and

$$\epsilon = \frac{Q'}{s_a q} \tag{3.18}$$

where Q' is defined

$$Q' = Q\cos\theta - I\sin\theta \tag{3.19}$$

Equation 3.16 yields the position and Equation 3.18 the combination of the angle and tilt components from the raw dipole signals.

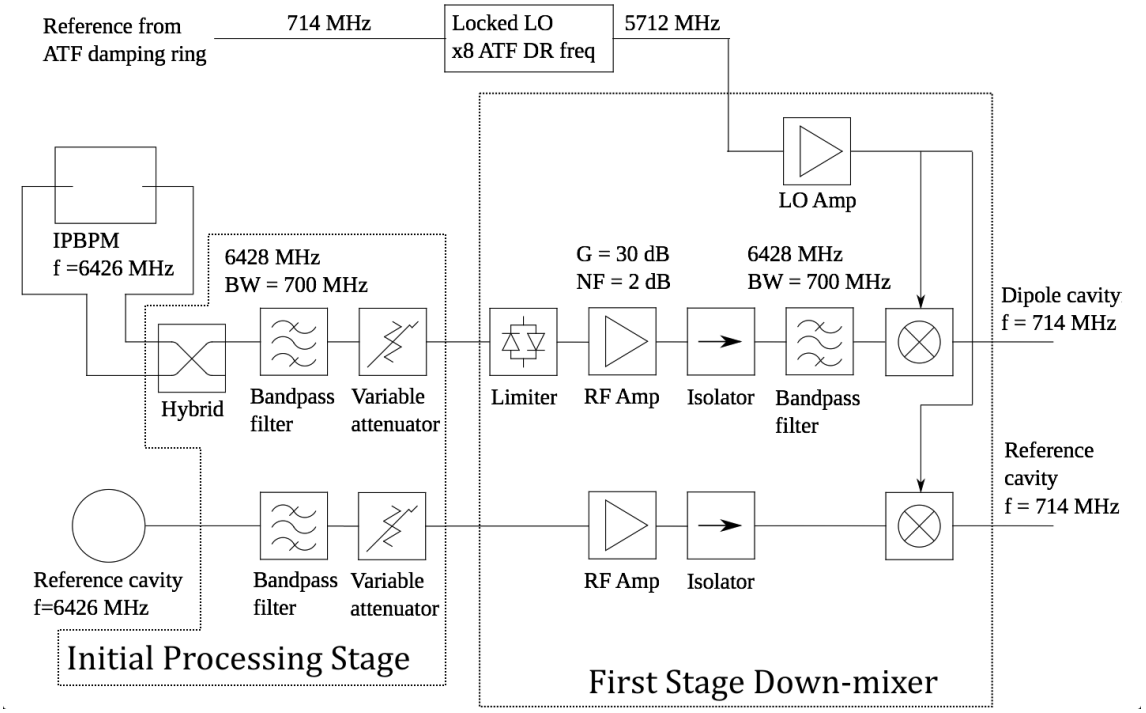

Figure 3.8: A schematic of the initial processing and first stage down-mixer.

3.2.3 Homodyne System Components

The homodyne electronics comprises four separate parts: 1) the initial processing stage which takes the raw cavity signals from the top and bottom feedthroughs and produces a single signal at the correct power level; 2) the first stage down-mixer which takes this signal and reduces its frequency from C-band to 714 MHz; 3) a second stage down-mixer to further reduce the signal's frequency from 714 MHz to baseband and produce the I and Q signals; and 4) a reference cavity processor which produces a 714 MHz LO signal phase locked to the beam and which is also a measure of the bunch charge.

Schematics of the processing scheme based on diagrams from [58] are shown in Figures 3.8 and 3.9 and a photograph of the electronics setup in the IP region at the ATF is shown in Figure 3.10. An analysis of the response of the electronics to varying input signals is described in Section 3.3.

3.2.3.1 The Initial Processing Stage

Each IP BPM has four SMA feedthrough outputs: top and bottom; and left and right. Prior to the down-mixing electronics the signals go through the pre-processing systems shown in Figure 3.8. Each pair of outputs is in antiphase with one another, the difference between these outputs is found using a 180° hybrid; this produces a signal of maximum amplitude. The hybrid also has the effect of cancelling any unwanted in phase higher order modes from the cavity. The output signal from the hybrid is passed through an Agilent Variable Attenuator [63]. This can be adjusted from outside the tunnel in steps of 10 dB. It is used to

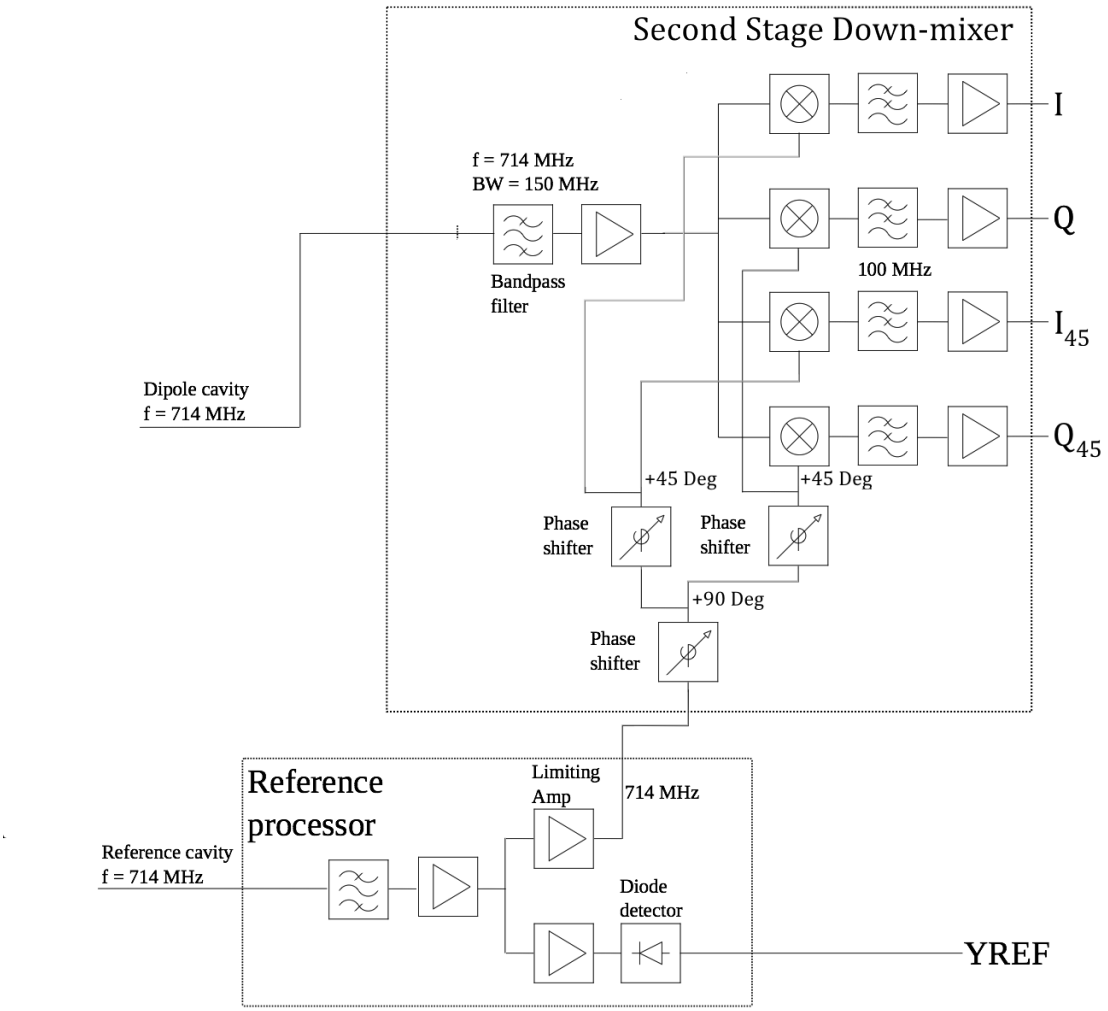

Figure 3.9: A schematic of the second stage down-mixer and reference cavity processor.

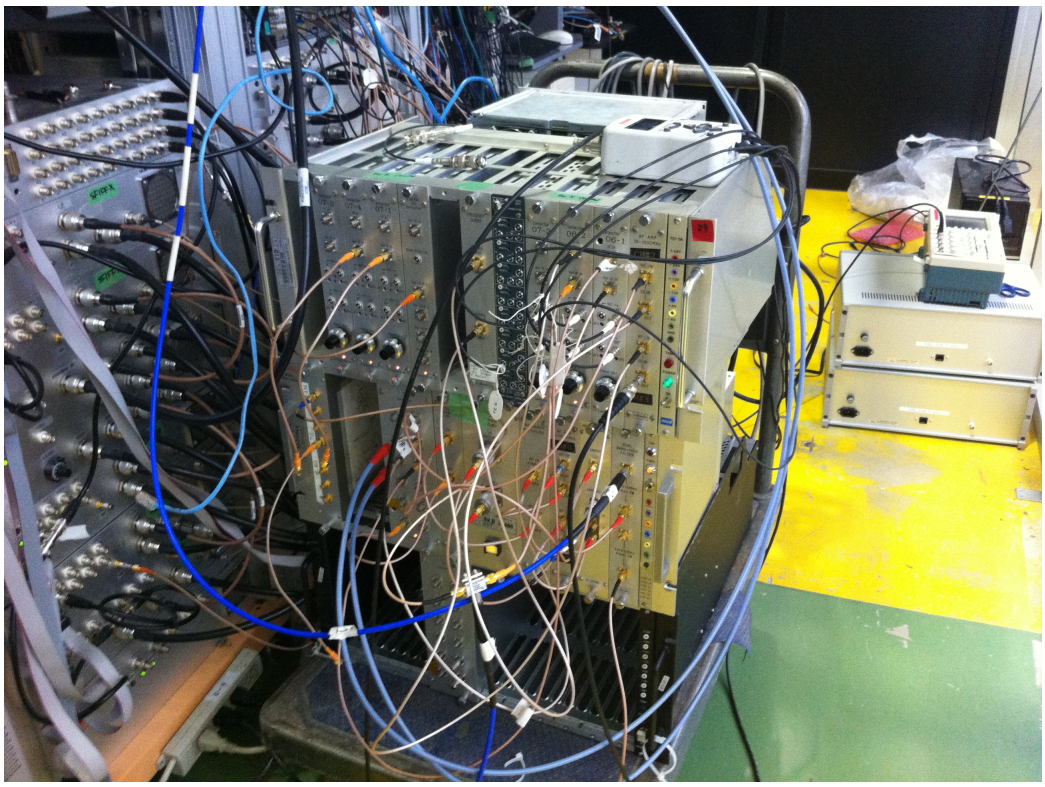

Figure 3.10: A photograph of the 'homodyne' down-mixing electronics.

control the input signal power to the processing electronics so as to ensure that no saturation occurs.

3.2.3.2 First Stage Down-mixer

The first stage down-mixer shifts the power spectrum from 6.4336 GHz to 714 MHz. First a 714 MHz signal from the damping ring is up-mixed using a series of frequency multipliers to 5.712 GHz and amplified to a power level of 1 dBm to form a LO signal in the C-band range. The signal from the variable attenuator is processed by a chain comprising a limiter; a 30 dB low noise amplifier; an isolator and finally a 714 MHz bandpass filter centred around 6.428 GHz. A mixer is used to take the product of this signal and the C-band LO.

The first stage down-mixing scheme also contains a channel to down-mix the reference cavity. This simpler scheme consists of an identical bandpass filter, amplifier, isolator and mixer to produce a signal from the reference cavity at 714 MHz.

3.2.3.3 Second Stage Down-mixer

The 714 MHz signal from the first stage down-mixer is then passed to the second stage down-mixer shown in Figure 3.9. This is used to shift the signal's power spectrum further downwards in frequency to baseband. First the signal is passed through another bandpass

filter with a 150 MHz bandwidth centred around 714 MHz. This removes any higher order components generated by the first down-mix. The signal is then split and amplified again before being split and sent to a number of mixers.

These mixers are driven by two 714 MHz LO signals produced from the reference cavity processor (described below) with one LO signal phase shifted by $\pi/2$. This produces two outputs $\pi/2$ out of phase with one another at baseband. Low pass filters cut frequency components above 100 MHz from the signal before it is amplified a final time. These signals form the I and Q outputs of the BPM processor.

In practice a slight variation of this scheme is used in the down-mixer: the two LO signals for the I and Q channels are split one further time and one of each output phase shifted by another 45°. This then provides two pairs of I and Q outputs denoted I, Q, I_{45} and Q_{45}. These pairs of outputs were found to have different responses; this is presented in Section 3.3.

3.2.3.4 Reference Cavity Processor

The final section of the processing scheme (shown in Figure 3.9) concerns the down-mixed reference cavity signal. As discussed extensively in the previous chapter on stripline BPM processing the importance of having a LO signal locked in phase to the bunch arrival cannot be overstated; although the processing for the cavity BPMs is different, the principle remains. The cavity BPM processing scheme uses the reference cavity to generate a LO signal that is phase stable with respect to the bunch. The reference cavity processing scheme takes this down-mixed signal; bandpass filters it and amplifies it.

The signal is split and half is sent to a limiting amplifier with a power output matched to the power level required by the mixers for the dipole second stage. As long as the input power level to the amplifier is above the limiting threshold this will produce a 714 MHz signal at a constant amplitude which is phase locked to the beam and can be used as an LO signal.

The other half of the signal is sent to a normal amplifier followed by a diode detector; this provides a baseband diode signal proportional to the beam charge. This signal can then be used to charge normalise the I and Q signals in the final stage of the processing scheme.

3.2.3.5 Digitisation Hardware

The I, Q and diode signals are digitised locally at the IP using a FONT5 board. Both IPA and IPB were instrumented in the vertical axis and IPB was also instrumented horizontally. The channel assignments used for the experiments were complicated by the requirements of the IP feedback algorithm. These are discussed fully in Section 6.1.2.

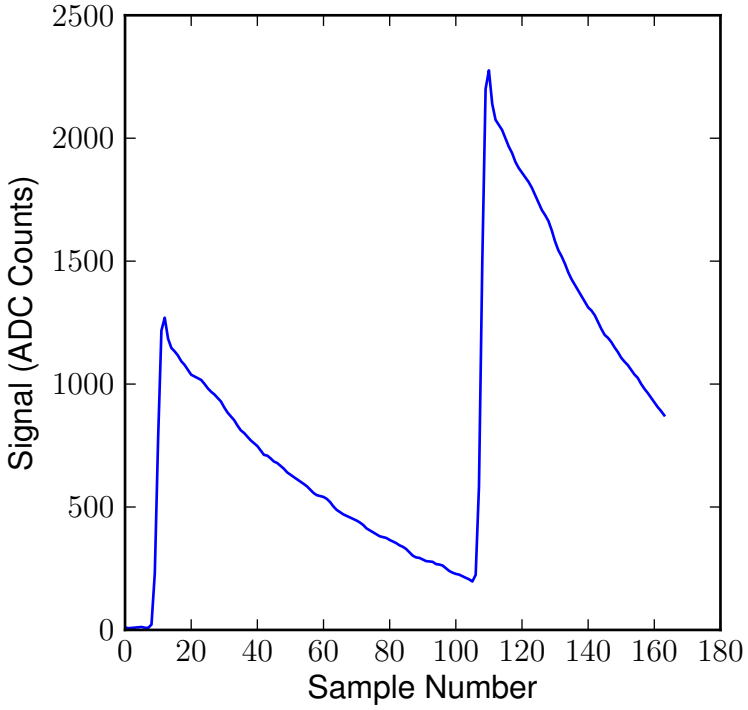

Figure 3.11: An example of the output of the diode signal vs. sample number for a trigger in two bunch mode.

3.2.4 Cavity Output

Examples of the digitised signals from the diode output and the I and Q channels are shown in Figures 3.11 and 3.12 respectively. The beam was set to two bunch mode with a bunch spacing of 274 ns or 98 digital samples. Figure 3.11 shows that the second bunch has a higher charge than the first. Examining the I and Q outputs in Figure 3.12 there is clearly some residual beating of the signal. This results from the slight frequency mismatch between the reference and dipole cavities. This is because the only reference cavity available for use at the ATF was designed for a different experiment and so had a slightly different frequency.

3.3 Signal Processing Electronics Characteristics

Section 3.2.3 describes the electronics used to process the raw cavity signals to give an analogue output proportional to position. At a simple level the electronics does two things: down-mixes the raw cavity signal from C-band to baseband and amplifies it.

The gain of the electronics is important, too high a gain can saturate the processing electronics at very small beam displacements; too low a gain will result in a poor signal to noise ratio. An effort was made to understand the gain of the electronics, how it differed between channels and over what input ranges it was linear.

Beam tests suggested that different sets of the processing electronics had different responses

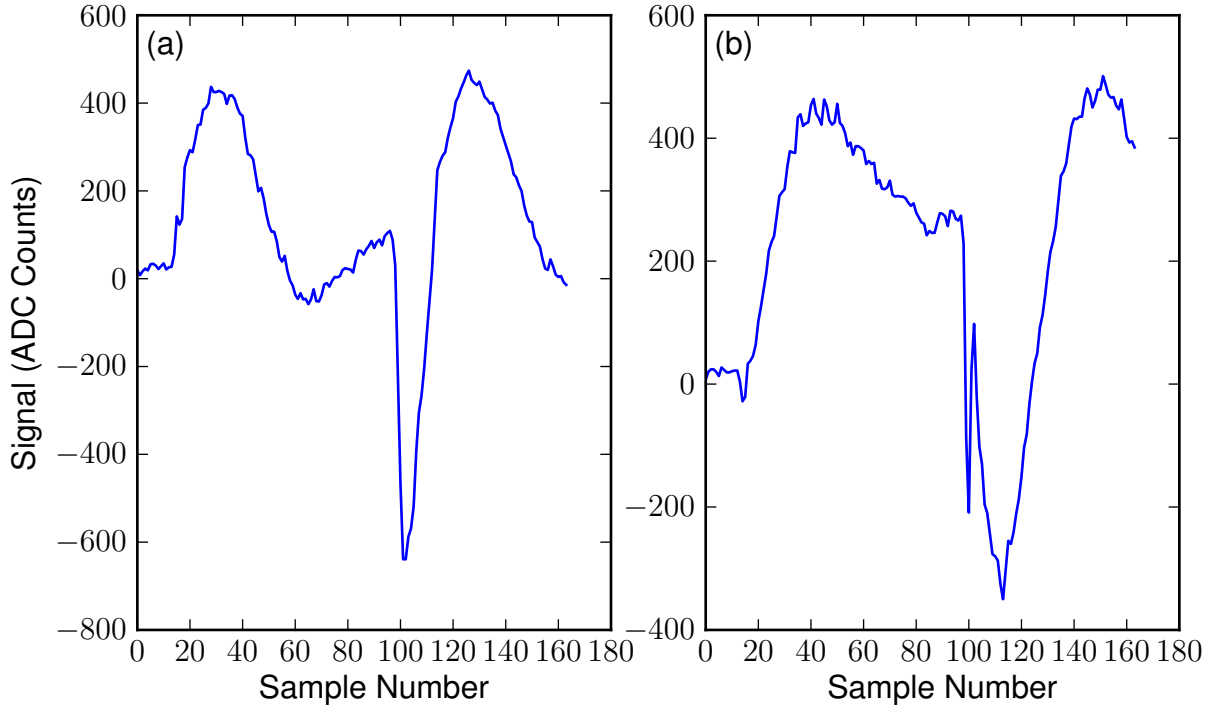

Figure 3.12: An example of the output of (a) the I channel and (b) the Q channel, vs. sample number, for a trigger in two bunch mode.

Second Stage	0° Channel Gain (dBm)	45° Channel Gain (dBm)
06 - 1	25	25
06 - 2	Non Linear	Non Linear
07 - 1	22	22
07 - 2	24	34
07 - 3	24	34
07 - 4	Non Linear	34

Table 3.2: The gain for each of the homodyne second stages.

and dynamic ranges. Switching the different sets of first stage electronics showed that all first stages had identical gain. Different second stages, however, gave different scale factors for the same BPM suggesting non-identical levels of gain.

All four outputs of each second stage were tested using a signal generator. Each second stage was given a 714 MHz LO signal at the correct input power and a separate 714 MHz signal as a simulated cavity input. The power of the cavity signal was varied to reproduce different beam displacements and the output of the I Q pair was measured using an oscilloscope. Some of the second stages were found to have two types of output gain and the gain for three pairs of the outputs was non linear.

In Figure 3.13 output power vs. input power is plotted for the 07 - 3 second stage. One of the I Q pairs has a gain of between 24 dB, the other 34 dB. The 24 dB stage is linear over a larger range than the 34 dB stage. Table 3.2 gives the gain of both outputs for all of the second stages. There are two types of output corresponding to low and high gain. The

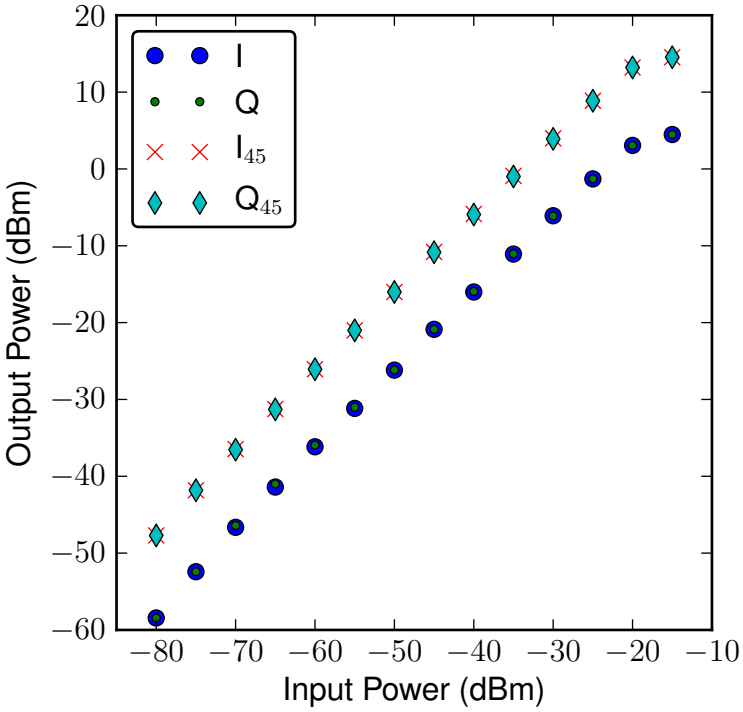

Figure 3.13: the output signal power vs. input signal power for the 07 - 3 second stage. The key denotes the points representing each output.

three non-linear second stages are noted, none of these were used in experiments. A specific second stage gain was selected for each experiment based on the level of beam jitter expected during that experiment. For experiments where a high level of beam jitter was expected a low gain second stage was selected to give a greater dynamic range; for experiments where a low level of beam jitter was expected a high gain second stage was used to increase the signal to noise ratio and thereby the resolution.

3.4 IP BPM Calibration Procedure

Since the IP BPMs are not mounted on movers, calibrations must by done be steering the beam by a known amount. The beam can be moved horizontally and vertically by varying the positions of the final focus magnets QD1FF and QD0FF respectively in the appropriate plane. If the beam waist is placed at a given BPM, data runs can be recorded at different magnet positions and used to determine the scale factor s_p and phase angle θ.

3.4.1 Beam Translation Factor

The method of moving the beam waist is to adjust the position of QD0FF. It is mounted on a mover system enabling its position in the horizontal and vertical planes to be moved in

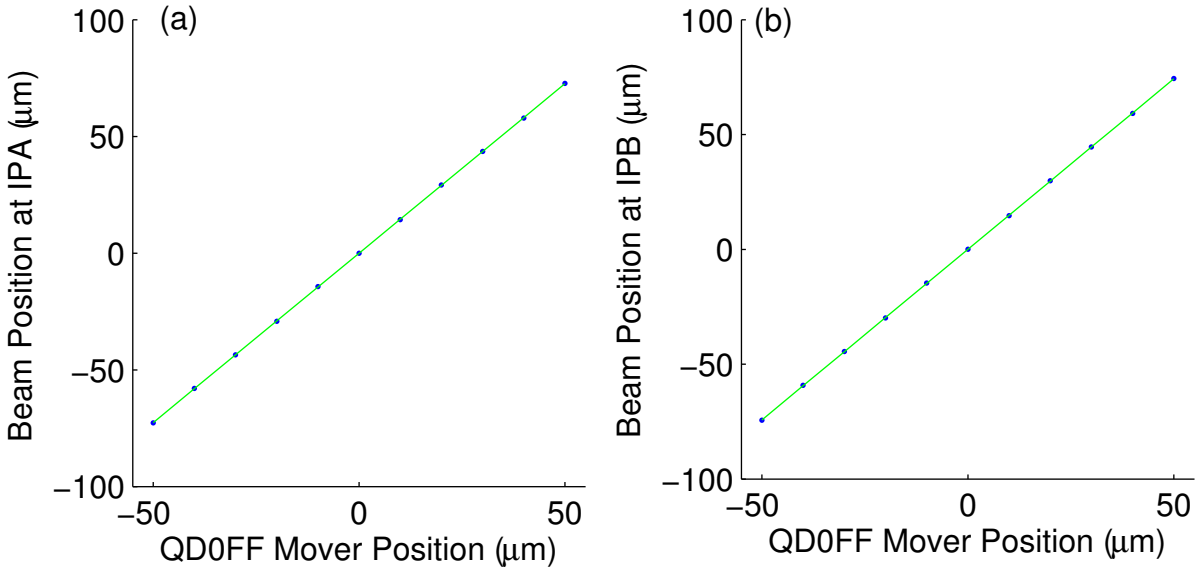

Figure 3.14: Simulated vertical beam position (blue) vs. QD0FF mover position with the beam waist at (a) IPA and (b) IPB. The green line represents a linear fit applied to the data.

steps as small as 1 μm.

When undertaking a calibration it is crucial to know how much a move in the magnet's position affects the position of the beam at a BPM. It is possible to calculate this with the beam tracking code Lucretia [64]. A simulation was performed using the model of the ATF. First a nominal lattice was setup and the currents in QD0FF and QF1FF were scanned whilst test bunches were tracked through the machine to find the currents required to place the waist longitudinally at IPA and then at IPB. The waist was then set at each of the BPMs in turn and the position of QD0FF shifted in the vertical plane whilst bunches were tracked through.

The average position of the tracked bunches at IPA and IPB vs. QD0FF magnet position is show in Figure 3.14. The gradient from the linear fit applied to the data gives the translation factor to convert a move in magnet position to beam position with the waist at a given BPM. These translation factors are shown in Table 3.3.

Attempts have been made to calculate the uncertainty on these constants. In turn the current in each of the magnets along the beamline was set to either side of its nominal position. The size of the displacement was given by the accuracy of the magnets power supply. The constant corresponding to each of these displacements was then simulated and the difference between these two values taken as the error. The errors arising from the miss-setting of all the magnets were then summed in quadrature to calculate the total uncertainty.

Waist Position	Translation Factor
IPA	1.455 ± 0.004
IPB	1.485 ± 0.004

Table 3.3: The beam translation factors for a QD0FF move along the y axis with the waist at IPA and IPB.

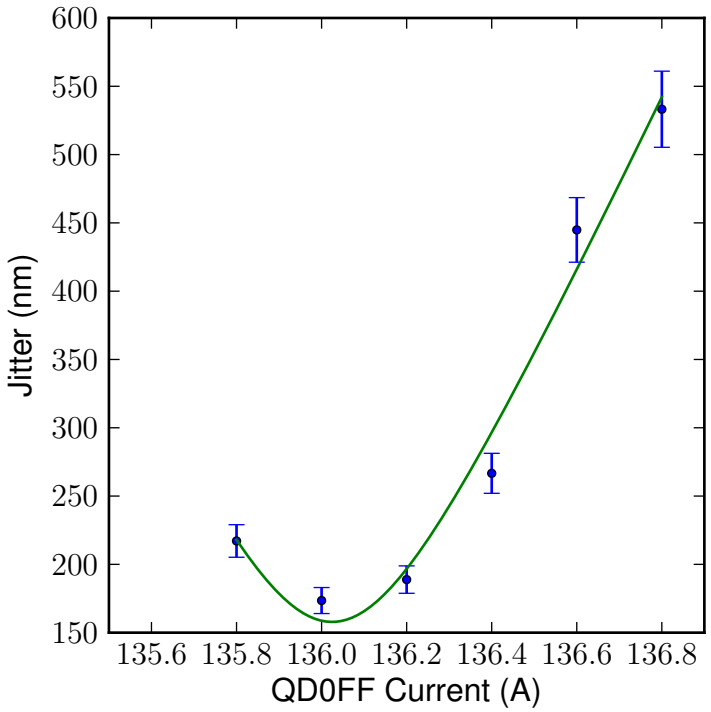

Figure 3.15: Vertical beam position jitter at IPB measured in the heterodyne system (blue) vs. QD0FF current for a waist scan. The green line represents a parabolic fit applied to the data.

3.4.2 Calibration Procedure

3.4.2.1 Transverse Beam Position

To ensure an accurate calibration it was crucial to place the beam waist at the longitudinal position of the BPM being calibrated. The initial stage of each calibration was therefore a waist scan - similar to that described in Section 3.5.1. The scan was done in single bunch mode and the beam jitter was measured using the heterodyne system described in Section 3.2.1.

An example of an IP waist scan taken around IPB is shown in Figure 3.15. A parabolic fit gives the current setting that places the beam waist at the BPM as 136.02 A.

For each BPM with the waist positioned at either IPA or IPB the beam was centred in the x-y plane. The beam was moved transversely either side of the centre position and the point where the system saturated was noted. This gave a centre point and range for the calibration. The beam was then moved in steps across this range by varying the position of

QD0FF and data was recorded at each of these steps.

3.4.2.2 Sample Point Selection and Flyer Rejection

The cavity signal takes the form of an exponentially damped sine wave and can be sampled at any point along the wave. Due to the positions of the reference and dipole cavities in the beam-line the reference LO signal arrived at the input to the second stage down-mixer after the dipole signal. At the start of the dipole cavity signal there was therefore a transient period before a reference LO signal arrived. As time progresses the amplitude of the cavity signal falls and the signal to noise ratio decreases. Selecting a sample point that was either too early or late would therefore degrade the BPM resolution. An algorithm to select a sample point was devised based on when the peak of the diode signal occurred:

1. Calculate the sample number where the peak of the diode signal occurs for all triggers in a data run
2. Find the modal value of this list
3. Offset the sample point from the mode by five

Five was chosen as this ensured enough time for the reference LO signal to arrive yet was close enough to the peak of the diode signal to ensure a large amplitude. The data was binned for each step in the beam position scan and the I, Q and diode signals at the sample point were found. The average and standard deviation of the I, Q and diode signals for each bin were calculated and triggers more than three standard deviations away from the mean were excluded as flyers. QD0FF is a large magnet with considerable weight, hence it was observed to be in motion for a short time after a command to move was sent. To ensure the magnet was stationary whilst data was being recorded the first two triggers for each bin were excluded, this was judged to be long enough as motion over three consecutive samples was never observed.

3.4.2.3 Phase Angle (ϕ)

The phase angle ϕ was calculated directly from the beam position scan. Returning to Equations 3.12 and 3.15 and rearranging gives

$$Q = I\frac{\sin\phi}{\cos\phi} + \frac{s_a\epsilon}{\cos\phi} \tag{3.20}$$

Figure 3.16 shows Q vs. I for all triggers over a QD0FF position scan after the 'flyer' triggers have been removed for (a) bunch one and (b) bunch two. ϕ is given by the inverse tangent of the gradient of the linear fit to the data and are shown in Table 3.4. The statistical uncertainty on the phase angle is calculated from the error on the fit.

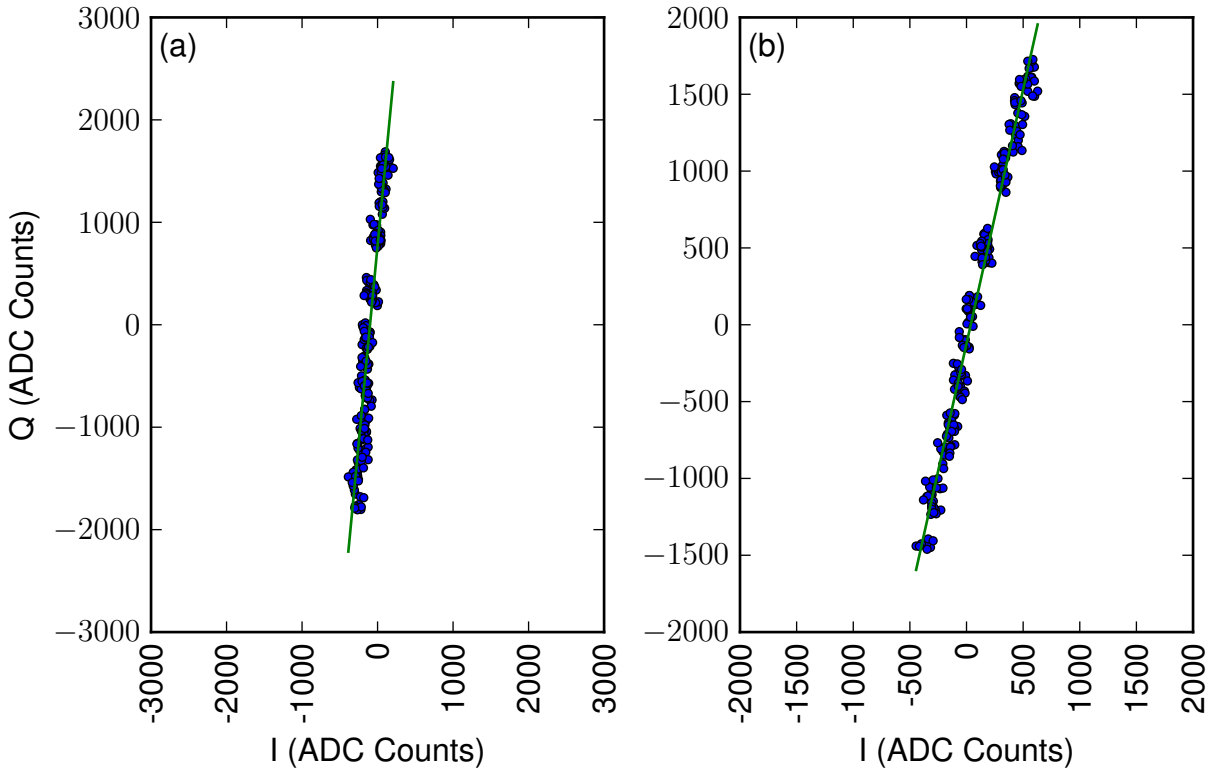

Figure 3.16: Q vs. I (blue) for (a) the first and (b) the second bunch for a QD0FF position scan measured at IPB. The green lines represent linear fits applied to the data.

BPM	Bunch One ϕ (°)	Bunch Two ϕ (°)
IPA	11.3 ± 0.3	2.3 ± 0.2
IPB	82.6 ± 0.2	73.0 ± 0.2

Table 3.4: ϕ for IPA and IPB. The errors represent the statistical uncertainty on the constants.

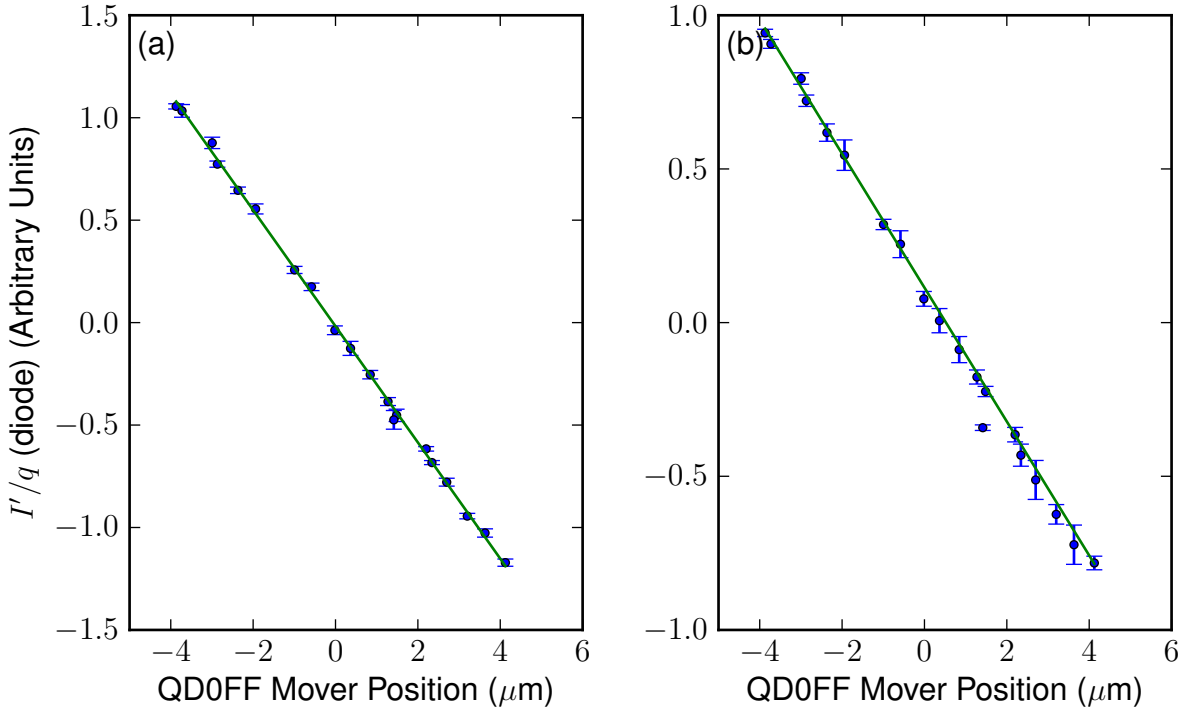

Figure 3.17: I'/q (blue) vs. beam position at IPB for (a) the first and (b) the second bunch using the diode as a measure of the bunch charge. The green lines represent linear fits applied to the data. The error bars represent the statistical uncertainty on each data point.

BPM	Bunch One Scale Factor	Bunch Two Scale Factor
IPA	49.3 ± 0.1 ± 0.3	61.0 ± 0.2 ± 0.3
IPB	5.35 ± 0.01 ± 0.04	-6.65 ± 0.02 ± 0.05

Table 3.5: Scale factors for IPA and IPB. The first errors represents the statistical uncertainty on each constants, the second error represents the systematic uncertainty on each constant.

3.4.2.4 Scale Factor (s_p)

Once I' was calculated using the phase angle it must be charge normalised to produce a signal proportional to beam position. A measurement of the beam charge was obtained from the diode signal. Figure 3.17 shows I'/q vs. beam position derived from the QD0FF magnet mover position. From the linear fits scale factors have been obtained which convert I'/q to beam position in microns, they are shown in Table 3.5. Statistical uncertainties on the scale factors have been calculated from the error on the fits, systematic uncertainties have been calculated from the error on the beam translation factor.

3.5 Estimates of the IP BPM Resolution

The ATF IP BPMs are situated between the final doublet and the nominal IP. This results in large incoming beam angles and exceptionally large position and angular jitter. The position

Bunch	Jitter (nm)
1	103 ± 9
2	108 ± 10

Table 3.6: The minimum measured jitter in the QD0FF waist scan. The errors represent the statistical uncertainty on the results.

jitter can be reduced by shifting the focus away from the nominal IP and towards one of the BPMs however the angular component remains and the jitter is still large at the other BPM. This results in a particularly difficult environment to measure BPM resolution when this is small in comparison with the beam jitter.

In addition there are only two IP BPMs in the area which precludes using the method of calculating BPM resolution discussed in Section 2.8.2. Two alternative methods were used to give estimates of the resolution of the IP BPMs: waist scans and the single value decomposition (SVD) method. Waist scans were used during the experiments at ATF and the SVD method has been used to cross check this method.

3.5.1 Waist Scans

The observed minimum beam jitter at a BPM ($\tilde{y}^M$) can be taken as an upper limit on its resolution (σ). Furthermore as the actual beam jitter ($\tilde{y}^a$) and BPM resolution are two independent Gaussian quantities they will sum in quadrature; if an independent estimate of the beam jitter can therefore be found the actual BPM resolution can be obtained by rearranging

$$\tilde{y}^{M^2} = \tilde{y}^{a^2} + \sigma^2 \tag{3.21}$$

The beam jitter at the ATF beam waist is typically quoted as 20% of the beamsize [65]. The data presented in the experiments herein was taken with beam sizes typically of order 100 nm [66] which therefore implies beam jitters at the waist of approximately 20 nm.

Waist scans were used to find the minimum measured beam jitter from which an estimate of the BPM resolutions could be obtained. First the IP BPMs were setup and calibrations were obtained using the method described. The strength of QD0FF was varied to scan the beam waist longitudinally through one of the IP BPMs in small steps. Varying the strength of QD0FF also changes the transverse beam position and accordingly it was re-centred at each step. A long data run was recorded at each step and from this the jitter was calculated.

An example waist scan around IPB for both bunches is shown in Figure 3.18. The jitter varies linearly around the minimum which occurs when the beam waist was positioned at IPB. The minimum beam jitter for both bunches is given in Table 3.6. Assuming $\delta_A = 20$ nm; the minimum measured jitter is almost entirely due to resolution giving a measure of the BPM's resolution at 101 nm and 106 nm for the first and second bunches respectively.

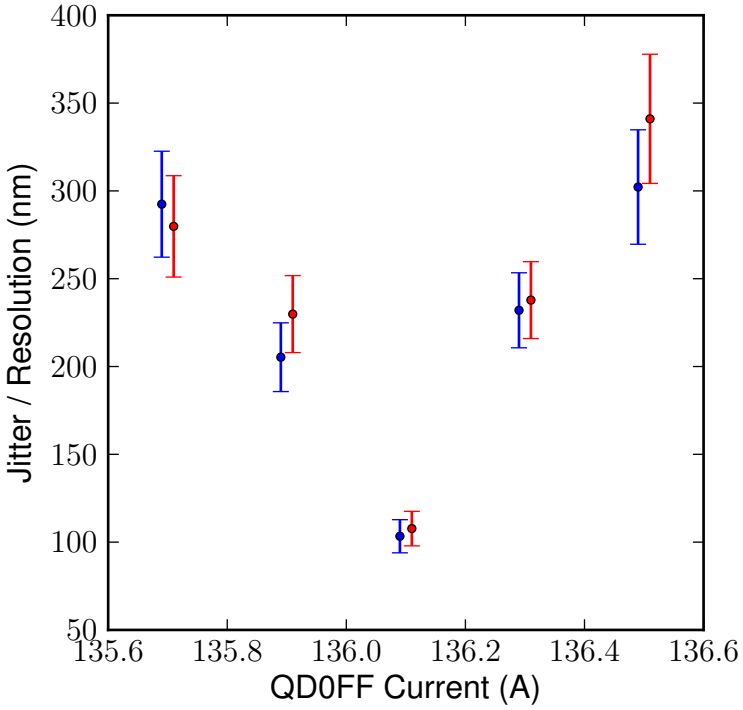

Figure 3.18: Beam jitter vs. QD0FF current of the first (blue) and second (red) bunch for a waist scan. The error bars represent the statistical uncertainty on each data point. A slight horrizontal offset has been introduced to the two data sets to guide the eye.

3.5.2 The SVD Method

Theoretically the position at any point in the lattice can be predicted using the position at two other points not in phase with one another. In practice if the position of many points at varying phases is measured it is possible to get a good estimate of the position at any given point in the lattice. The cavity BPM system at the ATF has demonstrated consistent sub 100 nm resolution using BPMs positioned throughout the ATF final focus system [67].

These positions can be used to predict the position at one of the IP BPMs. Using single value decomposition it is possible to fit a vector of coefficients which relate beam position throughout the lattice to the beam position at the IP. The difference between the predicted position and the measured position at the BPM can then be calculated and the standard deviation of this gives an estimate of the resolution. A full explanation of this method is given in [61].

The cavity BPM system only provides information about the first bunch; from this an estimate of the first bunch resolution has been calculated using the same data as the IP waist scan. The method yields a resolution of 123 ± 16 nm which agrees with the result from the IP waist scan.

3.6 Methods for Improving the Resolution

Several offline methods for improving the resolution have been investigated.

3.6.1 Sample Point Optimisation

The importance of selecting an appropriate sample point - denoted here as i - was previously discussed. A method to calculate the optimum sample point was devised. The sample point corresponding to the peak of the diode signal was calculated for all triggers in a calibration run. The mode of this was defined as $i = 0$ and used as the starting point for the optimisation. A calibration was then performed at different succeeding offsets from this sample point to give calibration constants θ_i and s_i . These calibrations were used to calculate the jitter at a number of successive sample points in the range $0 \leq i \leq N$.

A plot of vertical position jitter vs. sample point for (a) the first bunch and (b) the second bunch measured in IPB is shown in Figure 3.19. The point at $i = 0$ has been excluded from the results as the jitter is so large at this point it swamps the other results. Considering (a) at small sample point offsets the resolution is very poor due to the low quality signal from the reference cavity. This results in a large measured beam jitter; as the sample point moves away from the transient region the resolution of the BPM improves and the jitter reduces. In (b) there is a residual LO signal from the first bunch in the reference cavity so this initial transient region does not occur. As the sample point offset is increased further the resolution falls off exponentially as the signal to noise ratio decreases. At the beginning of each shift a long data run was recorded and subjected to this analysis. The sample point which provided the minimum measured beam jitter was selected and used for later experiments conducted in the same shift.

3.6.2 Sample Point Averaging

To increase the signal to noise ratio an average of the signal values over a number of sample points can be calculated. Different types of averages have been tested and are presented here. All averages take the sum over a number of sample points. The optimum sample point (defined in Section 3.6.1) was used as the first point in the sum and here is denoted as $j = 0$, the points directly succeeding the optimum sample point were then used up to $j = N$. Four averaging methods were tested.

3.6.2.1 *I*-*Q* Signal Averaging

Restating Equations 3.16 and 3.17 together yields

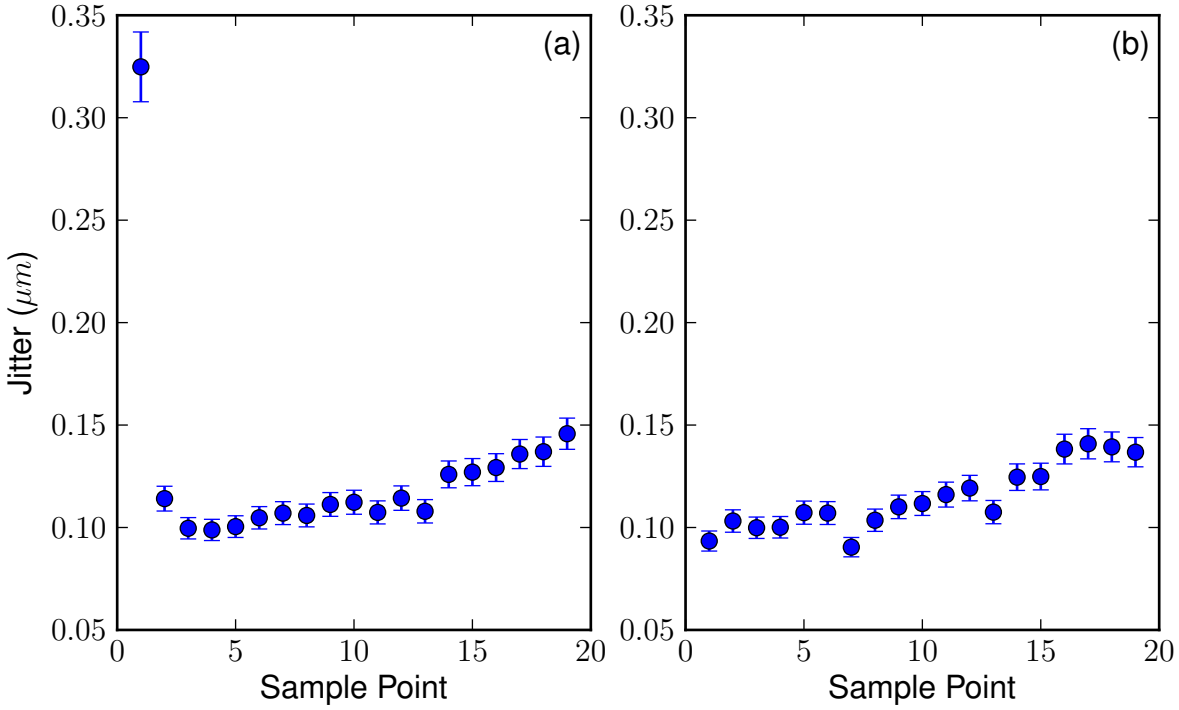

Figure 3.19: Measured vertical beam position jitter vs. sample number for (a) the first bunch and (b) the second bunch. The error bars represent the statistical uncertainty on each data point.

$$y = \frac{1}{q_j s_j}(I_j \cos\theta_j + Q_j \sin\theta_j) \tag{3.22}$$

where j denotes the sample point used for the calculation and s_p has been restated as s_j. The simplest method of sample point averaging is to calculate I and Q from a sum of several successive sample points

$$y = \sum_{j=0}^{N} \frac{1}{q_0 \bar{s}}(I_j \cos\bar{\theta} + Q_j \sin\bar{\theta}) \tag{3.23}$$

In this method the diode signal is not averaged and q_0 is used for all points. The calibration constants $\bar{s}$ and $\bar{\theta}$ are calculated after the summation and so represent the average calibration constant for the sample points $0 \leq j \leq N$.

3.6.2.2 I-Q-Diode Average

An extension to the I-Q average procedure is to include in the summation the charge signal

$$y = \sum_{j=0}^{N} \frac{1}{q_j \bar{s}} (I_j \cos\bar{\theta} + Q_j \sin\bar{\theta}) \tag{3.24}$$

3.6.2.3 Complete Average

Both averaging techniques described above assume the phase angle used to transform raw I and Q into I' remains constant over the range of samples - this is not the case. A more complete method is to perform a calibration at each of the sample points to calculate θ_j. The position can then be calculated from

$$y = \sum_{j=0}^{N} \frac{1}{q_j \bar{s}} (I_j \cos\theta_j + Q_j \sin\theta_j) \tag{3.25}$$

This technique contains the most information of the three so far, computationally it is also the most taxing, something that should be considered if it were to be used in a feedback algorithm.

3.6.2.4 Weighted Average

The final method attempted was an extension of the complete average. Here instead of taking a simple arithmetic mean a weighted average can be used. The weighting was based on the decay rate of the cavity signal $e^{j/\tau}$ where τ was the cavity decay constant (30 ns) written in units of sample points. The position was then given by

$$y = \sum_{j=0}^{N} e^{j/\tau} \frac{1}{q_j \bar{s}} (I_j \cos\theta_j + Q_j \sin\theta_j) \tag{3.26}$$

3.6.2.5 Comparison of Different Methods

The jitter was calculated by applying each of the averaging methods described to the same data run over an increasing number of sample points. The results are shown in Figure 3.20 and for the first and second bunches in Tables 3.7 and 3.8 respectively. They all demonstrate an improvement to the resolution with the weighted average giving the best result. Initially as more sample points are used the resolution of the BPMs improves manifesting itself in a lower measured jitter. As the number of sample points increases the improvement tails off.

Sample point averaging was not used during the experiments at ATF as it not integrated into the firmware. Hence the results presented in later chapters have not used sample point averaging. Going forward this is something that should be considered when new firmware is

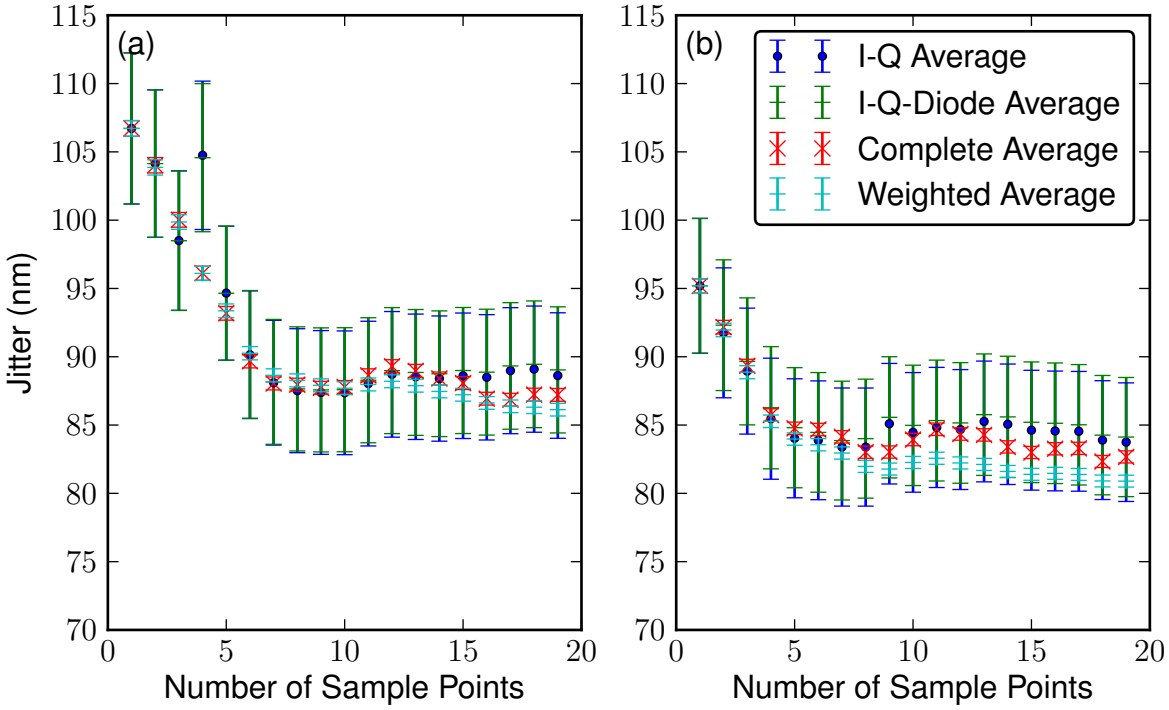

Figure 3.20: Measured vertical beam position jitter vs. number of sample points used in sample point average for (a) the first bunch and (b) the second bunch using different sample point averaging techniques. The error bars represent the statistical uncertainty on each point.

being developed.

3.7 Summary

This chapter gives a brief introduction to cavity BPMs and outlines the theory of their use. The signal processing scheme used at the ATF is explained and the details of the processing electronics and their characteristics presented.

The procedures used to calibrate the BPMs for the work described herein are detailed along with examples of such calibrations. The resolution of the BPMs is calculated using a waist scan and found to be approximately 100 nm for both bunches, a second calculation using SVD provides a cross check which agrees with the waist scan. Finally two methods to improve the resolution of the BPMs: sample point selection and sample point averaging are set out; these methods achieved a final resolution of approximately 85 nm.

No. of Sample Points	I-Q (nm)	I-Q-Diode (nm)	Complete (nm)	Weighted (nm)
1	110 ± 6	110 ± 6	110 ± 1	110 ± 1
2	100 ± 5	100 ± 5	100 ± 1	100 ± 1
3	99 ± 5	98 ± 5	100 ± 1	10 ± 1
4	100 ± 5	100 ± 5	96 ± 1	96 ± 1
5	95 ± 5	95 ± 5	93 ± 1	93 ± 1
6	90 ± 5	90 ± 5	90 ± 1	90 ± 1
7	88 ± 5	88 ± 5	88 ± 1	89 ± 1
8	88 ± 5	88 ± 5	88 ± 1	88 ± 1
9	87 ± 5	88 ± 5	88 ± 1	88 ± 1
10	87 ± 5	88 ± 5	88 ± 1	88 ± 1
11	88 ± 5	88 ± 5	89 ± 1	88 ± 1
12	89 ± 5	89 ± 5	89 ± 1	88 ± 1
13	89 ± 5	89 ± 5	89 ± 1	88 ± 1
14	88 ± 5	89 ± 5	88 ± 1	87 ± 1
15	89 ± 5	89 ± 5	88 ± 1	87 ± 1
16	88 ± 5	89 ± 5	87 ± 1	87 ± 1
17	89 ± 5	89 ± 5	87 ± 1	86 ± 1
18	89 ± 5	89 ± 5	87 ± 1	86 ± 1
19	89 ± 5	89 ± 5	87 ± 1	86 ± 1

Table 3.7: Measured first bunch vertical beam position jitter using a different number of sample points and different averaging techniques. The errors represent the statistical uncertainty on the results.

No. of Sample Points	I-Q (nm)	I-Q-Diode (nm)	Complete (nm)	Weighted (nm)
1	95 ± 5	95 ± 5	95 ± 1	95 ± 1
2	92 ± 5	92 ± 5	92 ± 1	92 ± 1
3	89 ± 5	90 ± 5	89 ± 1	89 ± 1
4	85 ± 4	86 ± 4	86 ± 1	85 ± 1
5	84 ± 4	85 ± 4	85 ± 1	84 ± 1
6	84 ± 4	84 ± 4	85 ± 1	84 ± 1
7	83 ± 4	84 ± 4	84 ± 1	83 ± 1
8	83 ± 4	84 ± 4	83 ± 1	82 ± 1
9	85 ± 4	86 ± 4	83 ± 1	82 ± 1
10	84 ± 4	85 ± 4	84 ± 1	82 ± 1
11	85 ± 4	85 ± 4	85 ± 1	83 ± 1
12	85 ± 4	85 ± 4	84 ± 1	82 ± 1
13	85 ± 4	86 ± 4	84 ± 1	82 ± 1
14	85 ± 4	86 ± 4	83 ± 1	82 ± 1
15	85 ± 4	85 ± 4	83 ± 1	81 ± 1
16	85 ± 4	85 ± 4	83 ± 1	81 ± 1
17	85 ± 4	85 ± 4	83 ± 1	81 ± 1
18	84 ± 4	84 ± 4	82 ± 1	81 ± 1
19	84 ± 4	84 ± 4	83 ± 1	81 ± 1

Table 3.8: Measured second bunch vertical beam position jitter using a different number of sample points and different averaging techniques. The errors represent the statistical uncertainty on the results.

Chapter 4

Effect of Upstream Feedback at the IP

A coupled loop feedback system designed to correct the incoming vertical beam angle and position jitter has been installed in the extraction line at the ATF. Previous beam tests of the system are reported in [68] and [69]. Efforts to measure the transfer of the beam correction downstream are presented here. The feedback was operated in the upstream region and beam position and jitter were measured at the IP.

4.1 Upstream Feedback Experimental Setup

A diagram of the upstream feedback system is given in Figure 4.1. It comprises three stripline BPMs and their processing electronics; two pulsed kicker amplifiers with pre kicker amplifiers; two stripline kickers and a FONT5 digital board. The system is interleaved in the beam-line with quadrupoles. The striplines and their processing electronics are described fully in Chapter 2.

P2 and K1 and P3 and K2 form the two loops of a coupled feedback system designed to stabilise both the position and angle of the second bunch in the train. The layout of the components to create such a system is discussed next.

The upstream feedback system implements a correction to the second bunch based on the position and angle of the first. It is therefore reliant on a good correlation between the position and angle of the first and second bunches.

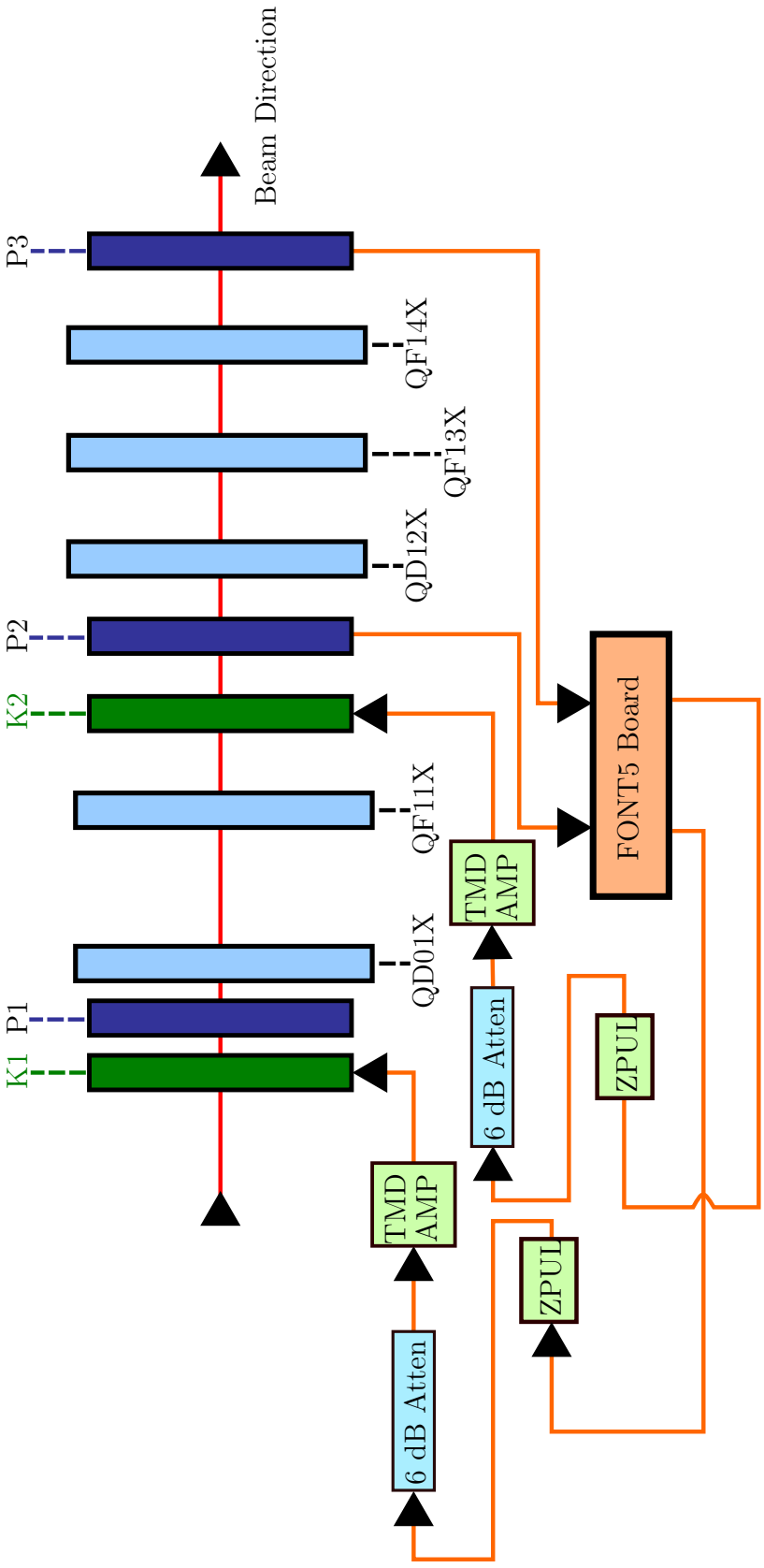

Figure 4.1: Block diagram of the upstream feedback system. The three stripline BPMs P1, P2 and P3 are shown along with the two stripline kickers K1 and K2 which are interleaved with quadrupoles in the lattice. The electrical components used in the FONT upstream feedback system are also shown.

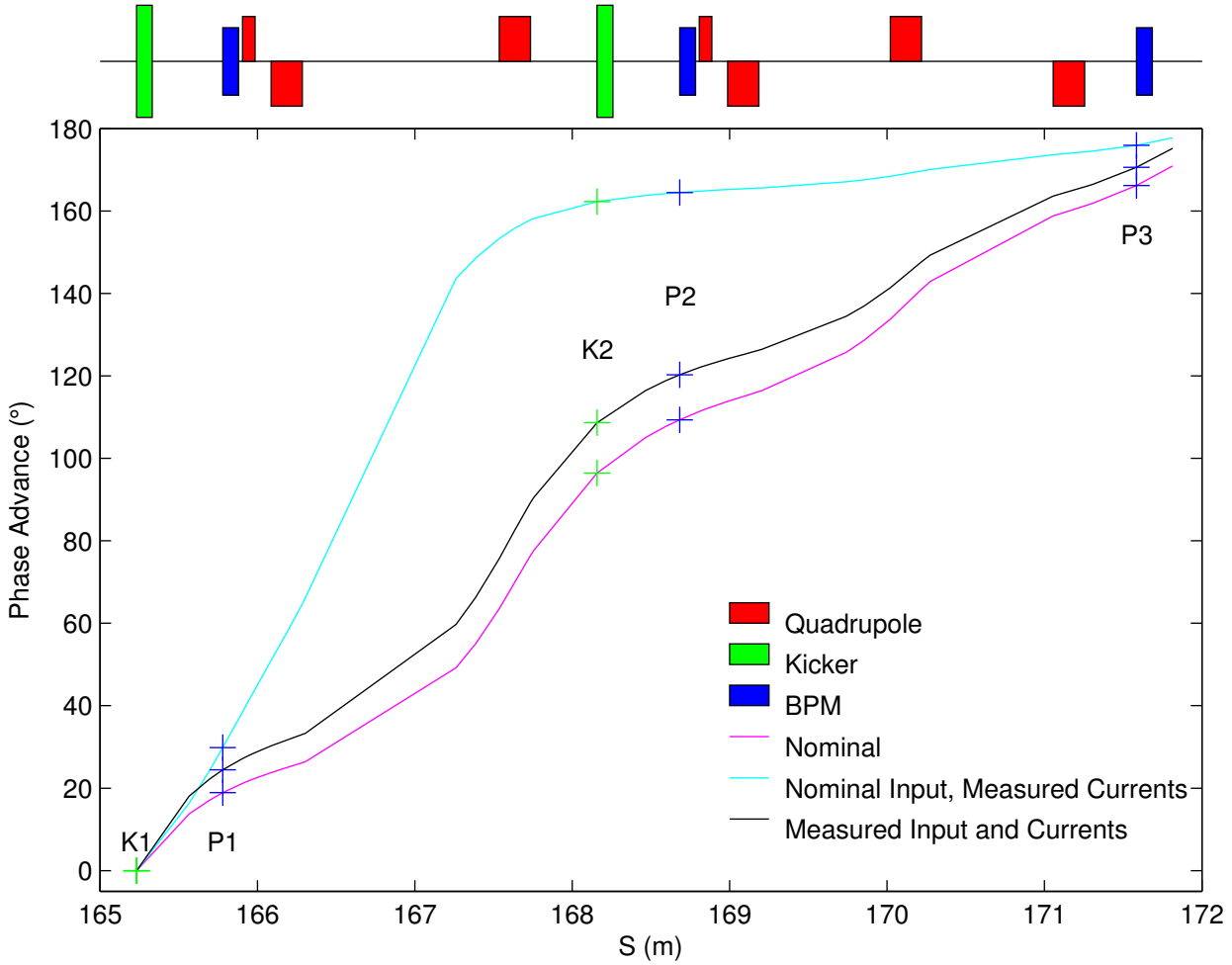

Figure 4.2: The phase advance vs. position along the beamline in the upstream region as designed (black) and as during experiments (magenta).

4.1.1 Phase Advance

Figure 4.2 shows phase advance vs. position along the beamline under the nominal optics; using the nominal input beam and the magnet settings for which the experiments presented herein were conducted; and using input beam parameters measured prior to the day on which experiments were performed and the magnet settings used for the experiments. The phase advance between key components in the upstream system is given in Table 4.1; the phase advance between components in the upstream system and IPA and IPB is given in Table 4.2.

4.1.1.1 Design Phase Advance

P1 is placed directly after the first stripline kicker; their proximity means the kicker has little effect on the beam position as measured by P1, which therefore acts as a witness BPM measuring the incoming beam position entering the feedback system.

Element	Nominal (°)	Nom. Input, Meas. Mag. (°)	Meas. Input and Mag. (°)
K1 → K2	96	162	109
K1 → P2	109	164	120
K1 → P3	166	176	170
K2 → P2	13	2	12
K2 → P3	70	13	62
P2 → P3	57	11	50

Table 4.1: The phase advance between key components in the upstream system under a range of different accelerator conditions.

Element	Phase Advance to IPA (°)	Phase Advance to IPB (°)
K1	253	260
K2	145	151
P2	132	140
P3	83	89

Table 4.2: The phase advance between key components in the upstream and IP systems using measured input beam and the magnet settings used for experiments.

As stripline kickers, K1 and K2 will introduce a purely angular displacement to the beam. The design optics places them at orthogonal points in the lattice and so a deflection at K1 will manifest itself as a position change at K2. K1 and K2 therefore combine to cover all parts of phase space and can affect a deflection to both the angle and position components of the beam's trajectory.

P2 and P3 are placed 57° degrees apart in the lattice. In combination they can therefore be used to reconstruct the complete beam trajectory. In combination with the two orthogonal kickers they form a coupled loop feedback system that will act to correct both the angle and position components of jitter in all areas of phase space.

As long as the two BPMs are not at identical phases some linear combination of them can be used to reconstruct the complete trajectory of the beam. More important is the phase advance between the two kickers: they should be perfectly out of phase with one another to affect all parts of phase space.

4.1.1.2 Actual Phase Advance

Simulating the phase advance in the upstream region is not a trivial exercise due to the methods used for small beam spot size tuning at the ATF2: The beam extracted from the damping ring has Twiss parameters which differ from those designed. The final focus system is very sensitive to the incoming beam parameters and so input of this mismatched beam would result in emittance blow-up and a large beam spot size at the beam waist. The matching quadrupoles in the extraction line are therefore used to match the Twiss parameters from the damping ring measured at the entrance to the final focus using an OTR. This is a device which places a fluorescent screen into the path of the beam which emits optical light when it interacts with the beam. A camera is then used to record this radiation and from

this a measurement of the Twiss parameters can be gained. The matching quadrupoles are interleaved with the components of the upstream system so when they are varied to match the Twiss parameters the phase advance in the upstream region is also changed.

It is possible to simulate the phase advance in the upstream region with the actual magnet settings using the 'Flight Simulator' [57] however the model still requires a set of input beam parameters. Two approaches to calculating the phase advance have been taken: 1) The magnet setting used on the day have been input to the 'Flight Simulator' and the nominal beam parameters output from the damping ring have been assumed. 2) Some of the beam parameters were measured at OTR0 the day before these experiments took place, these parameters have been input to the 'Flight Simulator' along with the magnet settings used on the day. The Twiss parameters have then been reverse tracked to the beginning of the extraction line to give input beam parameters for the simulation, these have then been used to calculate the phase advances in the upstream region. The two methods yield different phase advances, both of which are shown in Figure 4.2 and Table 4.1.

Considering first the case using the nominal input beam, the actual phase advance in the upstream region is quite different from the intended design: most importantly K1 and K2 are near anti-phase with one another and so will be unable to introduce a correction into both dimensions of phase space. Additionally K2 in particular is well in phase with both P2 and P3 and so will have a constrained effect on the beam position at either. In this situation the two feedback loops correct jitter in largely the same portion of phase space. Any jitter in the uncovered portion remains and will be present as the beam propagates downstream.

Considering the second case where the input beam parameters have been constructed from some measured parameters at OTR0 the phase advance is closer to that designed. The phase advance between the two kickers is still greater than in the nominal optics and so will place a constraint on the effectiveness of the feedback system. As the measured beam parameters for this method were recorded the day prior to the experiments it is probable that they will have changed. In particular it is likely the dispersion throughout the beam-line will be greater than that used and this will have the effect of slightly increasing the phase advance between the two kickers. Furthermore many of the beam parameters were not measured and so nominal parameters have been assumed, in particular a nominal beam energy has been used and this could have a noticeable effect on the phase advance.

These facts were discovered too late for the beam tests presented herein, and therefore have a degrading effect on the results. However as shown in Tables **??** and 4.2 in both cases P2 is still partially in phase with the two IP BPMs. This means that the correction in the upstream region at P2 should still have a noticeable effect at the IP.

Going forward a simulation is being undertaken to model the effects of the phase advance in the upstream region on the propagation of the jitter correction. Further beam tests are also being planned to measure these effects and a procedure to measure the extracted beam's Twiss parameters accurately has been devised.

4.1.2 Kicker Amplifiers

The signal from each DAC undergoes a two stage amplification before it is input into the kicker. A Mini-Circuits ZPUL-21 [70] pre amplifier placed immediately after the DAC provides 21 dB of gain. This, in combination with a 6 dB attenuator, provides the correct gain to match the full output of the DAC to the dynamic range of the kicker amplifier. The signal is then amplified further by a kicker amplifier built by TMD Technologies [71]. Three kicker amplifiers were produced; each is capable of providing ±30 A of drive current with a 35 ns rise time.

4.1.3 Gain Constants

The FONT5 board outputs a coupled loop correction with the output of each DAC (ζ_1 and ζ_2) being formed from a linear combination of the raw P2 and P3 positions ($\frac{\Delta}{\Sigma}_{P2}$ and $\frac{\Delta}{\Sigma}_{P3}$). This can be written in matrix form as

$$\begin{pmatrix} \zeta_1 \\ \zeta_2 \end{pmatrix} = \begin{pmatrix} G_{K1P2} & G_{K1P3} \\ G_{K2P2} & G_{K2P3} \end{pmatrix} \begin{pmatrix} \frac{\Delta}{\Sigma}_{P2} \\ \frac{\Delta}{\Sigma}_{P3} \end{pmatrix} \tag{4.1}$$

where $\underline{\underline{G}}$ is the gain matrix. The effects of a DAC output on the vertical beam position at P2 and P3 can be described in terms of a matrix of the kicker constants $\underline{\underline{k}}$ (described in Section 4.1.4) and will be given by

$$\begin{pmatrix} \frac{\Delta}{\Sigma}'_{P2} \\ \frac{\Delta}{\Sigma}'_{P3} \end{pmatrix} = \begin{pmatrix} k_{K1P2} & k_{K2P2} \\ k_{K1P3} & k_{K2P3} \end{pmatrix} \begin{pmatrix} \zeta_1 \\ \zeta_2 \end{pmatrix} \tag{4.2}$$

This can be re-written and substituted into Equation 4.1 to give

$$\underline{\underline{k}}^{-1} \begin{pmatrix} \frac{\Delta}{\Sigma}'_{P2} \\ \frac{\Delta}{\Sigma}'_{P3} \end{pmatrix} = \underline{\underline{G}} \begin{pmatrix} \frac{\Delta}{\Sigma}_{P2} \\ \frac{\Delta}{\Sigma}_{P3} \end{pmatrix} \tag{4.3}$$

For the feedback to reduce the jitter at both BPMs $-\frac{\Delta}{\Sigma}'_{P2} = \frac{\Delta}{\Sigma}_{P2}$ and $-\frac{\Delta}{\Sigma}'_{P3} = \frac{\Delta}{\Sigma}_{P3}$ and so by inspection

$$\underline{\underline{G}} = -\underline{\underline{k}}^{-1} \tag{4.4}$$

This gives gain constants of

Kicker-BPM Pair	k ($\frac{\Delta}{\Sigma}/\zeta$)	G ($\zeta/\frac{\Delta}{\Sigma}$)
K1-P2	13.2 ± 0.2	-8200 ± 10
K1-P3	4.3 ± 0.2	1800 ± 100
K2-P2	4.3 ± 0.2	1800 ± 100
K2-P3	19.2 ± 0.2	-5600 ± 100

Table 4.3: Kicker and gain constants for the upstream system. The errors represent the statistical uncertainty on the results.

$$G_{K1P2} = -\frac{k_{k2P3}}{|\underline{\underline{k}}|} \tag{4.5a}$$

$$G_{K1P3} = \frac{k_{k1P3}}{|\underline{\underline{k}}|} \tag{4.5b}$$

$$G_{K2P2} = \frac{k_{k2P2}}{|\underline{\underline{k}}|} \tag{4.5c}$$

$$G_{K2P3} = -\frac{k_{k1P2}}{|\underline{\underline{k}}|} \tag{4.5d}$$

4.1.4 Kicker Calibration

To calculate the gains required for upstream feedback a measure of the beam deflection at a given BPM produced by an output from each DAC was needed. The FONT5 DAQ contains the functionality to output a fixed correction signal from either of its DACs. The magnitude of each DAC was set to a range of outputs and Δ/Σ was recorded at each setting (Figure 4.3). The linear fits applied to each data set give a measure of the beam deflection of both kickers at both BPMs - they are presented in Table 4.3 along with a set of gain constants derived from them using Equation 4.5.

Considering the matrix of calibration constants the on-diagonal elements corresponding to K1-P2 and K2-P3 are larger than the off-diagonal elements. This is a manifestation of the relationship between the two kickers and BPMs. K1 is closer to 90° out of phase with P2 than P3, and so will have a greater effect at P2, this is represented by a larger K1-P2 gain constant; K2 is closer to 90° out of phase with P3 then P2 and so the K2-P3 gain constant is larger.

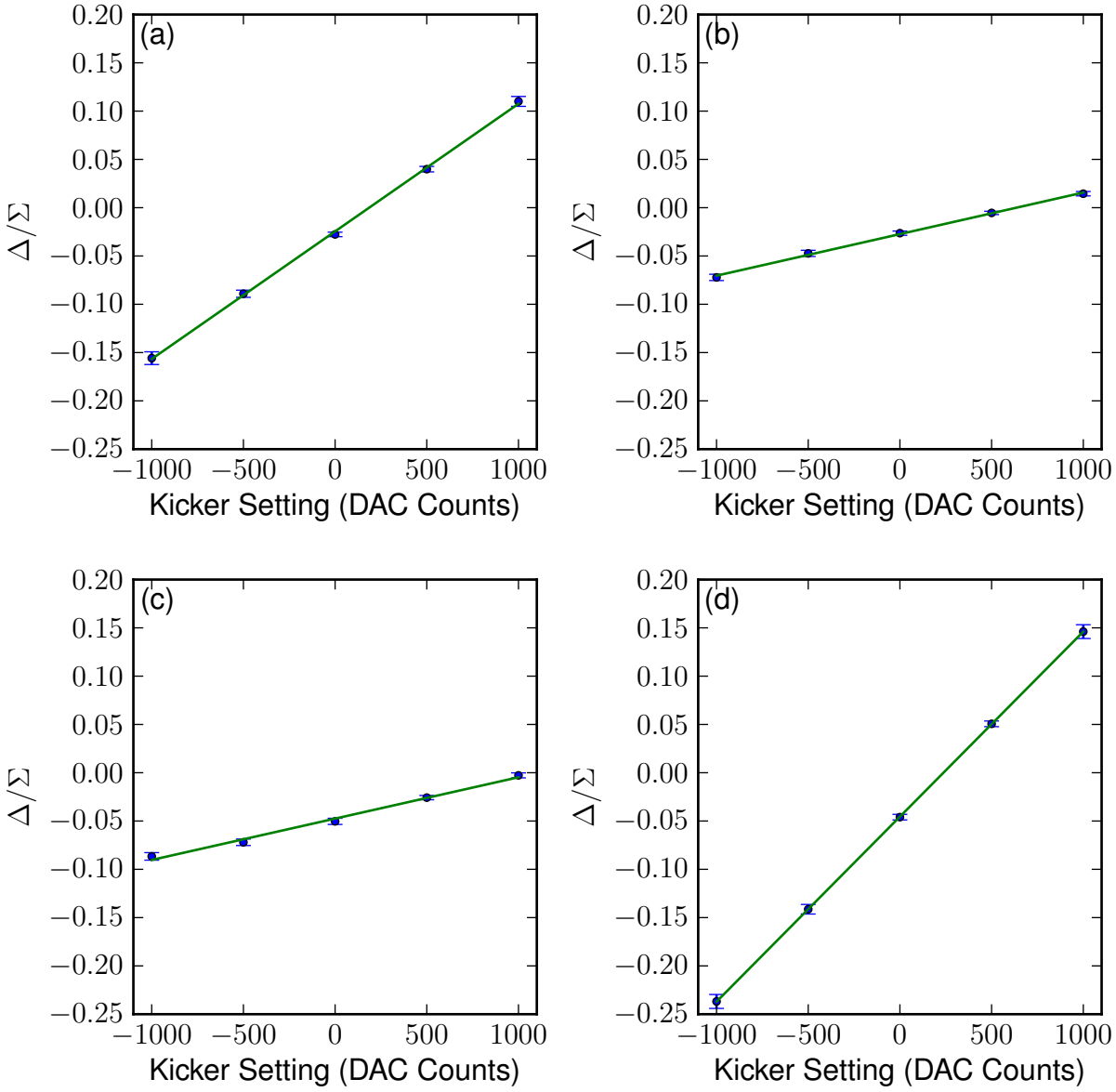

Figure 4.3: $\frac{\Delta}{\Sigma}$ vs. DAC setting for the (a) K1-P2, (b) K1-P3, (c) K2-P2 and (d) K2-P3 loops for an upstream kicker calibration. The error bars represent the statistical error on each point. The green lines represent linear fits applied to the data.

4.1.5 Interleaved Mode

During the beam tests the feedback system can be operated in an interleaved mode. Here the feedback correction is switched on and off on alternate triggers and so the correction is applied to alternate trains. This mode of operation has been used in most of the experiments presented in the following chapters.

When interleaved mode is applied, the properties of bunches with and without correction can be measured and directly compared. This method means the two initial distributions used to compare the feedback performance are in principle statistically identical.

4.2 Effects of the Kickers Measured Downstream

Kicker scans were taken and the beam position was measured downstream using the cavity BPM system. The average beam position vs. distance from P3 down the beam-line is shown in Figure 4.4.

The effect of each kicker is clearly visible. The beam displacement grows at the entrance to the final focus system, at around 20 m. The end of the final focus system is located around 40 m, here the displacement shrinks as the final doublet quadrupoles act to focus the beam to a point. Although the distributions appear asymmetric this not the case: the beam orbit with zero kick (magenta) is not flat throughout the beam-line, the displacement caused by the kicker is therefore symmetric about this nominal orbit.

4.3 Feedback Results

Beam tests were undertaken to investigate whether the correction to the vertical beam position made by the feedback system propagated downstream to the IP area. The upstream feedback system was set up; kicker scans were undertaken to calculate the gain constants and the position of the first bunch in each train was centred in P2 and P3 using the BPM mover system.

The IP BPMs were setup and calibrated in the manner described in Chapter 3. A low gain second stage was used to instrument IPA and the variable attenuator was set to introduce 10 dB of attenuation between the BPM output and the first stage down-mixer. At IPB a high gain second stage was used and no attenuation was inserted between the BPM and the first stage down-mixer. The current in QD0FF was set to place the beam waist near IPB and the vertical position of QD0FF was adjusted to position both bunches within the dynamic range of IPB. The feedback was activated and interleaved feedback runs were recorded. The vertical beam position was measured in P1, P2, P3, IPA and IPB. Distributions of the vertical beam positions are shown in Figure 4.5. The average vertical beam positions are given in Table 4.4; the vertical beam jitters are given in Table 4.5.

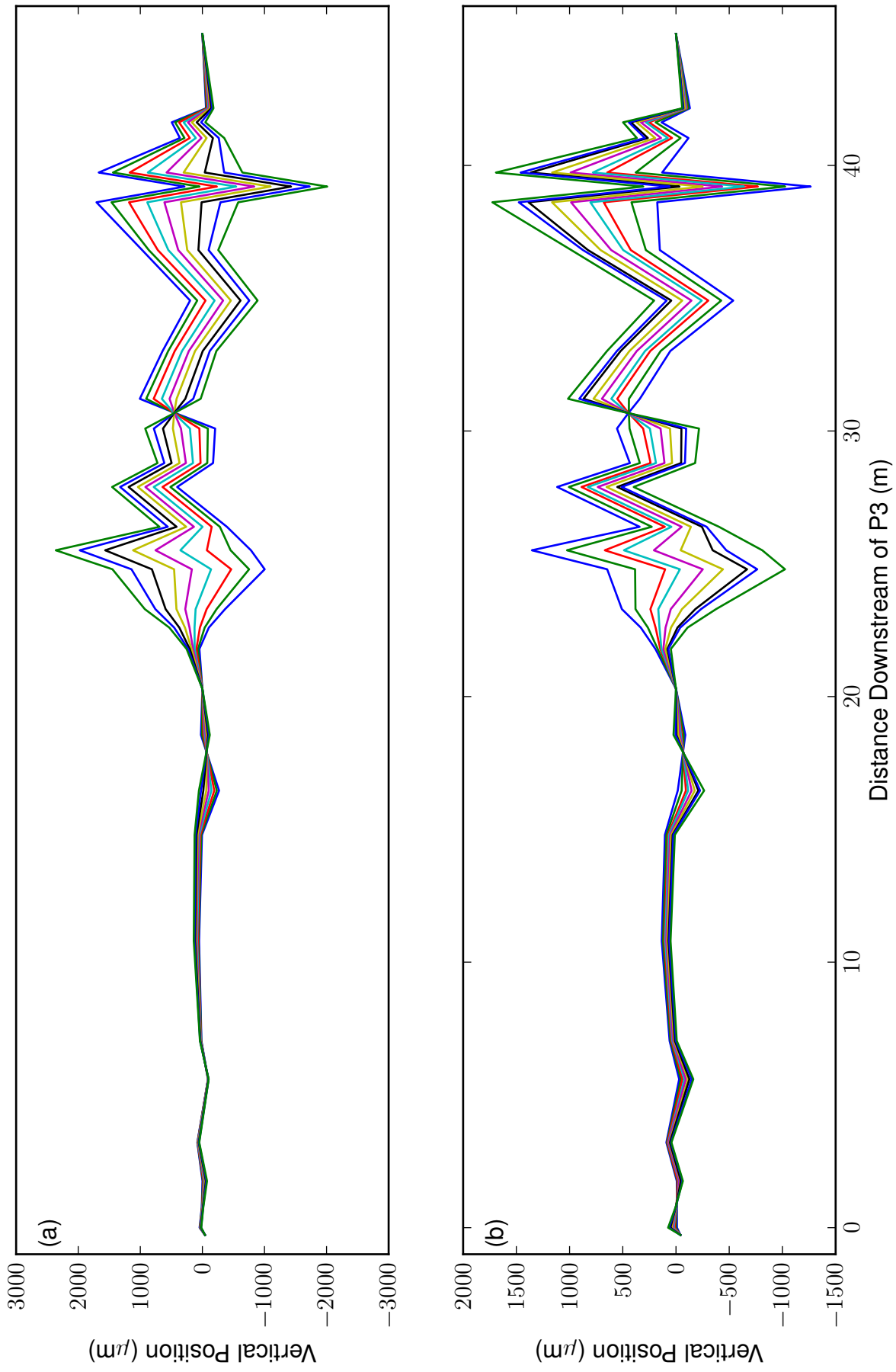

Figure 4.4: Vertical beam position vs. distance downstream of P3 for a range of (a) K1 and (b) K2 kicker settings between a DAC setting of −400 (blue) and +400 (chartreuse) in steps of 100 DAC counts.

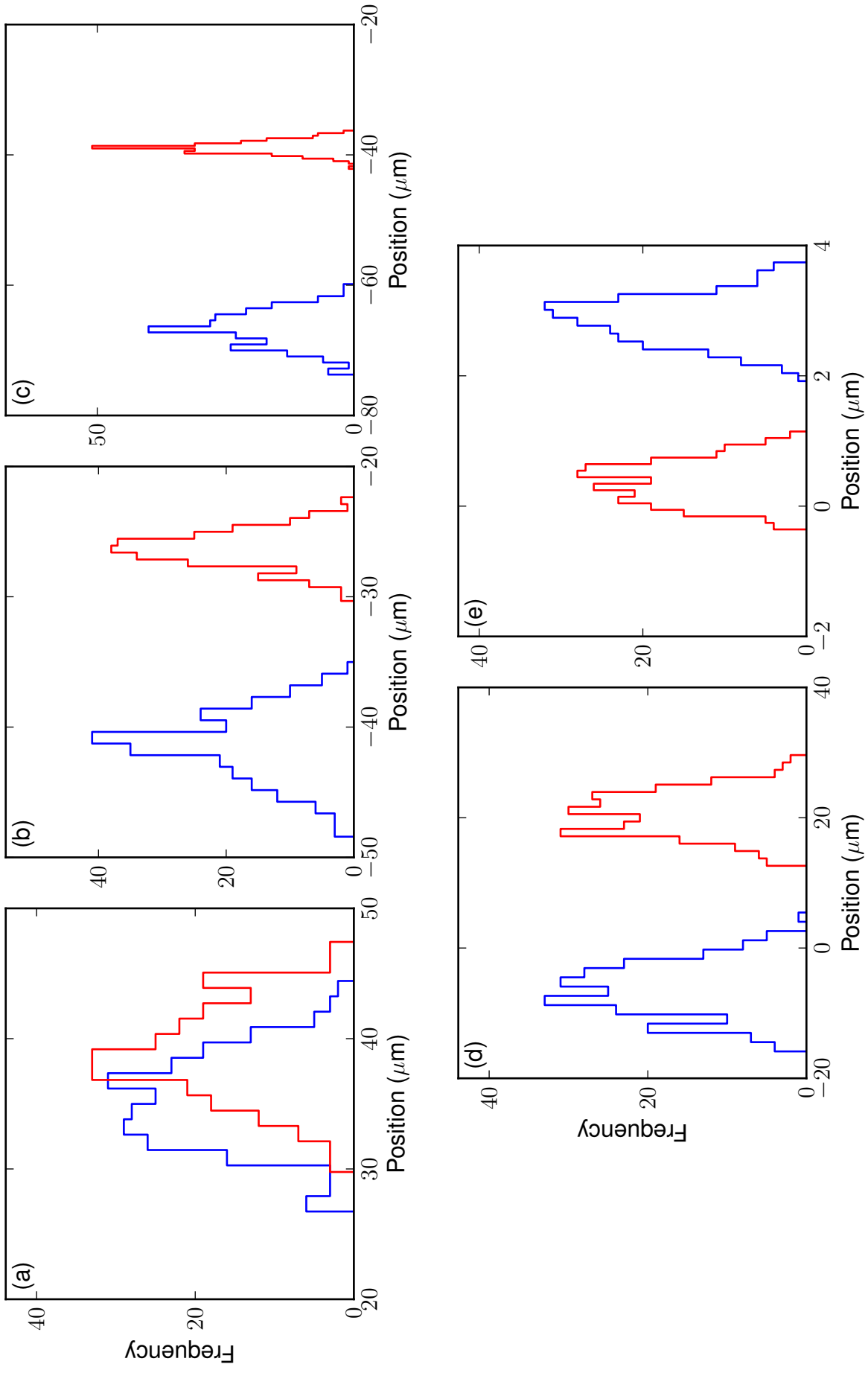

Figure 4.5: Distribution of vertical beam position of bunch two at (a) P1, (b) P2, (c) P3, (d) IPA and (e) IPB without (blue) and with (red) upstream feedback correction.

	Feedback Off (μm)	Feedback On (μm)
P1 Bunch 1	-3.6 ± 0.2	-3.4 ± 0.2
P1 Bunch 2	-35.3 ± 0.2	-38.9 ± 0.2
P2 Bunch 1	-7.3 ± 0.2	-7.5 ± 0.2
P2 Bunch 2	-41.4 ± 0.2	-26.4 ± 0.1
P3 Bunch 1	-11.0 ± 0.2	-11.3 ± 0.2
P3 Bunch 2	-66.7 ± 0.2	-38.9 ± 0.1
IPA Bunch 1	$6.6 \pm 0.3 \pm 0.03$	$6.8 \pm 0.2 \pm 0.03$
IPA Bunch 2	$-6.4 \pm 0.3 \pm 0.03$	$20.6 \pm 0.2 \pm 0.07$
IPB Bunch 1	$-1.90 \pm 0.03 \pm 0.03$	$-1.92 \pm 0.03 \pm 0.03$
IPB Bunch 2	$2.86 \pm 0.03 \pm 0.03$	$0.36 \pm 0.02 \pm 0.01$

Table 4.4: Average vertical beam position for an interleaved feedback run. These results were obtained using a bunch offset correction. The error on the position in the upstream BPMs represents the statistical uncertainty on the results. The first error on the position in the cavity BPMs represents the statistical uncertainty on the results; the second error represents the systematic uncertainty on the results.

The first and second bunch orbits throughout the ATF extraction line are not identical. The feedback has the capability to output a constant offset in addition to the feedback correction. This is referred to as the bunch offset correction and is discussed in greater detail in [21]. This can be used to align the first and second bunches at a given BPM. The bunch offset correction was adjusted to centre both bunches at IPB.

Examining Table 4.4 the feedback has little effect at P1 as it is placed directly after K1. At the two other BPMs it has the effect of moving the beam towards the zero in the two upstream BPMs but does not perfectly centre it. In the IP region the feedback does successfully centre the beam at IPB as intended, however at IPA it increases the offset of the second bunch; this is because the beam trajectory throughout the final focus was not flat when the results were taken.

The feedback reduces the vertical jitter recorded in P2, P3, IPA and IPB (Table 4.5). In the upstream region the effects are most pronounced with a factor two reduction in vertical beam jitter at P2 and a factor three reduction at P3. In the IP region the feedback reduces the jitter at both BPMs however at a much reduced level than upstream.

Figure 4.6 shows the vertical position of the second bunch vs. that of the first without and with the upstream feedback correction. The vertical bunch one to bunch two position correlations are given in Table 4.6. The feedback reduces the correlation of the first and second bunches at each BPM. The effect is most pronounced upstream and is reduced at the IP.

	Feedback Off (μm)	Feedback On (μm)
P1 Bunch 1	3.4 ± 0.2	3.4 ± 0.2
P1 Bunch 2	3.4 ± 0.2	3.6 ± 0.2
P2 Bunch 1	2.7 ± 0.1	2.5 ± 0.1
P2 Bunch 2	2.5 ± 0.1	1.4 ± 0.1
P3 Bunch 1	2.7 ± 0.1	2.5 ± 0.1
P3 Bunch 2	2.6 ± 0.1	0.92 ± 0.04
IPA Bunch 1	3.8 ± 0.2 ± 0.02	3.5 ± 0.2 ± 0.01
IPA Bunch 2	4.0 ± 0.2 ± 0.1	3.4 ± 0.2 ± 0.1
IPB Bunch 1	0.39 ± 0.01 ± 0.2	0.35 ± 0.02 ± 0.01
IPB Bunch 2	0.35 ± 0.02 ± 0.01	0.31 ± 0.01 ± 0.01

Table 4.5: Vertical beam jitter for an interleaved feedback run. The error on the position in the upstream BPMs represents the statistical uncertainty on the results. The first error on the position in the cavity BPMs represents the statistical uncertainty on the results; the second error represents the systematic uncertainty on the results.

BPM	Feedback Off(%)	Feedback On (%)
P1	77 ± 2	78 ± 2
P2	85 ± 2	1 ± 6
P3	94 ± 1	1 ± 6
IPA	92 ± 1	21 ± 6
IPB	79 ± 2	15 ± 6

Table 4.6: Bunch one to bunch two position correlation without and with the upstream feedback correction. The errors represent the statistical uncertainty on the results.

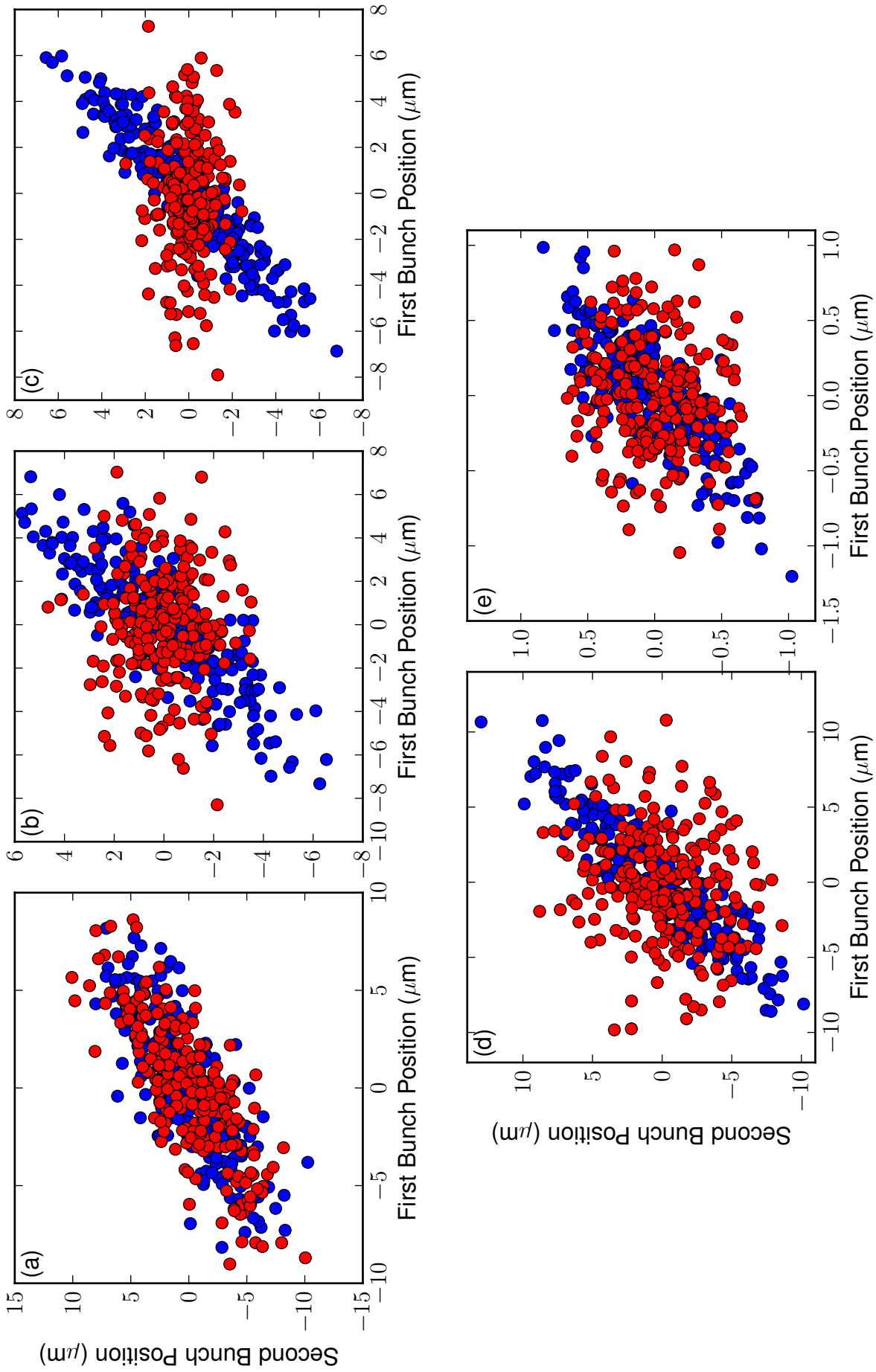

Figure 4.6: Vertical position of bunch two vs. that of bunch one at (a) P1, (b) P2, (c) P3, (d) IPA and (e) IPB without (blue) and with (red) upstream feedback correction. The offset between the two bunches has been removed.

4.4 Summary

The effectiveness of the upstream feedback system at stabilising the ATF2 beam waist has been studied. The results show that the feedback system is having an effect and improves the jitter at the IP but suggests it is hampered by the phase advance in the upstream region.

There is a free parameter in the matching routines used to setup the Twiss parameters at OTR0, in future experiments this shall be used to control the phase advance between the two upstream kickers. Experiments are currently being planned to quantitatively test the effect of the phase advance on the propagation of the correction and a simulation is being conducted in parallel to model these effects.

Chapter 5

Feedforward

During the 2012 summer recess a high speed cable was laid between the upstream experimental region and the IP. Using this cable a correction based on the beam position in the upstream system could be implemented locally at the IP using the IPK.

The effectiveness of the system operating in this 'feedforward' mode was measured using the IP BPMs.

5.1 The Feedforward Experimental Setup

Figure 1.11 shows a diagram of the feedforward system in the context of the ATF2 beamline. The feedforward system uses a linear combination of the position of the first bunch at the two upstream BPMs P2 and P3 to predict the position of the second bunch at the IP. Using the existing upstream feedback algorithm a predicted second bunch offset at the IP was calculated and a correction signal output from one of the DACs on the upstream FONT5 board. This signal was transmitted to the IP region by a half-inch Heliax[1] cable strung as close to the beamline as physical constraints would allow.

The correction signal was amplified at the IP by a FONT TMD kicker amplifier, and a stripline kicker placed downstream of QD0FF was used to deflect the beam. The effects of the local kick were measured in the IP BPMs.

5.1.1 IP BPM Setup

During the feedforward tests the IP BPMs were setup as described in Chapter 3. The beam focus was placed near IPB and the feedforward system set up to correct beam position jitter

[1] LDF4-50

at this BPM. IPB was operated with no attenuation between the BPM and the first down-mixing stage and a high-gain second stage was used. This yielded the highest achievable resolution for IPB.

With the beam waist placed near IPB during the experiments the beam position and angle jitter was large at IPA. To ensure that saturation at IPA was not an issue 10 dB of attenuation was inserted between the BPM and the input to the first stage down-mixer and a low gain second stage was used. The IP BPM signals were digitised using a local FONT5 board.

5.1.2 Feedforward Cable Latency

The distance between the upstream region and the IP is approximately 55 m. Due to physical constraints however - magnets, other experiments, support girders - the feedforward cable is longer.

A TDR unit was used to measure the transmission time of the cable, which was 263 ns. For a beam travelling at the speed of light the propagation time would be 185 ns. A signal therefore takes 78 ns longer than the beam to propagate from the upstream region to the IP. The bunch separation chosen for the experiments herein was 274 ns; considering this and subtracting the 78 ns signal propagation leaves a time window of 196 ns for the other system components. The latency of the complete system was tested and the results are reported in Section 5.3.1.

5.1.3 IPK Scan

For both IP feedback and feedforward it is crucial to have a measure of the beam deflection produced by a given DAC output of the FONT5 board. This deflection was measured using an IPK scan. The FONT5 DAQ contains the functionality to output a fixed correction signal to the IPK. Figure 5.1 shows the deflection of the second bunch by the IPK. A linear fit applied to the data yielded $k = -7.2$ nm/DAC count.

5.2 Theoretical Basis of the Feedforward Setup

The principle of feedforward is based on the idea that the beam position at any point in the lattice can be predicted using the positions at two other arbitrary points in the lattice as long as the two points are not at the same phase. It should be possible therefore to predict the position of the beam at the IP using two upstream BPMs, and stabilisation based on this prediction could be implemented. P2 and P3 are not at the same phase as one another and so are well placed to implement this idea.

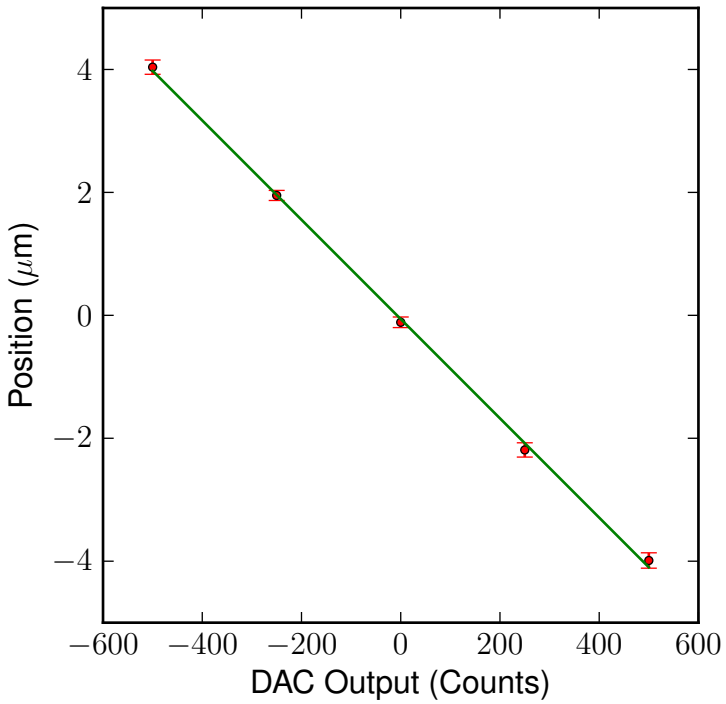

Figure 5.1: Beam position (red) vs. DAC output for an IPK scan. The green line represents a linear fit applied to the data. The error bars represent the statistical uncertainty on each point.

5.2.1 Derivation of the Feedforward Gain Constants

The algorithm used for beam stabilisation in feedforward mode has two free parameters: the P2-IPK and P3-IPK loop gain constants. These constants relate beam position in the upstream system to beam position at the IP and so contain information about the optics between the upstream region and the IP. This makes their calculation more complex than the gain constants for upstream and IP feedback.

The FONT5 board has two analogue outputs: DAC 1 and DAC 2. These were designed to be connected to K1 and K2 for upstream coupled loop feedback [21]. Each DAC takes as input a linear combination of the beam position at P2 and P3 scaled by the gains. Either can be selected to operate in feedforward mode and connected to the IPK amplifier via the feedforward cable.

Assuming that the second bunch position at the IP, $y_{IP}^{(2)}$, can be predicted from a linear combination of the first bunch positions in the upstream BPMs P2 and P3 - $y_{P2}^{(1)}$ and $y_{P3}^{(1)}$ respectively

$$y_{IP_{pred}}^{(2)} = A_2 y_{P2}^{(1)} + A_3 y_{P3}^{(1)} \tag{5.1}$$

where A_2 and A_3 are constants. These can be calculated from beam transfer matrices or from a linear fit to an appropriate data set and shall be discussed fully later. Rewriting

Equation 5.1 in terms of quantities measured in the upstream FONT system gives

$$y^{(2)}_{IP_{pred}} = A_2 c_{P2} \left(\frac{\Delta}{\Sigma}\right)^{(1)}_{P2} + A_3 c_{P3} \left(\frac{\Delta}{\Sigma}\right)^{(1)}_{P3} \tag{5.2}$$

where c_{P2} and c_{P3} are the P2 and P3 calibration constants respectively.

Consider now the deflection applied by the IPK at IPB

$$y^{(2)}_{IP_{kick}} = k\zeta \tag{5.3}$$

where k is the IPK constant described in Section 5.1.3 and ζ is the DAC output of the FONT5 board. The algorithm used in the FONT5 board to calculate the DAC output is

$$\zeta = G_{P2} \left(\frac{\Delta}{\Sigma}\right)^{(1)}_{P2} + G_{P3} \left(\frac{\Delta}{\Sigma}\right)^{(1)}_{P3} \tag{5.4}$$

where G_{P2} and G_{P3} are the gain constants to be determined.

Combining Equations 5.3 and 5.4 gives the deflection at the IP in terms of measured quantities

$$y^{(2)}_{IP_{kick}} = k \left(G_{P2} \left(\frac{\Delta}{\Sigma}\right)^{(1)}_{P2} + G_{P3} \left(\frac{\Delta}{\Sigma}\right)^{(1)}_{P3} \right) \tag{5.5}$$

The deflection at the IPK should act to cancel out the position predicted by the upstream system, i.e. $y^{(2)}_{IP_{kick}} = -y^{(2)}_{IP_{pred}}$. Hence

$$G_{P2} \left(\frac{\Delta}{\Sigma}\right)^{(1)}_{P2} + G_{P3} \left(\frac{\Delta}{\Sigma}\right)^{(1)}_{P3} = -\frac{1}{k} \left(A_2 c_{P2} \left(\frac{\Delta}{\Sigma}\right)^{(1)}_{P2} + A_3 c_{P3} \left(\frac{\Delta}{\Sigma}\right)^{(1)}_{P3} \right) \tag{5.6}$$

so by inspection

$$G_{P2} = -\frac{A_2 c_{P2}}{k} \tag{5.7}$$

and

$$G_{P3} = -\frac{A_3 c_{P3}}{k} \tag{5.8}$$

5.2.2 The Relation Constants A_2 and A_3

5.2.2.1 Determination of the Constants by Fitting

Considering Equation 5.1 and including a third free parameter B to allow for a constant arbitrary vertical position offset between the beam upstream and at the IP yields

$$y_{IP}^{(2)} = A_2 y_{P2}^{(1)} + A_3 y_{P3}^{(1)} + B \tag{5.9}$$

A long data run can be used to calculate the constants A_2, A_3 and B by fitting Equation 5.9 to $y_{IP}^{(2)}$, $y_{P2}^{(1)}$ and $y_{P3}^{(1)}$.

Fitting to a real data set has certain inherent advantages over transfer matrices: Measuring A_2, A_3 and B automatically takes into account the bunch-to-bunch correlations and higher-order magnetic effects that are not induced in the linear transfer matrices model.

5.2.2.2 Linear Transfer Matrices

Linear transfer matrices which relate the position and angle at different points in the lattice can be calculated using the theoretical models that exist for the ATF. Using these matrices it is possible to calculate how beam position at P2 and P3 translates to beam position at the IP.

Consider

$$\begin{pmatrix} y_{P3} \\ y'_{P3} \end{pmatrix} = \begin{pmatrix} m_{00}^{23} & m_{01}^{23} \\ m_{10}^{23} & m_{11}^{23} \end{pmatrix} \begin{pmatrix} y_{P2} \\ y'_{P2} \end{pmatrix} \tag{5.10}$$

and

$$\begin{pmatrix} y_{IP} \\ y'_{IP} \end{pmatrix} = \begin{pmatrix} m_{00}^{3I} & m_{01}^{3I} \\ m_{10}^{3I} & m_{11}^{3I} \end{pmatrix} \begin{pmatrix} y_{P3} \\ y'_{P3} \end{pmatrix} \tag{5.11}$$

which relate the position and angle at P2 to those at P3 and the position and angle at P3 to those at the IP where $\underline{\underline{\mathbf{M}}}^{\mathbf{23}}$ and $\underline{\underline{\mathbf{M}}}^{\mathbf{3I}}$ are the transfer matrices between P2 and P3 and P3 and the IP respectively.

Equation 5.10 yields a set of simultaneous equations relating the angle at P3 to the position at P2 and P3

Constant	Fitting Method	Transfer Matrix Method
A_2	-0.14 ± 0.02	-0.17
A_3	0.07 ± 0.02	0.10

Table 5.1: A_2 and A_3 derived using the fitted and transfer matrix calculation methods. The errors represent the statistical uncertainty on the constants.

$$y'_{P3} = \left(m_{01}^{23} - \frac{m_{11}^{23} m_{00}^{23}}{m_{01}^{23}} \right) y_{P2} + \frac{m_{11}^{23}}{m_{01}^{23}} y_{P3} \tag{5.12}$$

Considering Equation 5.11 and rearranging gives

$$A_2 = m_{01}^{3I} \left(m_{01}^{23} - \frac{m_{11}^{23} m_{00}^{23}}{m_{01}^{23}} \right) \tag{5.13}$$

and

$$A_3 = \left(m_{00}^{3I} + \frac{m_{01}^{3I} m_{12}^{23}}{m_{01}^{23}} \right) \tag{5.14}$$

The models that exist for the ATF have a large sensitivity to certain input parameters, for example the beam energy. This can result in differences between simulated and experimental parameters; in particular the model is very inaccurate at predicting the exact position of the beam waist [72]. As the constants are dependent on the exact position of the beam waist simulations have proved an ineffective method for calculating A_2 and A_3.

In practice therefore the position of the waist in the model was confirmed by comparing the simulated beam jitter at IPB with the measured beam jitter on that day. The strength of QD0FF could then be tuned in the simulation to match the simulated beam jitter (calculated as 20% of the beamsize) to the measured beam jitter ensuring the position of the waist was correct.

5.2.2.3 Comparison of the Two Methods

Table 5.1 gives examples of A_2 and A_3 calculated from fitting and from transfer matrices. For these settings the model predicts a beam jitter which agrees with that measured on the day. The predictions from the model are close to those obtained from the experimental results, it is thought that the difference is a result of a slight error in the location of the beam waist in the simulation; this arises because the beam jitter is not exactly 20% of the beamsize.

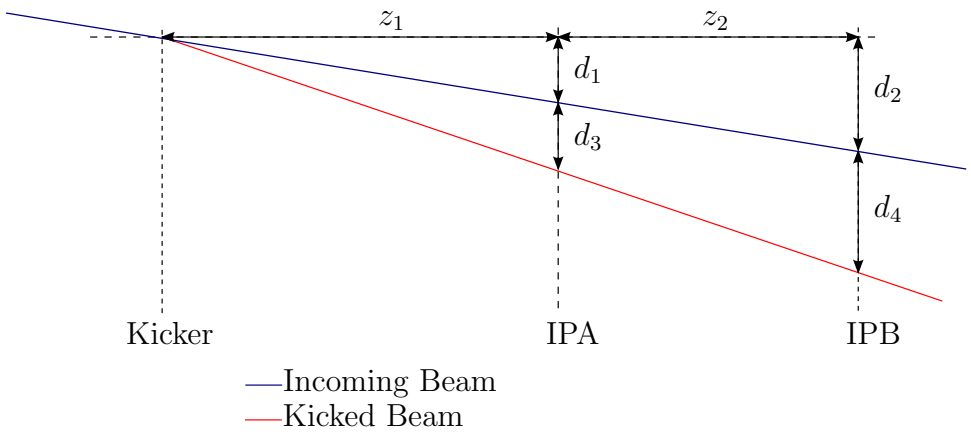

Figure 5.2: A diagram of the IP region geometry for an coming beam.

5.2.3 The Effects of the Feedforward at IPA

The effect of a kick at IPA will be less than at IPB. Examining Figure 5.2 gives

$$d_3 = \frac{z_1}{z_1 + z_2} d_4 \tag{5.15}$$

z_1 and z_2 are 0.44 m and 0.08 m respectively and so the effects of a kick at IPB will be diminished by 16% at IPA. The jitter was tuned to be in the region of 300 nm and below at IPB for the feedforward experiments. A 300 nm deflection introduced to a bunch by the IP kicker to reduce such a jitter would therefore result in a 255 nm deflection at IPA; this is below the upper limit of the resolution of IPA with 10 dB of attenuation, which is estimated using a waist scan to be approximately 500 nm. Data was recorded at IPA during the following experiments but as expected effects of the feedforward system at IPA are indistinguishable and hence no data from IPA are presented.

5.2.4 Bunch Offset Correction

As discussed in Chapter 4 the feedback algorithm has a third free parameter: the bunch offset. This is used to account for a constant position offset between the bunches one and two by introducing a constant term into the feedforward calculation. It can be calculated from B in Equation 5.9 and the kicker calibration constant. During the feedforward experiments however it was set by eye using the DAQ system; this method proved effective for these initial tests.

5.3 Feedforward Results

Multiple beam tests were undertaken at the ATF to investigate the success of the feedforward system at stabilising the beam. The performance will be evaluated in terms of: 1) the beam position; 2) the beam jitter; and 3) the bunch-to-bunch position correlation.

5.3.1 Feedforward Latency Scan

Although these experiments were performed with a long bunch spacing (274 ns) it is possible to run the ATF at shorter bunch spacings. A low latency feedforward system is important as it makes for greater flexibility in the setup of the machine.

During feedforward the arrival time of the first bunch in the upstream system is recorded in the DAQ. When this timing point is reached the FONT5 board calculates a correction and outputs the required kick signal via the feedforward chain to the IPK. The output pulse continues until long after the second bunch has passed the IPK.

Extra delay can be added to the feedforward loop by artificially shifting the first bunch arrival time in the DAQ. If enough delay is added the output kick will arrive at the IPK after the second bunch.

By gradually incrementing this parameter it is possible to discern when the combination of the latency of the feedforward components and the added delay shifts the kick until after the second bunch. Subtracting the extra delay from the bunch spacing (274 ns) gives the overall latency of the feedforward system.

Figure 5.3 shows the effect of the beam kick vs. added delay. The system was set up so the kick placed the beam near zero. At approximately 60 ns added delay the feedforward kick arrives after the second bunch; the beam then moves to its natural position without a correction near 2 μm.

From the sigmoid fit applied to the data the added delay required to reduce the kick to 90% of maximum is 72 ns. Subtracting this from the bunch spacing gives the latency of the feedforward system as 202 ns.

As discussed in Section 5.1.2 the feedforward cable latency is 78 ns. This gives a latency of the remaining components in the loop of 124 ns.

5.3.2 Feedforward Performance

The effects of the feedforward system can be demonstrated by monitoring the beam position over a data run. For clarity in such runs the strength of QD0FF was adjusted to create a beam jitter at IPB significantly larger than its resolution. QD0FF was moved to position the first bunch vertically in the centre of IPB as closely as possible. A long data run without feedforward, and an IPK scan, were taken to calculate the feedforward gain constants.

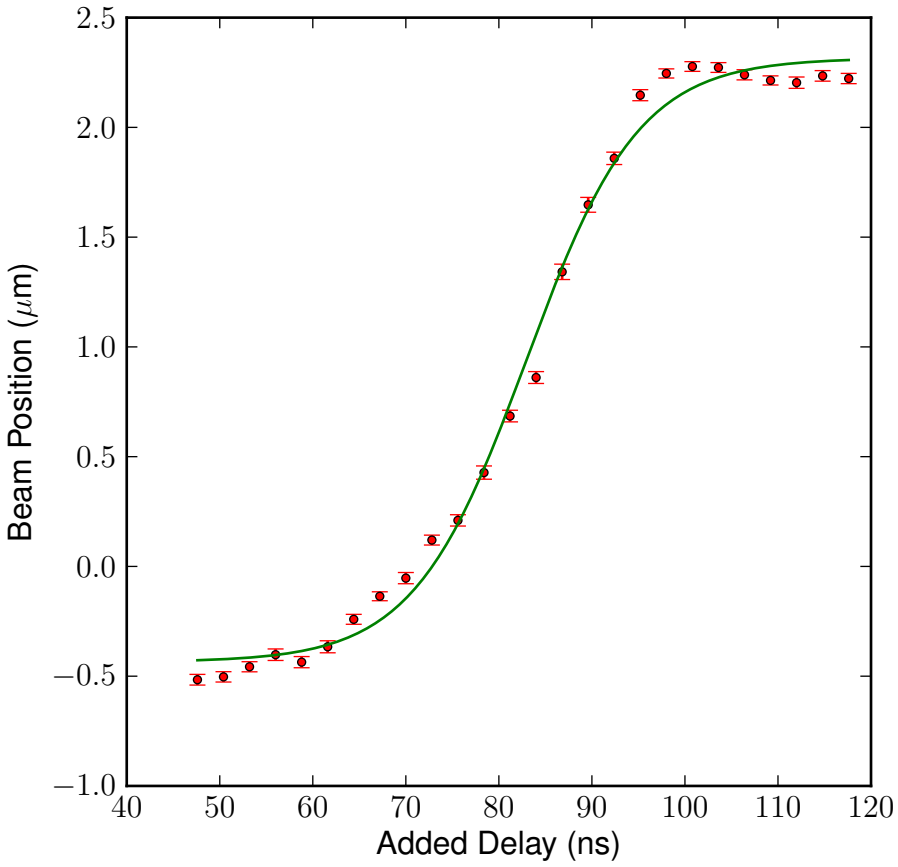

Figure 5.3: Vertical beam position at IPB (red) vs. added delay. The green line represents a sigmoid fit applied to the data. The error bars represent the statistical uncertainty on each point.

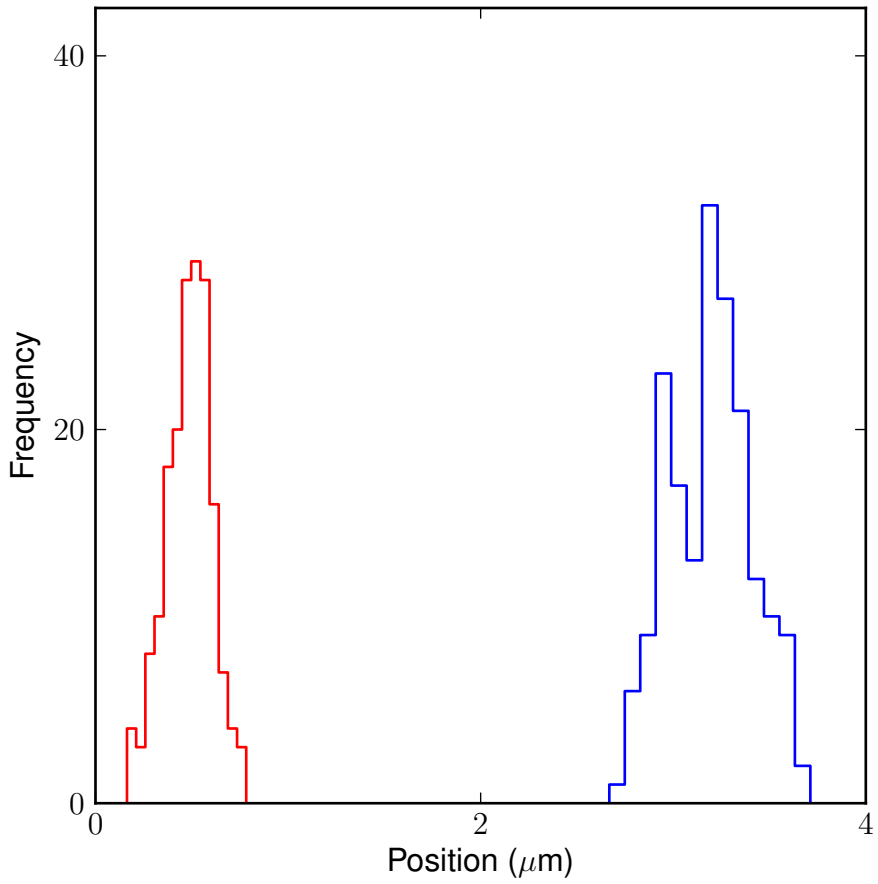

Figure 5.4: Distribution of vertical beam position at IPB with feedforward off (blue) and on (red).

Finally the bunch offset was adjusted to centre the second bunch when the feedforward correction was applied.

A run was taken with feedforward in interleaved mode and the position recorded with the IP BPMs. An example of such a data run is shown in Figure 5.4 with the average positions and jitters of both bunches with and without feedforward correction presented in Tables 5.2 and 5.3 respectively.

The results show the feedforward behaving as expected at IPB. As the feedforward does not act on the first bunch its position remains well centred with or without a feedforward correction. Due to an inherent offset between the two bunches the second bunch is positioned at approximately 3 μm; with feedforward the second bunch is well centred. Prior to feedforward the beam jitter at IPB is in the region of 160 nm; after the correction is applied the jitter is reduced to approximately 100 nm.

Figure 5.5 shows the first bunch position at IPB plotted against the second bunch position. Distributions are shown for an interleaved feedforward run without and with the feedforward correction. The bunch one to bunch two position correlations are given in Table 5.4.

Prior to feedforward the first and second bunches are well correlated. The feedforward system acts to reduce this correlation, rotating the position distribution in Figure 5.5 and

Average Position (μm)	Feedforward Off	Feedforward On
IPB First Bunch	0.72 ± 0.01 ± 0.006	0.72 ± 0.02 ± 0.006
IPB Second Bunch	3.20 ± 0.02 ±	0.3 ± 0.01 ± 0.005

Table 5.2: Average vertical positions for an interleaved feedforward run. The first error represents the statistical uncertainty on the results; the second error represents the systematic uncertainty on the results.

Jitter (nm)	Feedforward Off	Feedforward On
IPB First Bunch	220 ± 11 ± 4	229 ± 12 ± 5
IPB Second Bunch	215 ± 11 ± 6	121 ± 6 ± 6

Table 5.3: Vertical beam position jitters for an interleaved feedforward run. The first error represents the statistical uncertainty on the results; the second error represents the systematic uncertainty on the results.

flattening it.

5.3.3 Dynamic Range of the Feedforward System

A scan was undertaken to test the efficacy of the system in keeping a constant mean beam position at the IP as the upstream beam position was varied. First under nominal conditions the feedforward system was setup; gains were calculated and the bunch offset was zeroed. The current in ZV5X, a corrector magnet in the y-plane upstream of the FONT system in the extraction line was varied introducing a constant beam offset before the feedforward system. This offset changed the position of the beam in both the upstream system and at IPB.

Data runs were taken at different corrector settings whilst the feedforward was operated so as to stabilise the second bunch. The settings for the feedforward system remained unchanged throughout the scan.

In Figure 5.6 distributions of first and second bunch position measured at IPB are plotted for a number of ZV5X settings. The mean position of each distribution is given in Table 5.5. Examining the second bunch distributions one sees the system acts to stabilise the mean position of the beam at zero.

Table 5.6 lists the jitter of the first and second bunches for each of the position distributions. The feedforward system demonstrates a reduction in the jitter of the second bunch across all the points in the scan irrespective of average beam position at IPB.

Feedforward State	Bunch to Bunch Correlation (%)
Off	87 ± 2
On	-13 ± 7

Table 5.4: Bunch one to bunch two position correlations for feedforward off and on. The error represents the statistical uncertainty on the results.

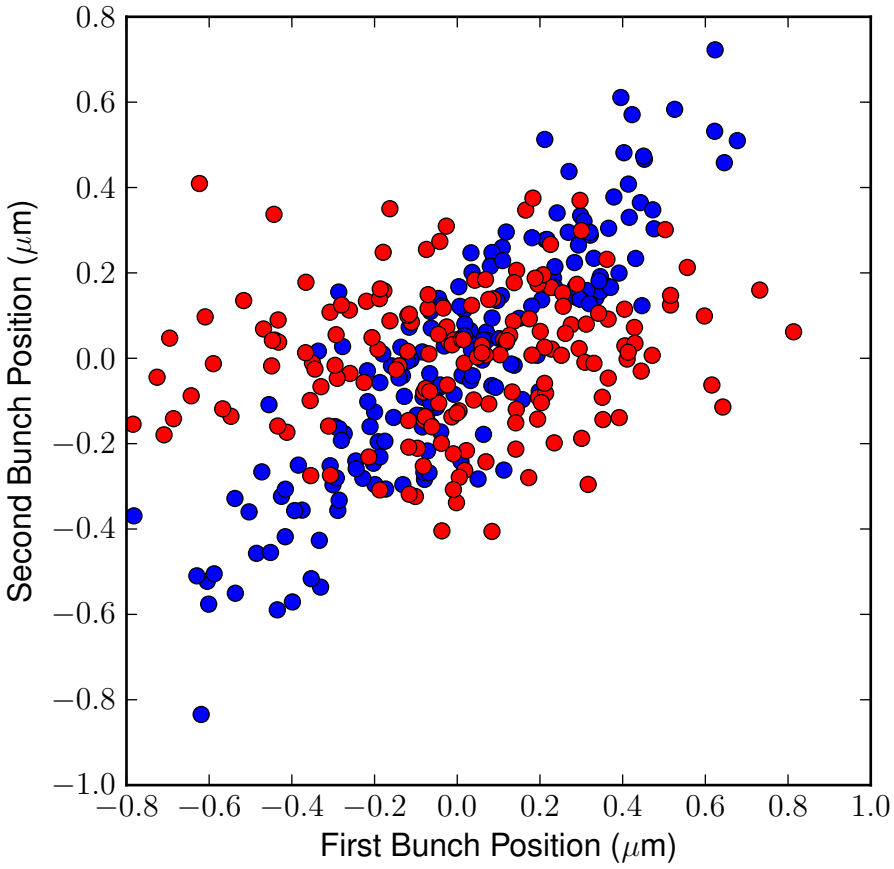

Figure 5.5: Vertical position of bunch two vs. that of bunch one without (blue) and with (red) feedforward.

ZV5X Settings (A)	First Bunch Mean Position (μm)	Second Bunch Mean Position (μm)
-0.010	4.95 ± 0.02 ± 0.04	-0.14 ± 0.01 ± 0.01
-0.005	3.92 ± 0.02 ± 0.03	-0.29 ± 0.01 ± 0.01
0.000	3.13 ± 0.02 ± 0.03	-0.13 ± 0.01 ± 0.01
0.005	1.14 ± 0.02 ± 0.01	-0.21 ± 0.01 ± 0.01
0.010	0.90 ± 0.02 ± 0.01	-0.16 ± 0.01 ± 0.01
0.015	-0.02 ± 0.02 ± 0.01	-0.10 ± 0.01 ± 0.01
0.020	-0.91 ± 0.02 ± 0.01	-0.08 ± 0.01 ± 0.01

Table 5.5: Mean vertical beam position measured at IPB for a range of ZV5X settings. The first error represents the statistical uncertainty on the results; the second error represents the systematic uncertainty on the results.

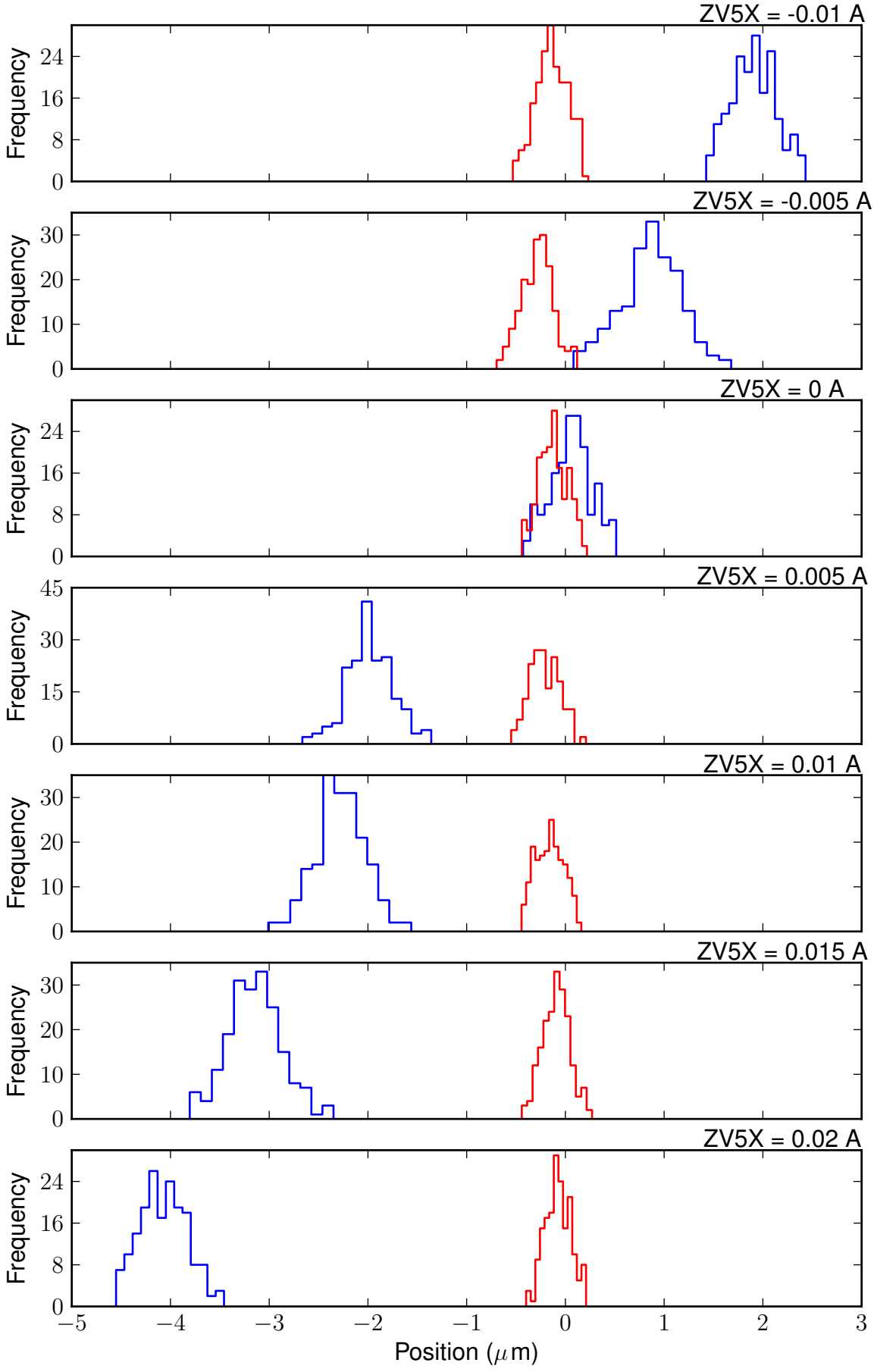

Figure 5.6: Distributions of vertical beam position for a range of ZV5X current setting for bunches one (blue) and two (red) with feedforward correction.

ZV5X Settings (A)	First Bunch Position Jitter (nm)	Second Bunch Position Jitter (nm)
-0.010	246 ± 12 ± 2	161 ± 8 ± 1
-0.005	268 ± 14 ± 3	161 ± 8 ± 1
0.000	220 ± 11 ± 2	144 ± 7 ± 1
0.005	235 ± 12 ± 2	152 ± 8 ± 1
0.010	212 ± 10 ± 2	141 ± 7 ± 1
0.015	217 ± 11 ± 3	140 ± 7 ± 1
0.020	209 ± 10 ± 2	131 ± 7 ± 1

Table 5.6: Vertical beam position jitter measured at IPB for a range of ZV5X settings. The first error represents the statistical uncertainty on the results; the second error represents the systematic uncertainty on the results.

5.3.4 Feedforward QD0FF Scan

An experiment was devised to investigate the efficacy of the feedforward system in reducing the jitter. The feedforward system should act to reduce the beam jitter to a constant level regardless of the incoming beam conditions. To investigate this hypothesis the current in QD0FF was varied to scan the waist through IPB altering the jitter at the BPM whilst other parameters were held constant and the feedforward system was operated.

5.3.4.1 QD0FF Scan with a Constant Gain

First an initial QD0FF current was selected to set the beam waist near to IPB with a jitter larger than the resolution of the BPM. The feedforward system was then set up as described in the previous sections. Interleaved feedforward runs were taken at numerous QD0FF current settings thereby moving the longtitudinal position of the waist successively from one side of IPB to the other. Altering the strength of QD0FF changes the angle and position of the beam as it passes through the final focus system. Hence the vertical position was re-centred in IPB at each current step by adjusting the vertical position of QD0FF. All other settings were kept constant.

Figure 5.7 shows the jitter recorded in IPB for such a scan. One can see that the feedforward system reduces the jitter at the first current setting in the scan, 135.7 A. As the strength of QD0FF is altered and the beam waist is moved through IPB the feedforward system correction degrades, and the jitter is worsened. As discussed in Section 5.2 the feedforward gain constants are a function of the optics between the upstream FONT region and the IP. Changing the strength of QD0FF alters the optics and therefore the required gain. Since the gain was calculated for the first point of the scan the feedforward system reduces the jitter here. As QD0FF is varied through the scan the gains are held constant, this results in incorrect gains for all other points in the scan and causes the increase in beam jitter.

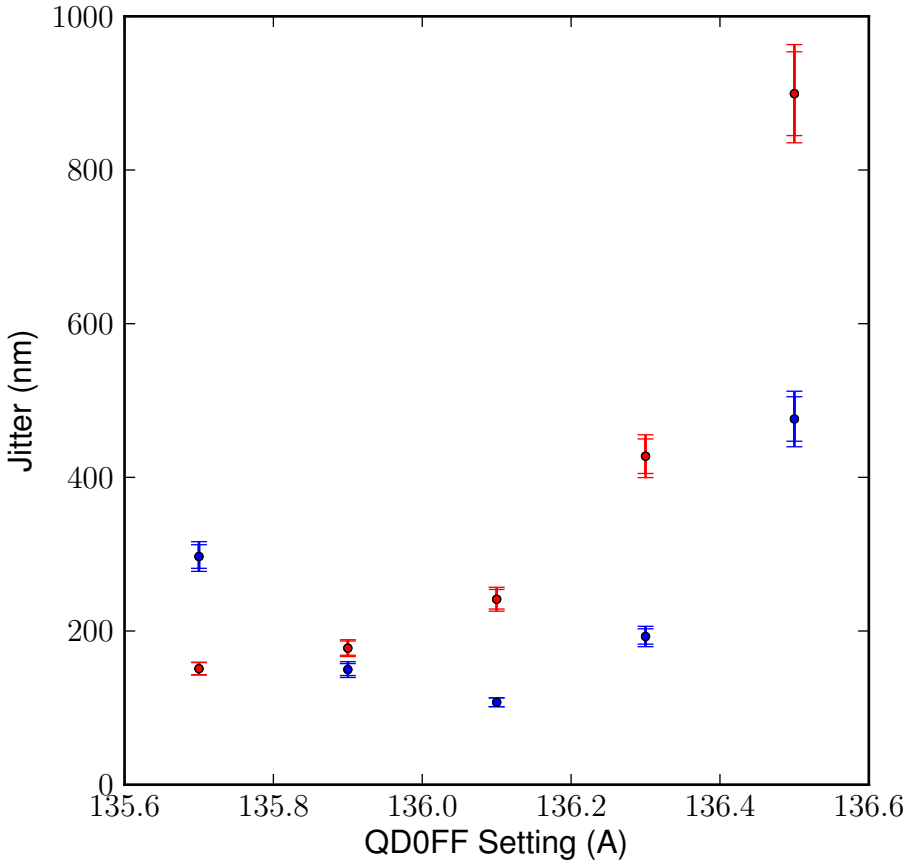

Figure 5.7: Beam jitter at IPB vs. QD0FF current without (blue) and with (red) a feedforward correction. The inner error bars represent the statistical uncertainty on each point; the outer error bars represent the total uncertainty on each point calculated as the quadrature sum of the statistical and systematic uncertainties.

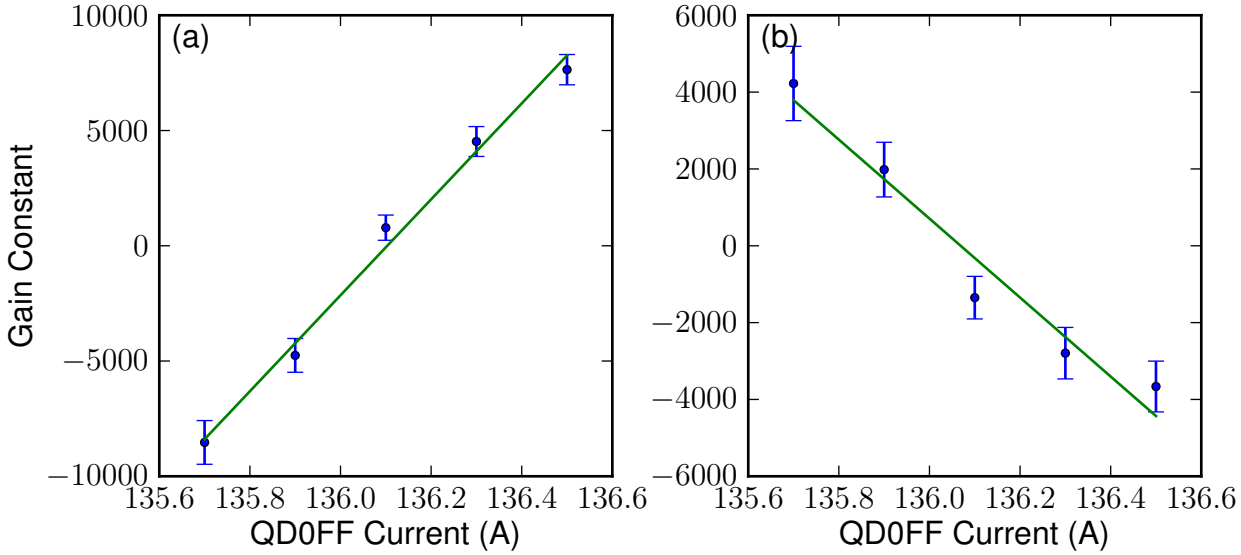

Figure 5.8: The (a) P2-IPK and (b) P3-IPK gain (blue) vs. QD0FF setting for a QD0FF feedforward scan. The green lines represents a linear fit applied to the data. The error bars represent the statistical uncertainty on each point.

5.3.4.2 Variation of the Gain Constants

The jitter at IPB scales linearly with the strength of QD0FF; the jitter as measured in the upstream system however remains constant. To reduce the jitter at IPB the gain must therefore be increased and should scale linearly with the jitter. Furthermore there is a π phase advance as the beam passes the focal point. The magnitude of the gain should therefore change in sign as the focal point moves from one side of IPB to the other.

New gains for each QD0FF setting were calculated from the data sets without a feedforward correction and are plotted in Figure 5.8. They demonstrate the expected linear relationship on QD0FF setting.

5.3.4.3 QF0FF Scan with Variable Gains

The gains calculated at each QD0FF setting were used in a second QD0FF feedforward scan. The results from the scan are shown in Figure 5.9 and the beam position jitter at each point is detailed in Table 5.7. The scan only has four QD0FF settings, five were taken however the bunch charge became unstable and the bunch-to-bunch correlation deteriorated during the run for QD0FF = 136.5 A. This point has therefore been excluded from the results.

The feedforward system reduces the beam jitter at all the QD0FF setting apart from 136.1 A. Predictions of the expected performance of the system and an explanation for the remaining dependence on incoming beam jitter after the feedforward correction are presented in the following sections.

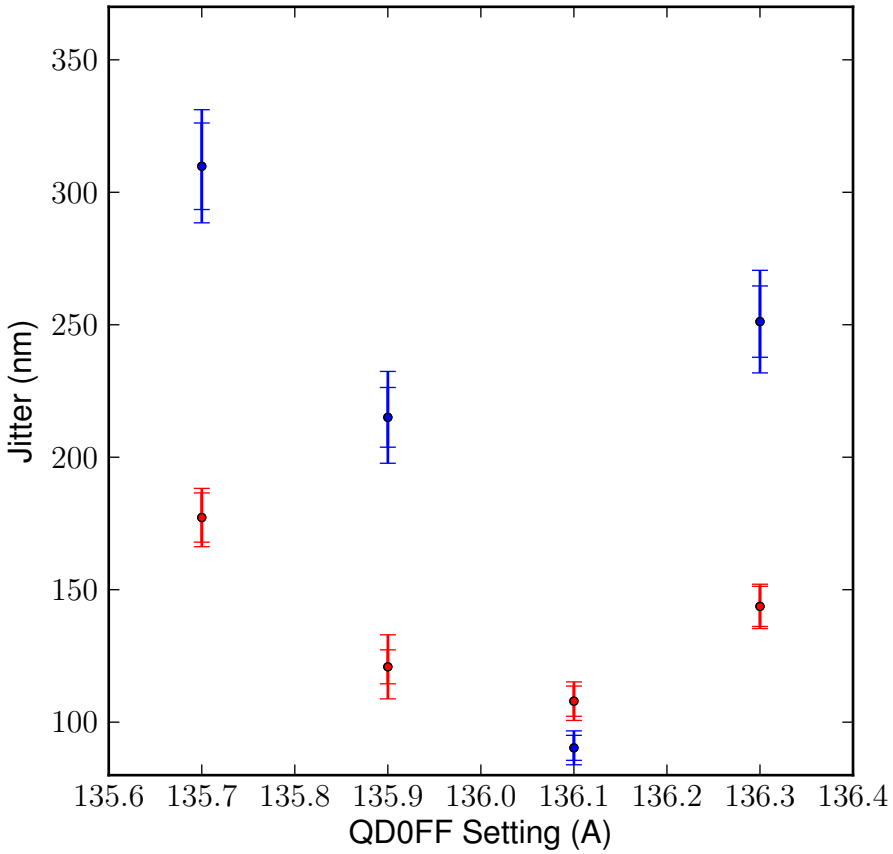

Figure 5.9: Vertical beam position jitter vs. QD0FF current for bunch two without (blue) and with (red) a feedforward correction using varying gains over a QD0FF scan. The inner error bars represent the statistical uncertainty on each point; the outer error bars represent the total uncertainty on each point.

QD0FF Settings (A)	Feedforward off Jitter (nm)	Feedforward On Jitter (nm)
135.7	$310 \pm 20 \pm 5$	$177 \pm 9 \pm 2$
135.9	$215 \pm 10 \pm 6$	$121 \pm 6 \pm 6$
136.1	$90.3 \pm 5 \pm 2$	$108 \pm 6 \pm 2$
136.3	$251 \pm 10 \pm 6$	$144 \pm 8 \pm 1$

Table 5.7: Second bunch vertical beam position jitter measured at IPB for a range of QD0FF current settings. The first error represents the statistical uncertainty on the results; the second error represents the systematic uncertainty on the results.

5.4 Modelled Performance of the Feedforward System

The results shown in Figure 5.9 show a reduction in the beam jitter however there remains a dependence on the incoming beam jitter after the feedforward correction is applied. By design the feedforward system should reduce all dependence of the corrected position on incoming beam jitter. Attempts have been made to understand this. Two frameworks are presented for predicting the level of beam jitter after the feedforward correction.

5.4.1 Expected Performance Based on the Predicted Position

The difference between the position at the IP predicted from the two upstream BPMs (y^p) and position measured at IPB (y^m) places an empirical limit on the achievable correction of the feedforward system. If every other component in the system performs perfectly and introduces no addition source of error the beam displacement after the correction (y^r) will be given by this difference

$$y^r = y^p - y^m \tag{5.16}$$

The position differences for all the triggers in the QD0FF scan have been calculated. If the RMS width of the distribution of these differences at each step in the scan is calculated it will give a prediction of the beam jitter after the feedforward correction. This is presented along with the jitters from the QD0FF scan in Figure 5.10. The results agree well with the prediction.

The prediction only includes terms derived from the measurement of the position either upstream or at the IP and the intrinsic correlation between the bunch position in the upstream and IP regions. The agreement between the prediction and the data suggests the the main contributions to the residual beam jitter are from the components related to these terms.

5.4.2 Expected Performance Based on the BPM Resolutions and Upstream Downstream Correlation

It is possible to calculate the expected performance of the feedforward system based solely on the BPM resolutions and the gain constants used in the system. This analysis also yields an explanation as to why the beam jitter is not reduced to a constant level over the feedforward QD0FF scan.

The measured position (y^m) at a BPM can be written

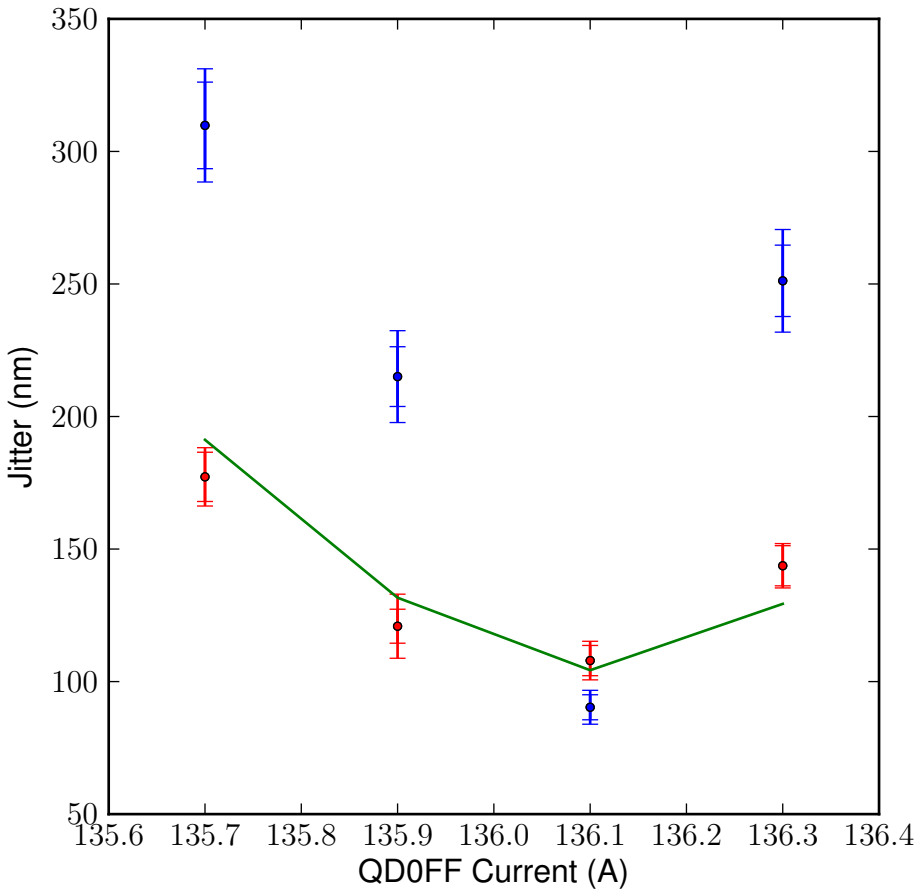

Figure 5.10: Beam jitter vs. QD0FF current without (blue) and with (red) a feedforward correction. The green line shows the predicted jitter based on position residuals. The inner error bars represent the statistical uncertainty on each point; the outer error bars represent the total uncertainty on each point.

$$y^m = y^a + \delta y \tag{5.17}$$

where y^a is the actual position and δy is the error on this measurement. The predicted position at the IP (y^p_{IP}) can then be written

$$y^p_{IP} = G_2(y^a_{P2} + \delta y_{P2}) + G_3(y^a_{P3} + \delta y_{P3}) \tag{5.18}$$

where G_2 and G_3 are the gain constants relating position at P2 and P3 to the IP.

If the other components in the feedforward system (kickers, amplifiers) do not introduce any additional sources of error then the beam position at the IP after a correction is applied is given by

$$y^r_{IP} = y^m_{IP} - y^p_{IP} \tag{5.19}$$

or in terms of Equations 5.17 and 5.18

$$y^r_{IP} = y^a_{IP} + \delta y_{IP} - G_2(y^a_{P2} + \delta y_{P2}) - G_3(y^a_{P3} + \delta y_{P3}) \tag{5.20}$$

The premise of feedforward is that position at the IP can be predicted by two other points in the lattice if the two points are not in phase with one another, written in terms of the upstream BPMs P2 and P3 as

$$y^a_{IP} = A_2 y^a_{P2} + A_3 y^a_{P3} \tag{5.21}$$

where A_2 and A_3 are the ideal constants relating position in the upstream region with the IP. The gain constants G_2 and G_3 are an experimental representation of the constants A_2 and A_3 with some experimental uncertainty. To reduce the contribution of individual measurement errors to this uncertainty the constants are calculated by fits to long data runs of many triggers. The error on each constant is therefore a representation of how well Equation 5.21 holds. If there is a poor correlation between the two systems or the two bunches then Equation 5.21 no longer holds and this will result in a poor fit and a gain constant with a large error. Equation 5.21 can be re-written in terms of the experimental gains and their errors as

$$y^a_{IP} = (G_2 + \delta G_2)y^a_{P2} + (G_3 + \delta G_3)y^a_{P3} \tag{5.22}$$

Substituting this into Equation 5.20, expanding brackets and cancelling yields

$$y^r_{IP} = \delta y_{IP} - G_2\delta y_{P2} - G_3\delta y_{P3} + \delta G_2 y^a_{P2} + \delta G_3 y^a_{P3} \tag{5.23}$$

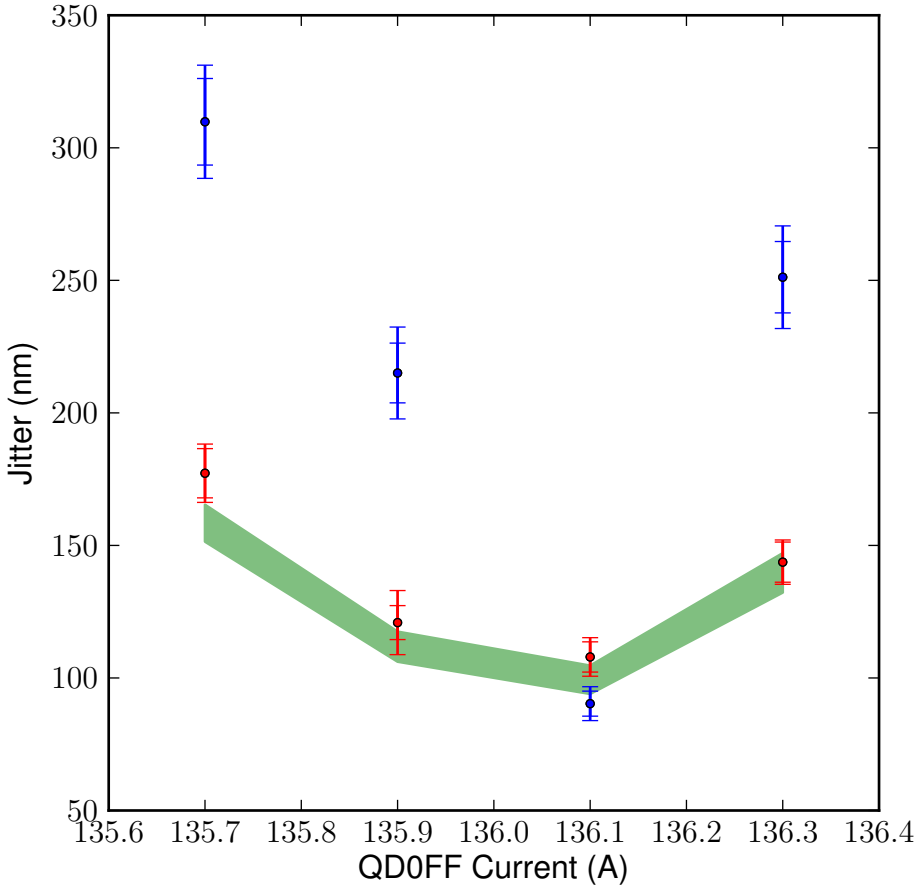

Figure 5.11: Beam jitter vs. QD0FF current for bunch two without (blue) and with (red) a feedforward correction. The green shaded area shows the lower and upper bounds of a prediction of the level of jitter after the correction based on BPM resolution and the error on the gains. The inner error bars represent the statistical uncertainty on each point; the outer error bars represent the total uncertainty on each point.

Finally, using Equation 5.17 to eliminate the actual positions in the equation gives

$$\begin{aligned} y^r_{IP} = \quad & \delta y_{IP} - G_2 \delta y_{P2} - G_3 \delta y_{P3} + \\ & \delta G_2 y^m_{P2} + \delta G_3 y^m_{P3} - \\ & \delta G_2 \delta y_{P2} - \delta G_3 \delta y_{P3} \end{aligned} \tag{5.24}$$

This equation can be thought of as containing three components: 1) terms relating to measurement errors of the position in the three BPMs used in feedforward; 2) terms relating to the errors in the gain arising from a lack of correlation between the upstream and downstream systems and 3) terms resulting in the combination of terms 1 and 2 which are negligible.

Considering the terms of this equation over many triggers: Any term relating to the beam position will yield a variation around some nominal position - the beam jitter ($\tilde{y}_{BPM}$). The components relating to the error on a position measurement will yield the average error on

the position measurement or the BPM BPM resolution (σ_{bpm}).

Each term in the equation contains one of these components all of which should be Gaussian distributed. Some of these terms also contain a component relating to a gain or an error on a gain, these act as scaling factors as they remain constant over many triggers. Equation 5.24 therefore becomes

$$\tilde{y}^r_{IP} = \sqrt{(\sigma_{IPB})^2 + (G_2\sigma_{P2})^2 + (G_3\sigma_{P3})^2 + (\delta G_2 \tilde{y}^m_{P2})^2 + (\delta G_3 \tilde{y}^m_{P3})^2} \tag{5.25}$$

This equation therefore gives a prediction for the residual beam jitter ($\tilde{y}^r_{IP}$) after the feedforward correction; this has been applied to the data from the QD0FF scan. The predicted jitter and the uncertainty on it are highly dependent on the resolution of IPB which, as setout in Chapter 3, is difficult to calculate. As presented previously the jitter with the waist at IPB has been used as a method to infer the BPM resolution at 85 $\pm$ 6 nm. This and the uncertainties on the other components in Equation 5.24 have been used to calculate an uncertainty on the predicted jitter for each step in the scan. The area between these limits is presented in Figure 5.11 along with the actual beam jitters. The measured jitter after the feedforward correction lies inside the area of the predicted performance.

This method also gives an explanation as to why the feedforward correction does not stabilise the beam jitter at a constant level. The level of beam jitter is being controlled by changes in the QD0FF magnet setting, which in turn affect the feedforward gains. The performance of the system will then vary as a larger gain will act to scale up the terms relating to the upstream BPM resolutions. This will result in a larger beam jitter after the feedforward correction is applied.

Using Equation 5.25 it is possible to analyse the contribution of each system component to the residual beam jitter. Figure 5.12 shows the contribution of different parts of the system to the feedforward jitter. At low jitters when the waist is placed close to IPB the dominant contribution to the residual jitter is the resolution of IPB. It is an important consideration that in the feedforward system IPB only acts as a witness and therefore does not affect the level of correction only the measurement of it. At QD0FF = 136.1 A there is a larger contribution from the error on the gain; at this setting the beam jitter is below the resolution limit of IPB. Attempts to fit to the upstream positions are therefore poor as the positions at IPB are swamped by Gaussian noise. At larger jitters the required gain is larger, this introduces a stronger coupling of the upstream BPM resolution into the final jitter and so these terms begin to dominate.

A final comment regards the method used to conduct this experiment. Ideally the beam jitter before the upstream system would have been varied and the lattice downstream held constant. Under these conditions the feedforward system should reduce the beam jitter to a constant level. However, a method for varying the beam jitter before the upstream system in a controlled manner proved elusive.

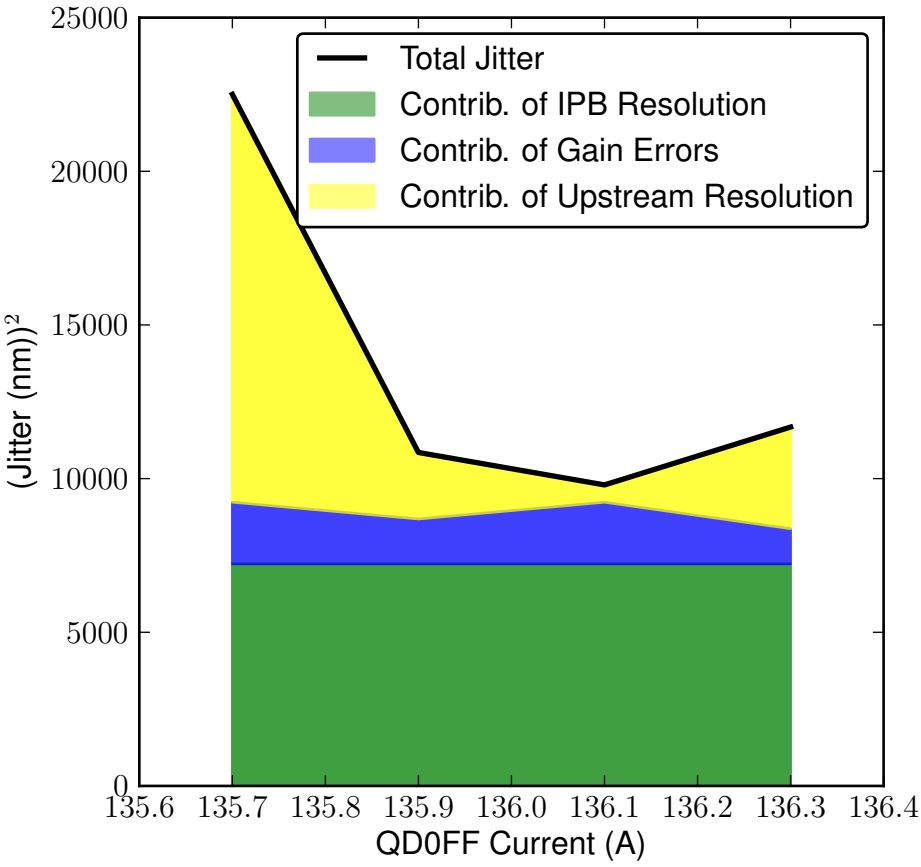

Figure 5.12: Predicted contribution to the residual beam jitter squared vs. QD0FF setting during a feedforward QD0FF scan. The legend specifies the colour used to represent each component. Jitter squared is presented as the contributions sum in quadrature.

5.5 Summary

The concepts of a system using the positions in two upstream BPMs to stabilise the beam locally at the IP have been described. A method for calculating the gains in such a system has been provided and an explanation of the effects of such a system on beam position and jitter in the context of the ATF final focus system has been presented.

Results from the first attempts at a practical implementation of such a feedforward system have been reported. The initial setup and commissioning procedures have been explained and a series of tests designed to demonstrate the feedforward system working in the manner expected have been presented. The feedforward system has produced effective reductions in beam jitter to levels of 100 nm and shown stabilisation of the mean position over an incoming beam range of 6 μm. The latency of the feedforward system was measured and found to be 202 ns.

Two frameworks for predicting the performance of the feedforward system have been developed both of which produce predictions of the residual jitter level in line with the experimental results. One framework provides a breakdown of the contributions to the residual jitter after the feedforward correction and suggests that at low jitters the main contributing factor is the resolution of IPB.

Chapter 6

IP Feedback

A third experimental system for stabilisation of the ATF IP was tested: The IP feedback system used one of the ATF IP BPMs to measure the vertical position of the focus and output a feedback correction based on this position using the IPK. The effects of the feedback were then measured using the same BPM.

The IP feedback tests had two purposes: 1) as another attempt to stabilise the ATF beam waist and 2) an attempt to use a cavity BPM system to provide beam based position feedback within a bunch train. The system presented is believed to be the first successful attempt to use a cavity BPM for single pass intra-train feedback worldwide.

6.1 IP Feedback Experimental Setup

A block diagram of the IP feedback system is shown in Figure 6.1. It measures the position of the first bunch at IPB and uses this to calculate a feedback correction aimed at stabilising the position of the second bunch at IPB. The system utilises the components used for upstream feedback adapted for the IP. In place of the upstream stripline BPM processor described in Chapter 2 the homodyne cavity BPM electronics are used to process the signals from the IP BPMs and provide an analogue position signal on which to feed back.

The biggest difficulty in adapting the upstream system for use at the IP arises from the design of the firmware run on the FONT5 board. Until now all experiments described at the IP have used the FONT5 board as a digitiser: the raw waveforms were digitised and transmitted to the FONT DAQ where they were recorded; the signals were then processed into position data offline. For IP feedback the processing of the cavity BPM signals must be done using digital logic on the FONT5 board. The position must be calculated in real time so it can be used to calculate a correction signal for the second bunch.

The feedback firmware takes as input a linear combination of the Δ/Σ signals from P2 and

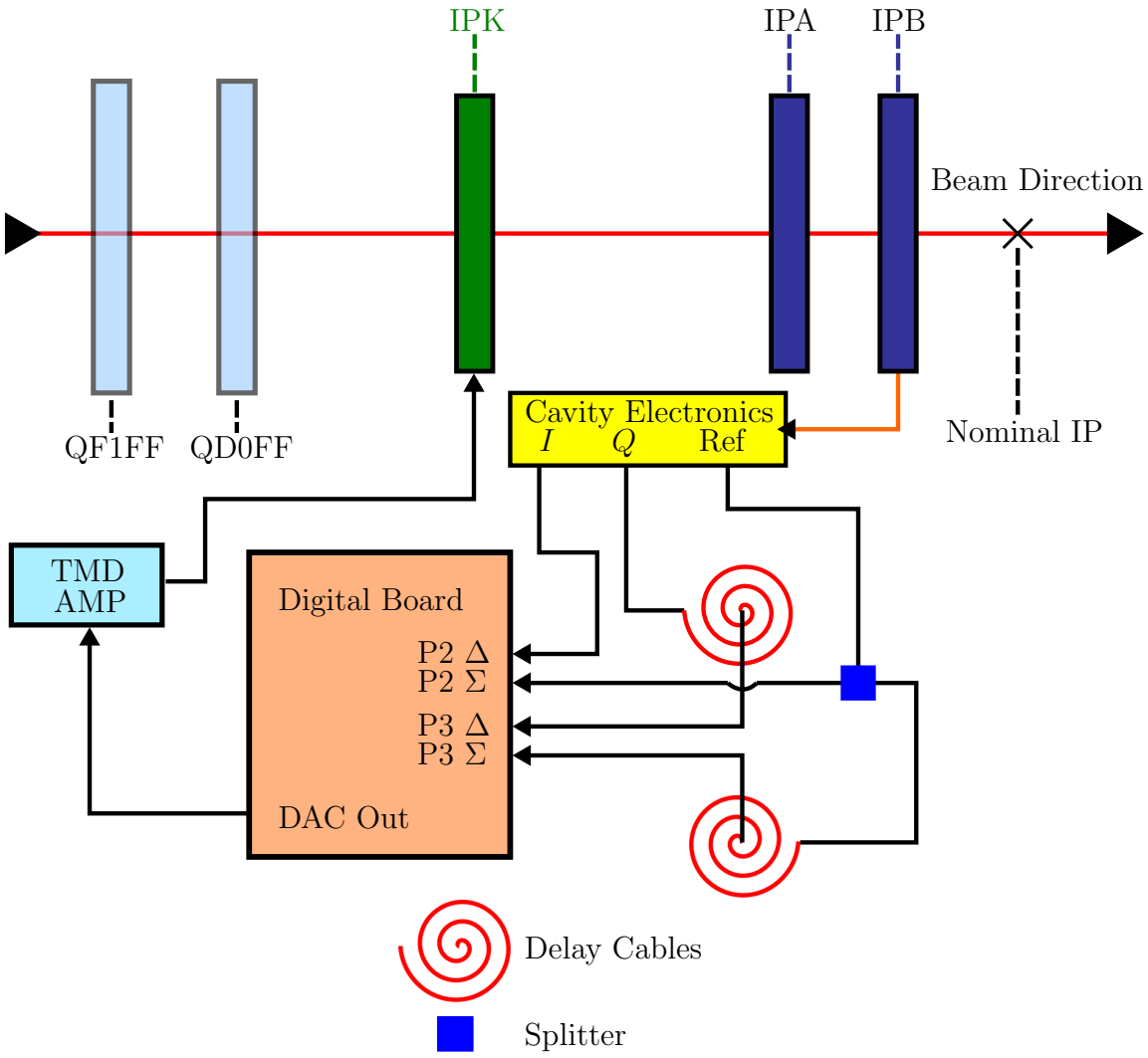

Figure 6.1: Block diagram of the IP feedback setup showing the FONT5 board; the cavity BPM electronics (simplified); the TMD amplifier; the final doublet magnets; the IPK; and the two cavity BPMs IPA and IPB.

P3 to calculate a correction. The weighting of the combination is adjusted by the gains (G_2 and G_3) used to scale the signals to give an output - ζ - in DAC counts of

$$\zeta = G_{P2}\left(\frac{\Delta}{\Sigma}\right)_{P2} + G_{P3}\left(\frac{\Delta}{\Sigma}\right)_{P3} \tag{6.1}$$

This is algebraically similar in form to the equation used to calculate position at a cavity BPM:

$$y = s_p \cos\theta \frac{I}{q} + s_p \sin\theta \frac{Q}{q} \tag{6.2}$$

where s_p is the scale factor for converting charge normalised I' to microns and q is the diode bunch charge signal.

As shown in Figure 6.1 for IP feedback the P2 and P3 Δ channels were used to digitise the I and Q signals. The diode charge signal was split using a 3 dB power splitter to provide identical inputs to the P2 and P3 Σ channels for charge normalisation.

6.1.1 Derivation of the IP Feedback Constants

The output of the feedback algorithm in DAC counts with the board set up in this manner was

$$\zeta = G_I \frac{I}{q} + G_Q \frac{Q}{q} \tag{6.3}$$

Where G_I and G_Q were the gain constants used for the I and Q channels. The IPK will amplify a DAC signal scaled by the IPK constant k to produce a deflection at IPB in terms of I, Q and q as

$$y_{kick} = k(G_I \frac{I}{q} + G_Q \frac{Q}{q}) \tag{6.4}$$

The DAC output should act to produce a deflection at the IPK of opposite sign to the measured beam displacement at IPB

$$y_{kick} = -y_{meas} \tag{6.5}$$

Using this; combining Equations 6.2 and 6.4 and rearranging gives

$$G_I = \frac{s_p \cos\theta}{k} \tag{6.6}$$

and

$$G_Q = \frac{s_p \sin\theta}{k} \tag{6.7}$$

The I-Q rotation is thereby achieved by including θ in the I and Q gain constants to rotate and scale simultaneously.

6.1.2 Practical Implementation of the IP Feedback Setup

There were some practical difficulties in the implementation of the IP feedback setup caused by features in the firmware concerning specific parameters; in particular there are several constraints regarding the arrival time of specific signals. These constraints arise due to certain assumptions about the geometry and apparatus of the upstream system that do not hold at the IP.

It is a requirement that the P3 Σ and Δ signals are sampled at least five sample points after the P2 signals. This aids latency constraints in the feedback calculation [21] and was acceptable because P2 is several meters upstream of P3. In the down-mixing electronics the I and Q signals are output simultaneously and as the I-Q rotation angle is a function of time must be sampled at the same point.

The solution to this problem was to make two cables one of which was five sample points, i.e. 14 ns, longer than the other. These cables were then used to connect the homodyne electronics to the FONT5 board with the longer cable used to connect the Q channel. This delayed the arrival of the Q signal until five samples after the I signal enabling simultaneous sampling in time but effectively five sample points apart on the digital board.

A further difficulty was that the sample point was constrained to be identical across each Σ and Δ pair. Further delay cables were therefore fabricated to synchronise the arrival time of the signals at the FONT5 board.

6.1.3 Setup of the IP Feedback System

A standard procedure was devised to set up the IP feedback system: 1) An IPK scan was taken to calculate the gains for IP feedback. 2) The position of the first bunch was centred at IPB using QD0FF. 3) The upstream system was used to align the trajectory of the second bunch with respect to the first. 4) The feedback was activated.

6.2 Expected Performance of IP Feedback System

A model based on the bunch to bunch correlations and the resolution of IPB was developed for the IP feedback system. The model's aims were to predict the residual beam jitter after the feedback correction given the incoming beam conditions and the gain used in the feedback loop.

6.2.1 With Nominal Gain

The IP feedback system predicts the position of the second bunch by assuming it is identical to that of the first. The beam displacement at IPB (y^r) after the feedback correction will therefore be

$$y^r = y_2^a - y_1^a + \delta y_2 - \delta y_1 \tag{6.8}$$

where y_1^a and y_2^a are the actual positions of the first and second bunches without feedback and δy_1 and δy_2 are the respective errors on these measurements. Writing $y_2^a - y_1^a$ as the position difference between the bunches (Δy_{12}^a) and considering this over many triggers the beam jitter after a correction ($\tilde{y}^r$) will be given by

$$(\tilde{y}^r)^2 = \langle \Delta y_{12}^a \rangle^2 + \langle \delta y_2 \rangle^2 + \langle \delta y_1 \rangle^2 \tag{6.9}$$

Hence

$$(\tilde{y}^r)^2 = (\tilde{y}_1^a)^2 + (\tilde{y}_2^a)^2 - 2\tilde{y}_1^a \tilde{y}_2^a \rho_{y_1^a y_2^a} + 2\sigma_y^2 \tag{6.10}$$

where $\tilde{y}_i$ is the jitter of the i^{th} bunch; $\rho_{y_1^a y_2^a}$ is the correlation between the position of the two bunches; and σ_y is the resolution of IPB. If both bunches have equal jitter and are perfectly correlated, $\rho_{y_1^a y_2^a} = 1$:

$$\tilde{y}^r = \sqrt{2}\sigma_y \tag{6.11}$$

placing a theoretical limit on the performance of the IP feedback system as $\sqrt{2}$ times the resolution of IPB.

In practice we measure the position hence

$$(\tilde{y}^r)^2 = (\tilde{y}_1^m)^2 + (\tilde{y}_2^m)^2 - 2\tilde{y}_1^m \tilde{y}_2^m \rho_{y_1^m y_2^m} \tag{6.12}$$

6.2.2 With Fractional Gain

When the bunch to bunch correlation is below 100% the level of jitter reduction can be improved by scaling the gain. The position of the second bunch is then assumed to be that of the first bunch scaled by a factor j

$$y_2^m = jy_1^m \tag{6.13}$$

The residual position difference is therefore

$$y^r = y_2^m - jy_1^m \tag{6.14}$$

and the jitter is

$$(\tilde{y}^r)^2 = (\tilde{y}_1^m)^2 + j^2(\tilde{y}_2^m)^2 - 2j\tilde{y}_1^m\tilde{y}_2^m\rho_{y_1^m y_2^m} \tag{6.15}$$

Differentiating Equation 6.15 with respect to j gives

$$\frac{d(\tilde{y}^r)^2}{dj} = 2j(\tilde{y}_2^m)^2 - 2\tilde{y}_1^m\tilde{y}_2^m\rho_{y_1^m y_2^m} \tag{6.16}$$

which yields a minimum jitter at

$$j = \rho_{y_1^m y_2^m} \tag{6.17}$$

if the jitter of the first bunch is equal to that of the second. This was the case during the IP feedback experiments as is demonstrated in the following sections (Table 6.3).

6.3 IP Feedback Results

The performance of the IP feedback system was studied.

6.3.1 IP Feedback Latency Scan

The latency of the IP feedback system was tested using the method described in Section 5.3.1. Figure 6.2 shows the results from the scan with a sigmoid fit applied to the data. From the fit the delay required to reduce the kick to 90% is 62 ns. Subtracting this from the bunch spacing of 274 ns gives the latency of the IP feedback system as 212 ns.

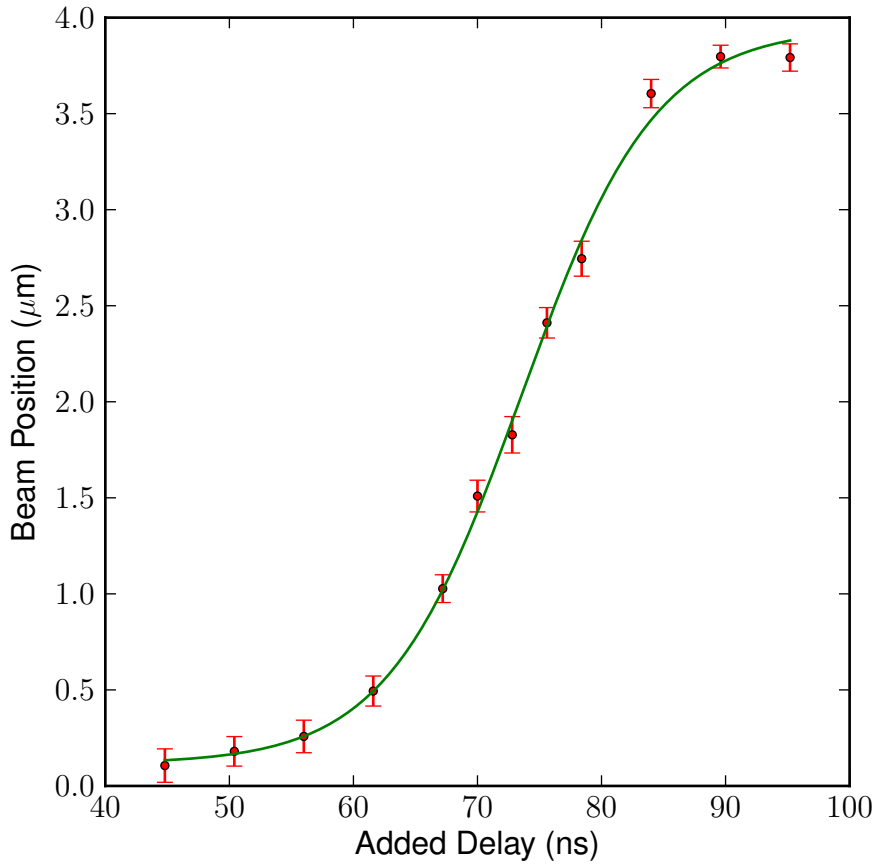

Figure 6.2: Vertical beam position at IPB (red) vs. added delay for an IP feedback latency scan. The green line represents a sigmoid fit applied to the data. The error bars represent the statistical uncertainty on each data point.

Component	Latency (ns)
Beam time of flight	1
Signal return to processor	20
Signal delay cables	14
FONT V Digital processing*	39
Amplifier*	35
Signal transmission and Kicker fill time*	18
Total	**127**

Table 6.1: The latency of the individual IP feedback components.

Bunch	Ave. Pos. Feedback Off (μm)	Ave. Pos. Feedback On (μm)
1	-0.61 $\pm$ 0.01 $\pm$ 0.01	-0.60 $\pm$ 0.01 $\pm$ 0.01
2	0.81 $\pm$ 0.02 $\pm$ 0.01	-0.08 $\pm$ 0.01 $\pm$ 0.01

Table 6.2: Average positions at IPB for an interleaved feedback run. The first error represents the statistical uncertainty on the results; the second error represents the systematic uncertainty on the results.

A breakdown of the latency of the individual system components is given in Table 6.1, * quantities are taken from [21]. Missing from the table is the latency of the IP BPM analogue signal processing electronics which is unknown. This can be calculated by subtracting the latency of the other components from the total system latency and gives a measure of the electronics latency of 85 ns.

There is considerable scope for optimisation of the latency of the IP feedback system. No effort was made to minimise the lengths of the cables connecting the various components most of which could be reduced. The position of the IP BPM electronics in the tunnel could also be improved moving them closer to the IP BPMs reducing signal round trip times. Finally the signal delay cables described earlier were introduced to meet firmware requirements originating from the upstream system; work on new firmware without such requirements is ongoing and will render the delay cables unnecessary.

6.3.2 IP Feedback Performance

Attempts were made to centre both bunches in IPB and the strength of QD0FF was tuned such that the jitter was larger than the resolution limit of the BPM. IP feedback was set up in interleaved mode, applying a correction on every alternate machine pulse. The bunch position without and with feedback is shown in Figure 6.3 and Table 6.2. The jitters are shown in Table 6.3.

The IP feedback system acts to centre the beam and moves the average beam position of the second bunch closer to zero. The jitter of the second bunch is also reduced, stabilising the beam to nearly 100 nm - a considerable achievement.

Figure 6.4 shows the vertical position of the second bunch vs. the first with feedback off and on. The IP feedback acts to remove the correlation between the bunches rotating the

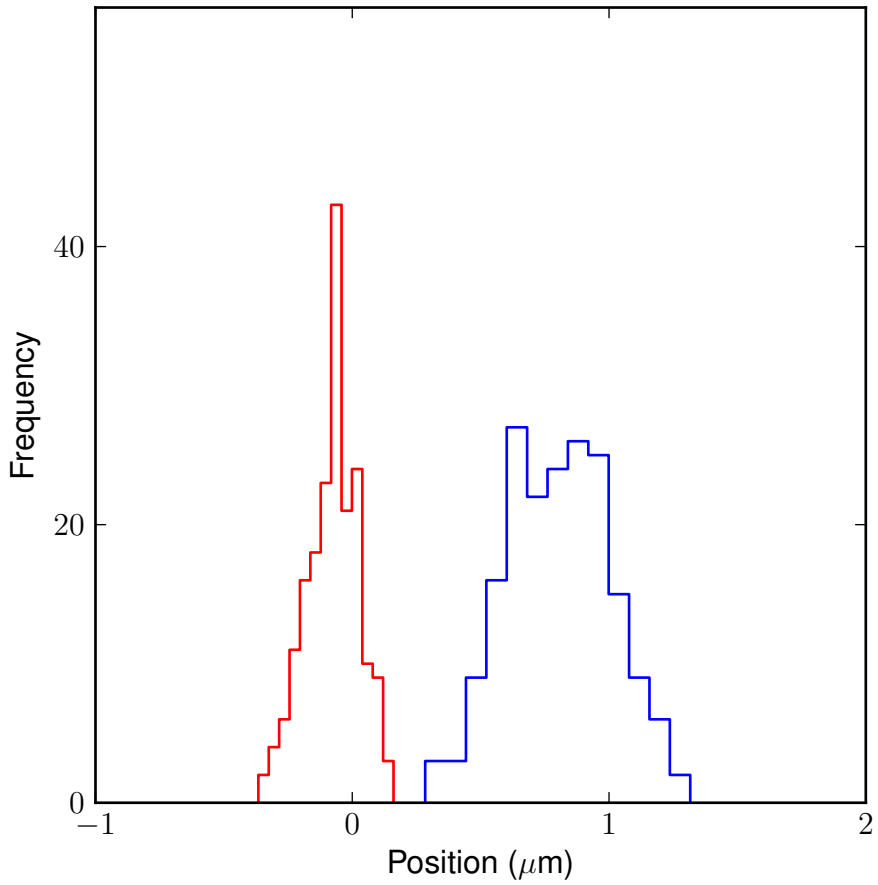

Figure 6.3: Distributions of vertical beam position at IPB without (blue) and with (red) IP Feedback.

Bunch	Feedback Off Jit. (nm)	Feedback On Jit. (nm)
1	197 ± 10 ± 3	198 ± 10 ± 3
2	205 ± 10 ± 3	102 ± 5 ± 1

Table 6.3: Position jitters at IPB for an interleaved feedback run. The first error represents the statistical uncertainty on the results; the second error represents the systematic uncertainty on the results.

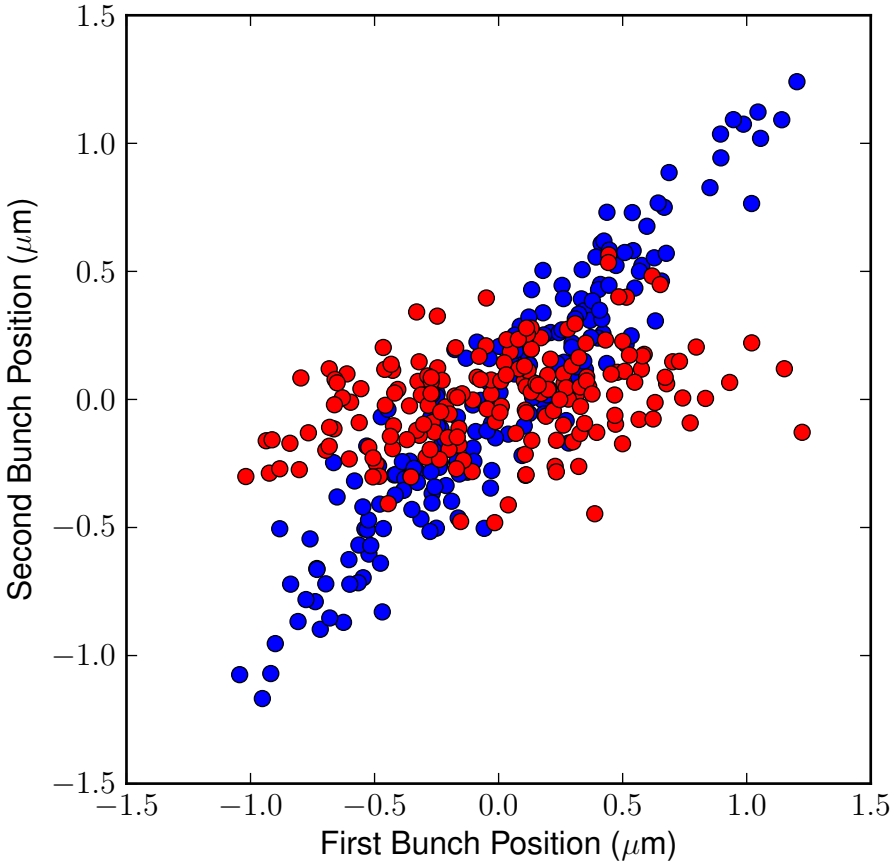

Figure 6.4: Bunch two vs. bunch one position without (blue) and with (red) IP feedback.

Feedback State	Bunch to Bunch Correlation (%)
Off	92 ± 1
On	20 ± 7

Table 6.4: Bunch to bunch position correlations without and with a feedback correction. The errors represent the statistical uncertainty on the results.

distribution and flattening it. The bunch one to bunch two position correlations for both feedback states are given in Table 6.4.

6.3.3 IP Feedback Gain Scan

An IP feedback gain scan was performed to test the accuracy of the model presented in Section 6.2. The IP feedback system was set up; the jitter at IPB was fixed well above resolution limit of the BPM using QD0FF and both bunches were centred. Interleaved IP feedback runs were recorded for a series of gains around the nominal.

The results are presented in Figure 6.5 and Table 6.5 and demonstrate the behaviour expected. The response of the beam jitter to a scaling of the gain is linear around a minimum given by the fit as 0.85. The predicted optimum based on the average bunch to bunch cor-

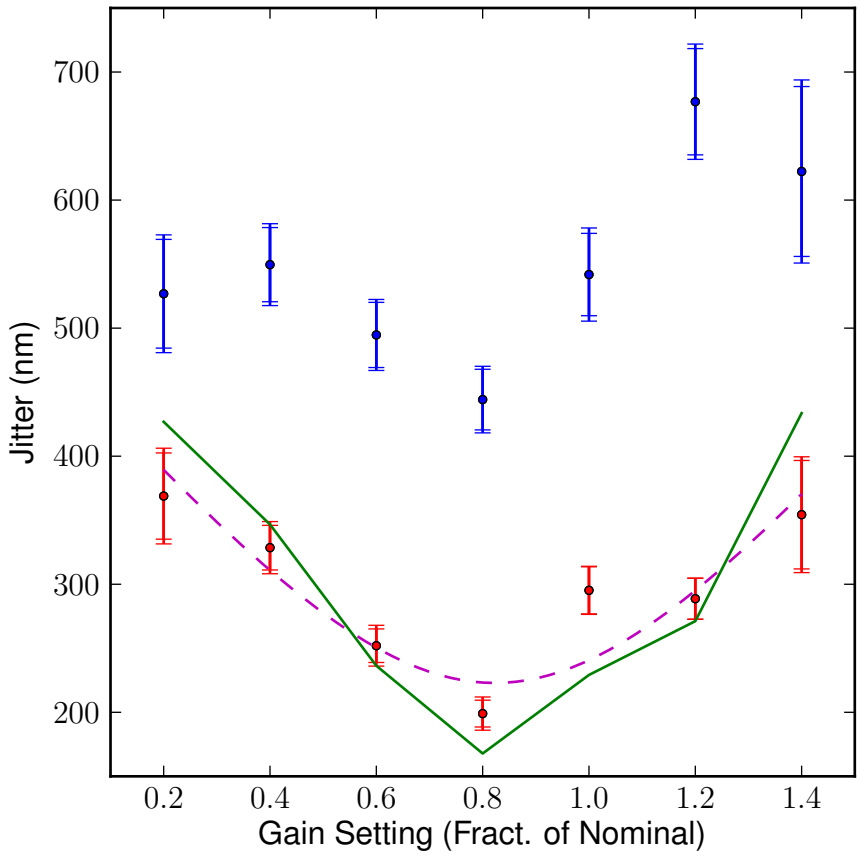

Figure 6.5: Beam position jitter at IPB vs. gain setting for an IP feedback gain scan without (blue) and with (red) an IP feedback correction. The green line represents a prediction on the jitter based on the incoming beam jitter and the gain and the dotted magenta line is a fit applied to the data. The inner error bars represent the statistical uncertainty on each point; the outer error bars represent the total uncertainty on each point.

relation of 90 ± 1% given by Equation 6.17 was 0.9. A prediction for the residual jitter at each point based on the correlations; incoming beam jitter and the gain was given by Equation 6.15 and is also plotted. The level of correction is not as impressive as those shown in Section 6.3.2 as these results were taken before the sample point optimisation technique (Section 3.6.1) was developed.

6.3.4 Dynamic Range of the IP Feedback System

The effectiveness of the IP feedback system at stabilising the average beam position over a range of incoming trajectories was investigated. First the feedback system was set up and the bunches centred; the position of the incoming bunches was then varied by changing the vertical position of the QD0FF final focus magnet. As discussed in Section 3.4 this affects the beam trajectory through the final focus system and changes the beam position after QD0FF. An IP feedback run was taken at a number of QD0FF steps moving the average position of the first bunch at IPB from -6 μm to 3 μm.

Gain Setting (Frac of Nominal)	Feedback Off Jitter (nm)	Feedback On Jitter (nm)
0.2	530 ± 40 ± 4	370 ± 30 ± 4
0.4	550 ± 30 ± 3	330 ± 20 ± 3
0.6	500 ± 30 ± 2	250 ± 10 ± 3
0.8	440 ± 20 ± 2	200 ± 10 ± 3
1	540 ± 30 ± 4	300 ± 20 ± 1
1.2	680 ± 40 ± 4	290 ± 20 ± 1
1.4	620 ± 70 ± 5	350 ± 40 ± 3

Table 6.5: Second bunch vertical beam position jitter measured at IPB over a range of gain settings. The first error represents the statistical uncertainty on the results; the second error represents the systematic uncertainty on the results.

QD0FF Mover Setting (μm)	First Bunch Pos (μm)	Second Bunch Pos (μm)
346	-5.82 ± 0.06 ± 0.03	-2.09 ± 0.03 ± 0.01
347	-4.65 ± 0.04 ± 0.03	-1.94 ± 0.02 ± 0.01
348	-3.89 ± 0.05 ± 0.02	-2.02 ± 0.02 ± 0.01
349	-2.06 ± 0.04 ± 0.01	-1.63 ± 0.02 ± 0.01
350	-0.386 ± 0.04 ± 0.01	-1.32 ± 0.02 ± 0.001
351	0.841 ± 0.04 ± 0.01	-1.12 ± 0.02 ± 0.01
352	2.78 ± 0.04 ± 0.02	-0.759 ± 0.02 ± 0.01

Table 6.6: Mean vertical beam position measured at IPB for a range of QD0FF mover settings. The first error represents the statistical uncertainty on the results; the second error represents the systematic uncertainty on the results.

Histograms of the position distributions of the first and second bunches at each step in the scan are shown in Figure 6.6; the average beam positions are given in Table 6.6 and the beam jitters are given in Table 6.7. The change in the incoming beam position over the steps is clearly visible in the first bunch positions. The IP feedback stabilises the position of the second bunch near zero over the range of the scan. The jitter at each step in the scan is also reduced by the IP feedback system; the level of jitter reduction is not as impressive as that shown in Section 6.3.2 as these results were taken before the sample point optimisation technique (Section 3.6.1) was developed.

QD0FF Mover Setting (μm)	First Bunch Jitter (nm)	Second Bunch Jitter (nm)
346	640 ± 40 ± 6	320 ± 20 ± 3
347	560 ± 30 ± 5	290 ± 20 ± 3
348	670 ± 40 ± 6	300 ± 20 ± 3
349	550 ± 30 ± 4	250 ± 10 ± 2
350	510 ± 30 ± 4	280 ± 10 ± 1
351	450 ± 20 ± 4	300 ± 20 ± 1
352	530 ± 30 ± 3	290 ± 20 ± 1

Table 6.7: Vertical beam position jitter measured at IPB for a range of QD0FF mover settings. The first error represents the statistical uncertainty on the results; the second error represents the systematic uncertainty on the results.

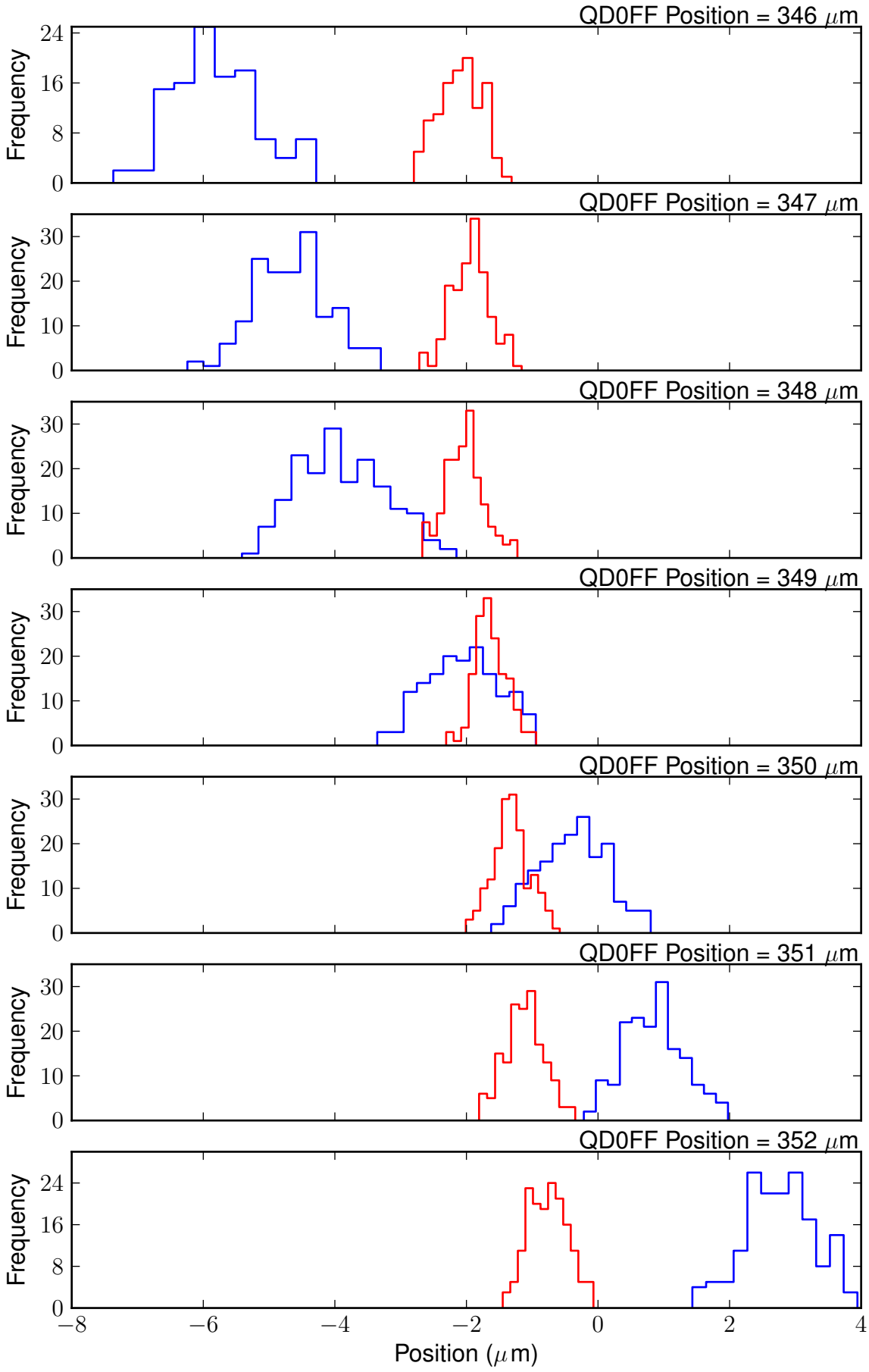

Figure 6.6: Distributions of vertical beam position at IPB vs. QD0FF mover position setting for bunches one (blue) and two (red) with an IP feedback correction.

QD0FF Setting (A)	Feedback Off Jitter (nm)	Feedback On Jitter (nm)
134.8	750 ± 40 ± 3	176 ± 9 ± 2
135.2	480 ± 20 ± 4	189 ± 10 ± 3
135.6	160 ± 8 ± 1	186 ± 10 ± 1
136	200 ± 10 ± 2	164 ± 9 ± 2
136.4	520 ± 30 ± 7	187 ± 10 ± 4
136.8	800 ± 40 ± 7	247 ± 10 ± 2

Table 6.8: Second bunch vertical beam position jitter measured at IPB over a range QD0FF current settings. The first error represents the statistical uncertainty on the results; the second error represents the systematic uncertainty on the results.

6.3.5 Waist Scan

A final experiment was undertaken to test the IP feedback system performance over a range of incoming beam jitters. As with feedforward the experimental method was to scan the QD0FF current setting to move the waist through IPB. IP feedback runs were taken at each QD0FF setting in interleaved mode; the jitters for feedback on and feedback off are shown in Figure 6.7 and Table 6.8. For IP feedback the gain constants are not functions of QD0FF strength and so the IP feedback system should reduce the beam jitter to a constant level regardless of incoming beam jitter. It is clear from Figure 6.7 that the system is performing as expected.

As discussed in Section 6.2 the resolution of IPB gives an upper limit on the feedback performance. The minimum jitter of a detailed IP waist scan taken earlier in the day was used to estimate an upper limit on IPB's resolution, which provides an upper limit on the feedback performance of 135 nm; this is higher than other results quoted as this data was taken before the development of sample point optimisation (Section 3.6.1). A prediction of the residual beam jitter after feedback based on incoming beam conditions, is given by Equation 6.12 and is also plotted. The results show good agreement with the predictions and demonstrate the feedback system is operating close to the performance limit given by $\sqrt{2}\sigma_{IPB}$.

6.4 Summary

A system has been presented that uses the local cavity BPM, IPB, to stabilise the position of the beam waist at the ATF2 final focus. The system comprises components sourced from the upstream feedback system and the analogue cavity BPM processing electronics. A method for the calculation of the gain constants used in the system has been given and a model has been devised to calculate the expected residual beam jitter after IP feedback.

Demonstrations of the system have shown it behaving as expected and results with jitter reduction to 100 nm levels have been shown. Scans showing it stabilising the average incoming beam position over a range of 9 μm have been detailed and the level of jitter reduction is

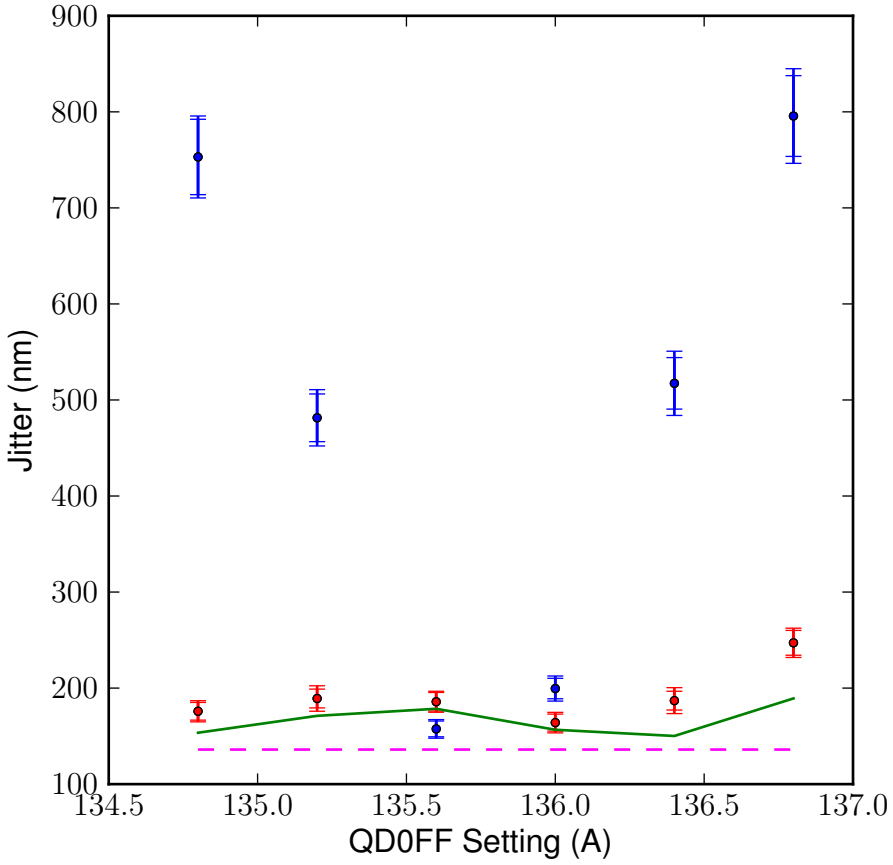

Figure 6.7: Vertical beam jitter at IPB vs. QD0FF current without (blue) and with (red) an IP feedback correction for a QD0FF scan. The green line represents a prediction of the residual jitter after the correction based on Equation 6.12, the dotted magenta line represents the minimum beam jitter calculated using Equation 6.11 and the resolution of IPB. The inner error bars represent the statistical uncertainty on each point; the outer error bars represent the total uncertainty on each point.

constant over beam jitters ranging from approximately 100 to 600 nm. The measured performance of the system is in line with predictions from the model and suggests it is performing close to the limit given by the resolution of IPB.

Chapter 7

Conclusions

7.1 Summary

Measurements at the LHC have demonstrated the existence of a Higgs particle; such a discovery establishes the case for a lepton collider capable of performing detailed studies of its properties. The established designs for such a machine require beam-sizes of order 5 nm in the vertical plane at the IP to achieve a high luminosity. Beam jitter caused by the displacement of the final focus magnets by ground motion is enough to offset such a small beam and reduce the collider's luminosity. As such any current design for a linear collider would require some position feedback system to stabilise the beams at the IP; the FONT project is the prototype for such a system.

The performance of any position feedback system is constrained by the accuracy of the position measurements used as inputs to the feedback. The FONT system uses two types of BPM: stripline BPMs in the upstream region and cavity BPMs in the IP region. The first two chapters of this thesis therefore describe work undertaken regarding the BPMs.

The sensitivity of the upstream stripline processing electronics to LO signal phase jitter was studied. Tests showed that this sensitivity was the main limiting factor in the BPM resolution. An offline analysis to remove this sensitivity was set out. A second method using RCPS to remove the BPM phase sensitivity online and improve the accuracy of position measurement used in the feedback loop, was also described. The results from these tests demonstrated resolutions of approximately 0.35 μm; the theoretical limit on the BPM resolution from the ADC noise was calculated to be 0.25 μm.

The processing scheme used for the cavity BPMs was set out and work detailing the response of the electronics was presented. Studies of the cavity BPMs demonstrated position resolutions of approximately 100 nm. Further offline processing methods were presented yielding a best resolution estimate of approximately 85 nm.

The final three chapters of this thesis detail the development three different experimental prototypes of feedback systems for use at a linear collider. These prototypes were based at the ATF2 at KEK and all three demonstrated successful stabilisation of the ATF2 beam waist. As such they mark the first attempts at progress towards the second ATF2 goal of stabilising the ATF2 beam waist at approximately 2 nm.

The first system uses two stripline BPMs and two stripline kickers in the upstream ATF2 region to measure the position and angle of the first bunch and correct the position and angle of the second. The propagation of this correction downstream to the IP region was then studied by measuring the beam jitter at the IP. Although these tests demonstrated successful vertical beam stabilisation of the ATF2 waist they were hampered by the setup of the accelerator in the FONT region.

A second system used the position of the first bunch measured in two of the upstream stripline BPMs to predict the position of the second bunch at the IP; the local IP kicker then implemented a correction based on this prediction at the ATF2 beam waist. The system demonstrated vertical stabilisation of the ATF2 beam waist at the 100 nm level with a dynamic range of at least 6 μm; the latency of the feedforward system was measured to be 202 ns. Two frameworks for describing the source of the residual beam jitter after the feedforward correction are set out; both agree well with the data. The second framework suggests that at low jitters the largest contribution to the residual beam jitter is the resolution of IPB.

The third system takes as input the position of the first bunch measured at IPB and outputs a correction to the second bunch based on this using the local IP kicker. Vertical stabilisation of the ATF2 beam waist at the 100 nm level was demonstrated over a dynamic range of at least 9 μm; the system proved effective at maintaining the level of jitter over an input range of 100 to 600 nm; the system latency was measured to be 202 ns.

Previous tests of the upstream feedback system have demonstrated the requirements for an ILC beam stabilisation system which requires single loop stabilisation at the 1 μm level for an ILC like beam energy scaled to 1 GeV [21]. The tests suggest that a different type of system not necessarily based inside the detector could also provide

7.2 Outlook

The IP BPMs used during the experiments described herein have now been removed from the IP region at the ATF and replaced with a completely new BPM system. The new system consists of three cavity BPMs with frequencies in the C-band range. These new BPMs have been designed with very short decay times which should ensure the signals from different bunches do not overlap one another. The new BPMs are mounted on a mover system which enables the position of each BPM to be set independently. In addition a new set of processing electronics has been designed and built; the new electronics downmixes the signals from the cavity BPMs from C-band to baseband in a single stage before splitting the signal to produce

I and Q.

This new system has several advantages over the system used for these experiments: 1) Calibrations of the BPMs are easier as the mover can be used to move the BPM directly whilst the position of the beam is held constant. 2) As there is a BPM triplet the BPM resolution can be accurately calculated using the method set out in Chapter 2. 3) The new electronics have a higher gain, and are designed with a resolution target of around 2 nm.

The system has been installed at the ATF and the initial work commissioning has begun. The FONT group is involved in this programme but until the commissioning is complete further studies at the IP involving feedback is impossible.

The challenges involved with the new BPM system are considerable. The gain of the elections is so high that it is easy to saturate the electronics if the beam is not very well centred. This means that even setting up the final focus system correctly to take measurements is exceptionally difficult and will require very precise tuning. Additionally the signal to noise ratio required to resolve such small distances means the characteristics of the electronics will have to be exactly known. Any slight imperfections in the setup or the cabling of the system could cause reflections and interference which would decrease the resolution beyond the required point.

A new stripline has been installed mid-way along the final focus line and is instrumented using the high resolution stripline electronics presented in Chapter 2. This is being used in experiments aimed at studying the effects of the phase advance in the upstream system on the upstream feedback and the propagation of the upstream correction downstream.

Finally the FONT group is involved in a new study with colleagues from CERN. Existing stripline BPMs throughout the extraction and final focus lines are being instrumented with the high resolution stripline electronics and used to study the beam jitter along the beam-line. Is is hoped that this will pinpoint sources of jitter throughout the beam-line.

Bibliography

[1] CERN Press Office. "LHC physics data taking gets underway at new record collision energy of 8TeV". Press Release (2012). press.web.cern.ch/press-releases/2012/02/lhc-run-4-tev-beam-2012

[2] A. Hofmann. "The Physics of Synchrotron Radiation". Cambridge University Press (2004).

[3] W. Herr et al. "Concept of Luminosity". CERN Accelerator School: Intermediate Accelerator Physics Course, (2006).

[4] O. Bruning. "Turnaround Time in Modern Hadron Colliders and Store-length Optimization". Proceedings of BEAM07, CERN, Geneva, Switzerland, (2007), 2.

[5] M. Herrer. "The Standard Model" (1998). ArXiv:hep-ph/9812242v1.

[6] P. Higgs. *Phys. Rev. Lett.*, **13** (1964) 508.

[7] C. Campagnari et al. *Rev. Mod. Phys.*, **69** (1997) 137.

[8] K. Kodama et al. *Physics Letters B*, **504** (2001) 218.

[9] S. Chatrchyan et al. *Physics Letters B*, **716** (2012) 30.

[10] G. Aad et al. *Physics Letters B*, **716** (2012) 1.

[11] Vogel. "Beam-induced backgrounds in detectors at the ILC". Ph.D. Thesis, Hamburg University (2008).

[12] D. Griffiths. "Introduction to Elementary Particles". Wiley (2008).

[13] R. Lipton et al. "Muon Collider: Plans, Progress and Challenges" (2012). FERMILAB-CONF-12-883-PPD.

[14] M. G. Minty et al. "Measurement and Control of Charged Particle Beams". Springer (2003).

[15] T. Behnke et al. "A Multi-TeV linear collider based on CLIC technology: CLIC Conceptual Design Report" (2013). CERN-2012-007.

[16] C. Adolphsen et al. "International Linear Collider Technical Design Report Volume 3: Accelerator" (2013). ArXiv:1306.6328.

[17] W. Kilian et al. *Phys. Lett. B*, **373** (1996) 135.

[18] M. Aicheler et al. "CLIC Conceptual Design Report Volume 1: A multi TeV Linear Collider based on CLIC Technology" (2012). ArXiv:1209.2543.

[19] "CTF website". `http://ctf3.web.cern.ch/ctf3/`

[20] P. Raimondi et al. *Phys. Rev. Lett.*, **86** (2001) 3779.

[21] B. Constance. "Design and beam testing of a fast, digital intra-train feedback system and its potential for application at the International Linear Collider". DPhil Thesis, University of Oxford (2011).

[22] J. Resta-Lopez et al. *JINST*, **5** (2010) P09007.

[23] P. N. Burrows. "Feedback on Nanosecond Timescales FONT: Results from First Beam Tests at the NLCTA at SLAC". Proceedings of PAC2003, Portland, USA, (2003), 687.

[24] P. N. Burrows et al. "Nanosecond-timescale Intra-bunch-train Feedback for the Linear Collider: Results of the FONT2 Run". Proceedings of EPAC2004, Lucerne, Switzerland, (2004), 785.

[25] "FEATHER website". `http://acfahep.kek.jp/subg/ir/feather/index.html`

[26] P. N. Burrows et al. "Tests of the FONT3 Linear Collider Intra-Train Beam Feedback System at the ATF". Proceedings of PAC2005, Knoxville, Tennessee, USA, (2005), 1359.

[27] P. N. Burrows et al. "Performance of the FONT3 Fast Analogue Intra-train Beam-based feedback system at ATF". Proceedings of EPAC2006, Edinburgh, Scotland, (2006), 852.

[28] P. N. Burrows et al. "Design of the ILC Prototype FONT 4 Digital Intra-train Beam-based Feedback System". Proceedings of EPAC2006, Edinburgh, Scotland, (2006), 849.

[29] P. N. Burrows et al. "The FONT4 ILC Intra-train Beam-based Digital Feedback System Prototype". Proceedings of PAC2007, Albuquerque, New Mexico, USA, (2007), 416.

[30] R. J. Apsimon et al. "Design and Performance of a Prototype Digital Feedback System for the International Linear Collider Interaction Point". Proceedings of EPAC08, Genoa, Italy, (2008), 3245.

[31] R. J. Apsimon et al. "Beam Test Results with the FONT4 ILC Prototype Intra-Train Beam Feedback System". Proceedings of PAC09, Vancouver, BC, Canada, (2009), 2676.

[32] R. J. Apsimon et al. *Physics Procedia*, **37** (2012) 2063.

[33] Inc. Xilinx. "Virtex-5 FPGA User Guide" (2009). `www.xilinx.com/support/documentation/userguides/ug190.pdf`

[34] Inc. Xilinx. "Platform Flash PROM User Guide" (2009). `www.xilinx.com/support/documentation/userguides/ug161.pdf`

[35] Texas Instruments. "Datasheet for ADS5474 14-bit, 400 MSPS Analog-to-Digital Converter" (2007). `www.ti.com/lit/ds/symlink/ads5474.pdf`

[36] Analog Devices. "Datasheet for AD9744 14-bit, 210 MSPS TxDAC D/A Converter" (2005). www.analog.com/static/imported-files/datasheets/AD9744.pdf

[37] "ATF website". http://atf.kek.jp/

[38] H. Sakai et al. *Phys. Rev. ST Accel. Beams*, **5** (2002) 122801.

[39] S. Araki. "ATF2 beamline layout". Private Communication.

[40] ATF2 Group. "ATF2 proposal. Vol. 1" (2006). ArXiv:physics/0606194.

[41] G. R. White et al. *Phys. Rev. Lett.*, **112** (2014) 34802.

[42] R. Fulton et al. *NIM A*, **274** (1989) 37.

[43] P. Tenenbaum et al. *Annual Review of Nuclear and Particle Science*, **49** (1999) 125.

[44] J.Yan et al. *NIM A*, **740** (2013) 131.

[45] A. Sørensen. "Liouville's theorem and emittance". CERN Accelerator School : 3rd General Accelerator Physics Course, (1988), 18. CERN-2006-002.361.

[46] M. Wendt. "BPM Instrumentation: A Short Introduction for Non-Experts" (2000). Introductory talk given at DESY lab.

[47] R. E. Shafer. "Beam Position Monitoring". AIP Conference Proceedings, volume 249 (1992), 601.

[48] N. Terunuma. Private Communication.

[49] R. J. Apsimon. "The Development and Implementation of a Beam Position Monitoring System for use in the FONT Feedback System at ATF2". DPhil Thesis, University of Oxford (2012).

[50] D. R. Bett. "The Development of a Fast Intra-train Beam-based Feedback System Capable of Operating on the Bunch Trains of the International Linear Collider". DPhil Thesis, University of Oxford (2013).

[51] Mini Circuits. "LFCN-1000 Data Sheet". http://217.34.103.131/pdfs/LFCN-1000.pdf

[52] Mini Circuits. "SCPJ-2-9 Data Sheet". http://www.minicircuits.com/products/psc_sm_2_180.html

[53] C. Perry. Private Communication.

[54] Mini Circuits. "SYM-2 Data Sheet". http://217.34.103.131/pdfs/SYM-2.pdf

[55] S. Sakanaka et al. "Construction of a 714-MHz RF system for the ATF damping ring". Proceedings of the 1997 Particle Accelerator Conference, (1997), 2980.

[56] Linear Technologies. "LT Spice Users Guide".

[57] S. Molloy et al. "A Flight Simulator Based Beam Based Alignment Package for ATF2". Proceedings of PAC09, Vancouver, BC, Canada, (2009).

[58] Y. I. Kim. "Cavity Beam Position Monitor System for the Beam Delivery and Interaction Point of the Accelerator Test Facility 2 and Future Linear Collider". Ph.D. Thesis, Kyungpook National University (2012).

[59] S. Walston et al. *NIM A*, **578** (2007) 1.

[60] Y. Inoue et al. *Phys. Rev. ST Accel. Beams*, **11** (2008) 62801.

[61] Y. I. Kim et al. *Phys. Rev. ST Accel. Beams*, **15** (2012) 42801.

[62] S. Boogert. Private Communication.

[63] Agilent. "8494/95/96G/H Attenuators Data Sheet". `http://cp.literature.agilent.com/litweb/pdf/08495-90025.pdf`

[64] "The LUCRETIA Project Homepage". `http://www.slac.stanford.edu/accel/ilc/codes/Lucretia/`

[65] Y. Renier. "Implementation and validation of the linear collider final focus prototype: ATF2 at KEK (Japan)". Ph.D. Thesis, De l'Universite Paris XI Orsay (2010).

[66] "ATF Logbook for the June 2013 Period". `http://atf.kek.jp/twiki/bin/view/ATFlogbook/ATFlogbookCalendar`

[67] Y. I. Kim et al. "Cavity Beam Position Monitor at the Interaction Point Region of the Accelerator Test Facity 2". Proceedings of IPAC2013, Shanghai, China, (2013).

[68] G. B. Christian et al. "Latest Performance Results from the FONT5 Intra-Train Position and Angle Feedback System at ATF2". Proceedings of IPAC2011, San Sebastián, Spain, (2011).

[69] D. R. Bett et al. "Latest Performance Results from the FONT5 Intra-train Beam Position and Angle Feedback System at ATF2". Proceedings of IPAC2012, New Orleans, Louisiana, USA, (2012).

[70] Mini Circuits. "ZPUL-21 Data Sheet". `http://217.34.103.131/pdfs/ZPUL-21.pdf`

[71] "TMD Technologies Limited website". `www.tmd.co.uk`

[72] G. R. White. Private Communication.